Mixing Processes Near Boundaries

by

Keir Murray Colbo
B.Sc., Memorial University of Newfoundland, 1994

A Dissertation Submitted in Partial Fulfillment of the
Requirements for the Degree of

DOCTOR OF PHILOSOPHY

in the School of Earth and Ocean Sciences

We accept this dissertation as conforming
to the required standard

[signed]

Dr. C. Garrett, Supervisor (School of Earth and Ocean Sciences)

[signed]

Dr. R. Lueck, Departmental Member (School of Earth and Ocean Sciences)

[signed]

Dr. R. Dewey, Departmental Member (School of Earth and Ocean Sciences)

[signed]

Dr. S. Dosso, Departmental Member (School of Earth and Ocean Sciences)

[signed]

Dr. R. Thomson, Departmental Member (Institute of Ocean Sciences)

[signed]

Dr. H. Seim, External Examiner (University of North Carolina)

©Keir Murray Colbo, 2002
University of Victoria
All rights reserved. This dissertation may not be reproduced in whole or in part,
by photocopying or other means, without the permission of the author.

Abstract

Using a large eddy simulation (LES) model the cross-cell diffusion of neutrally buoyant and buoyant particles in Langmuir circulation is studied. The non-dimensional diffusivity is found to asymptote to a constant value for sufficiently small Langmuir number. This allows a parameterization for the cross-cell diffusivity that depends only on well known physical properties of the wind and wave field. Buoyant particles are found to behave similarly, but with a substantial reduction of the cross-cell diffusivity.

Lateral Reynolds stresses from an array of acoustic Doppler current profilers (ADCPs) are computed for fluctuations about a tidal mean. The results are compared with the observed lateral shear to estimate the horizontal eddy viscosity, $O(10\,m^2/s)$. Possible parameterizations of the eddy viscosity are discussed. The lateral Reynolds stresses acting on the estuarine mean flow are also calculated.

The velocity data from the ADCPs along with density data from temperature chain moorings are used to examine the partition of energy between internal waves and the vortical mode. Consistency relations for the ratio of counterclockwise to clockwise energy (CCW/CW) and potential to horizontal kinetic energy (PE/HKE) are modified to account for the effect of boundaries and Doppler shifting. Exact partitioning of the energy is not possible, but the signature of both internal waves and vortical modes can be detected.

Examiners:

[signed]

Dr. C. Garrett, Supervisor (School of Earth and Ocean Sciences)

[signed]

Dr. R. Lueck, Departmental Member (School of Earth and Ocean Sciences)

[signed]

Dr. R. Dewey, Departmental Member (School of Earth and Ocean Sciences)

[signed]

Dr. S. Dosso, Departmental Member (School of Earth and Ocean Sciences)

[signed]

Dr. R. Thomson, Departmental Member (Institute of Ocean Sciences)

[signed]

Dr. H. Seim, External Examiner (University of North Carolina)

Contents

List of Tables

List of Figures

Acknowledgements

I'd like to thank my supervisor, Chris Garrett, for his support, mentorship and patience. Richard Dewey organized and supervised the field work. The other members of my committee (Rolf Lueck, Rick Thomson, and Stan Dosso) have provided useful feedback and direction. Ming Li provided useful help in the adaption of the computer code used in the Langmuir circulation simulations. My parents, Murray and Deirdre, have encouraged my career, and early on instilled in me a love of learning. My wife, Caroline Martin, has provided endless encouragement, understanding and love. Her faith in me has been a constant well of strength. I'd finally like to mention my daughter, Chloe, who has given me the final bit of incentive necessary to shake off this albatross.

1 Introduction

The dynamics of the ocean depends upon the fluxes of buoyancy and momentum that are transmitted through the sea surface and the ocean bottom. Knowledge of the fluxes themselves is not sufficient to determine the behaviour of the ocean interior. This will depend critically on the physical processes that transport the momentum and buoyancy away from the boundaries. To see this consider only a portion of the ocean, or a lake, where you might swim in the summer. After several weeks of sun in the summer, the water in a secluded cove might finally become comfortable, while the water in a nearby tidal channel will remain bone chilling. The difference is in the level of mixing that transports the heat of the sun's rays away from the surface. Aside from the effect on the dynamics caused by the redistribution of mass and momentum, these processes also play a significant roll in the transport of tracers. This could include sewage discharge at an outfall, oil spills on the surface, or the diffusion of gases such as CO_2.

Irreversible mixing, as opposed to stirring, happens on the smallest of scales (millimeters) by molecular diffusion. The inputs of energy are predominantly large scale: tides have wavelengths of 1000s of kilometers, solar radiation is fairly uniform over 10s to 100s of kilometers, even rivers have some finite-size mouth. Molecular diffusion alone could work to erode gradients on these large scales, but not very efficiently. In order to be effective molecular diffusion needs strong gradients and large surface areas over which to act. It is the intermediate scale processes that act to provide those strong gradients. The large scale flows generate smaller scale perturbations, that themselves generate smaller scale perturbations, etc., until the processes have reached sufficient size that molecular diffusion can act effectively. The energy is thus seen to cascade from its input at large scales to

its dissipation at small scales. Because this energy cascades in a chain (perhaps a branching chain), it may be advantageous to examine any single process in the chain in order to draw conclusions about the whole. However, it is not always clear which process determines the rate of energy transfer, nor would all processes act in the same manner: one process might be stable for long time periods whereas one might break up rapidly, one process might be stationary whereas one may travel substantial distances. It is therefore the goal of this thesis to understand some of these intermediate scale processes.

Juan de Fuca Strait and the surrounding Gulf Islands (figure 1) is an excellent region in which to study the effects of mixing. It has both strong sources of stratification, due to river runoff, and strong sources of mixing, primarily due to tidal dissipation. This gives us the ability to consistently observe mixing events, as opposed to having to randomly search for them, such as might be the case in the open ocean. The tidal currents may, depending on location, completely mix the water column destroying all stratification, but the constant input of new water means that as soon as the tidal currents weaken the stratification will return. There is also a great range of mixing strengths visible in the surrounding waters. The mixing within Juan de Fuca Strait may be relatively weak, though still strong compared to the deep ocean, whereas the mixing in the small channels between the Gulf Islands may be sufficient to erase all stratification.

In this thesis, I investigate three main topics. All are concerned with mixing near ocean boundaries. The first topic concerns the cross-wind diffusivity expected by Langmuir circulation. The second looks at lateral Reynolds stresses next to a side wall. The third deals with the partitioning of energy between internal waves and vortical modes. The Langmuir circulation problem will be addressed

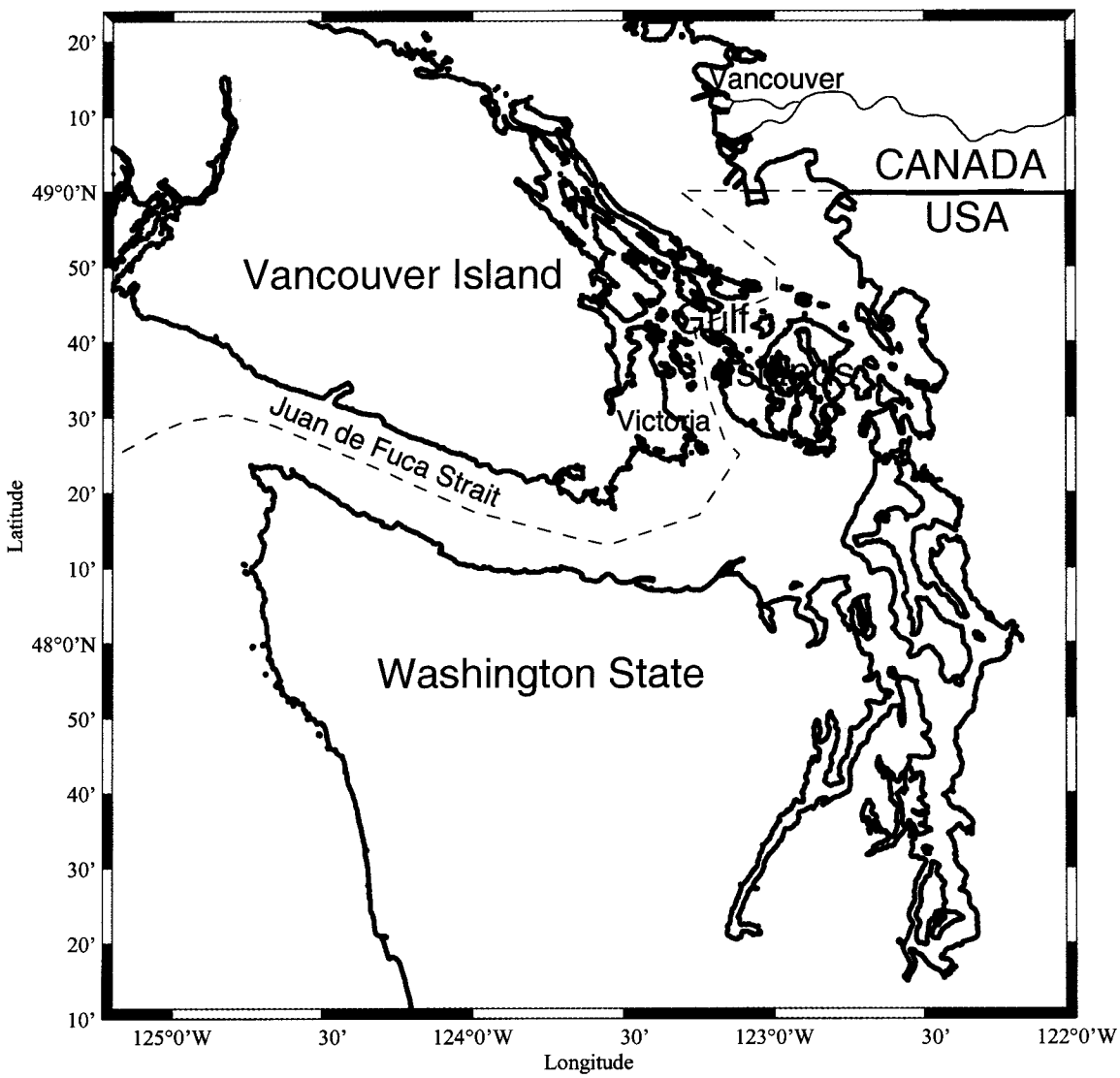

Figure 1: Juan de Fuca Strait and surrounding waters.

through the use of a numerical model. The other two topics are addressed through observational and theoretical means.

The rest of the introduction will provide some background for each of these three problems. Chapter 2 will discuss the modelling of dispersion by Langmuir circulation. It will include a discussion of previous attempts at characterising the dispersion, introduce the basic theory governing Langmuir circulation, lay out the basics of the computer model, and discuss the results for both buoyant and neutrally buoyant particles. Chapter 3 will discuss the theory of the lateral Reynolds stress, internal waves, and vortical modes. A review of boundary layer literature helps us to understand the expected forms of the Reynolds stress. Internal wave consistency relations are presented and modified to account for the boundaries of Juan de Fuca Strait. The vortical mode is first introduced, and then its consistency relations are presented. Finally, I discuss the effect that Doppler shifting due to the tide might have on my observations. Chapter 4 gives a brief outline of the observational program for the different years and details the primary instrumentation. Chapter 5 details the data analysis and the errors involved. The velocity and density data require substantial processing to arrive at a useful data set. The details of the Reynolds stress calculation are provided, and a discussion of the derivation of higher order data products (vorticity and divergence) are given. Chapter 6 presents the Reynolds stress results starting with the lateral Reynolds stress and then looking at the resultant eddy viscosities. Analysis of the spring-neap cycle is also provided. Chapter 7 details the consistency relations with the goal of elucidating the causes of the Reynolds stress. First, we shall look at the effect of the Doppler shift on the data, and then proceed through an analysis of the two main consistency relations (CCW/CW and PE/HKE). Finally we examine the vorticity

and divergence measurements. Chapter 8 provides a discussion of the results, and presents a number of open questions.

1.1 Motivation

1.1.1 Langmuir Circulation

In the open ocean, far from the influence of lateral boundaries, the sea surface is an important boundary for the transfer of momentum, and the primary source of buoyancy forcing. This strong forcing leads to the existence of a number of energetic processes. What motivates this investigation is the dispersion of tracers in this upper ocean mixed layer, with a primary focus on the diffusion of a localized source, such as an oil spill. Langmuir circulation is a dominant dynamic structure in the wind-driven upper ocean [*Langmuir*, 1938; *Leibovich*, 1983; *Weller and Price*, 1988]. It is produced through an interaction of the Stokes drift, due to surface gravity waves, and the surface wind stress. The resulting, fully developed and quasi-steady flow field resembles pairs of counter-rotating vortices oriented roughly in the direction of the wind, and consequently in the direction of the dominant waves (Figure 2).

Surface windrows consisting of foam and flotsam are vivid demonstrations that Langmuir circulations can cause floating particles to congregate at the convergence zones between counter-rotating vortices. It may appear that Langmuir circulation is a mechanism for concentrating floating particles. However, its temporal evolution, including the amalgamation, disintegration and regeneration of Langmuir cells, makes Langmuir circulation effective in dispersing particles, bubbles and oil droplets in the cross-wind direction [e.g. *Thorpe*, 1995a].

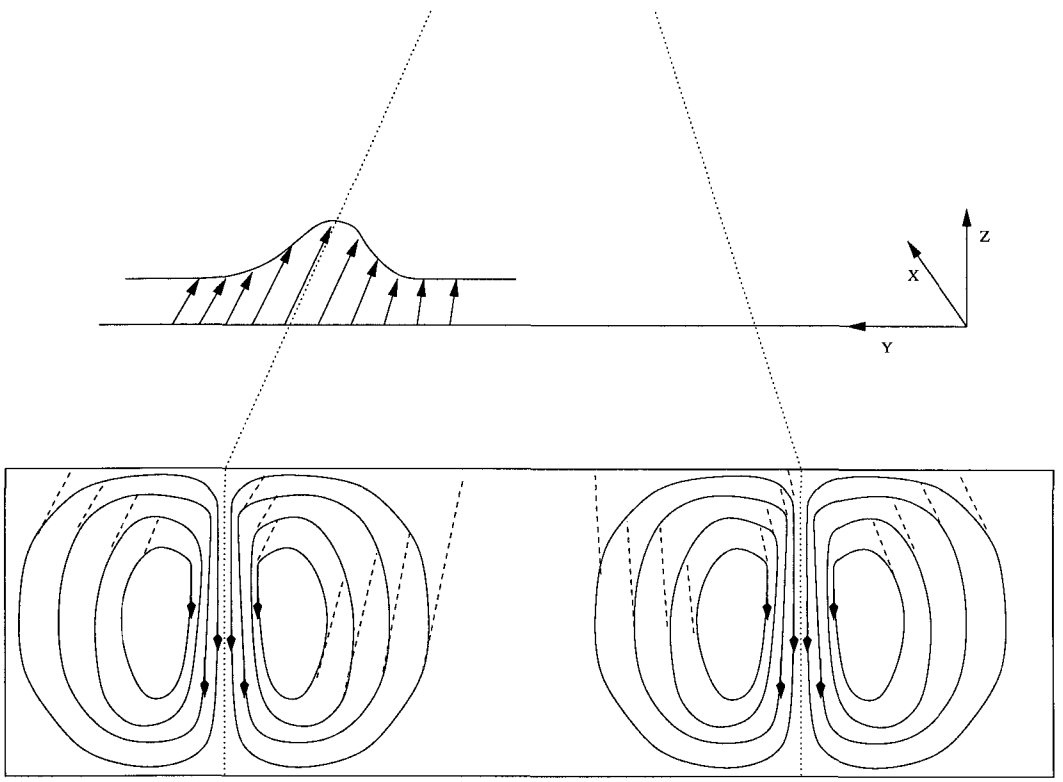

Figure 2: An illustration of Langmuir circulations, showing the subsurface streamlines and the surface water velocity profile.

The surface convergence zone, between two vortices, has an associated narrow downwind jet and is situated above the region of maximum downwelling. The downwelling zone is narrow compared to the cell width and has large vertical velocities, up to $0.1ms^{-1}$, whereas the upwelling zones are broad and have weaker vertical velocities [*D'Asaro and Dairiki*, 1997; *Weller and Price*, 1988]. Langmuir circulations form quickly for winds of order $3ms^{-1}$ or larger, and are found to be only slightly sensitive to surface heating or cooling [*Li and Garrett,* 1995; *Skyllingstad and Denbo*, 1995]. Langmuir circulations are observed to have cell spacing in the region of two meters to two hundred meters, often with smaller scale cells existing alongside the dominant structures [*Leibovich*, 1983]. These smaller cells are constantly created, grow and finally merge with the larger cells. The largest cells typically penetrate to the base of the mixed layer, and may cause the mixed layer to deepen, or at the least delay the onset of restratification [*Li and Garrett,* 1997; *Li et al.*, 1995]. It is common to postulate that the jet spacing is about twice the mixed layer depth on the assumption that the cells are roughly circular.

The strong downwelling velocity ($0.1ms^{-1}$) is comparable to, or larger than, the buoyant rise speed of small bubbles and oil droplets. Bubbles have been observed to penetrate down to more than 10 meters depth [*Zedel and Farmer,* 1991], and oil droplets may be entrained into the water column [*Thorpe*, 1995b]. Therefore, Langmuir circulation can play an important role in the entrainment and diffusion of buoyant tracers.

Previous attempts at modelling the cross-wind diffusivity of Langmuir circulation have been based upon either dimensional arguments [*Csanady*, 1974; *Faller and Auer*, 1988], or observations [*Thorpe et al.*, 1994]. The simplified theory of

Faller and Auer [1988] is difficult to use as a predictive tool since it depends on the windrow lifetime. *Farmer and Li* [1995] state that windrow lifetime is a quantity that is difficult to measure or estimate because individual bubble bands (or windrows) often change their shapes and are difficult to track objectively. Furthermore one might assume that the windrow lifetime is itself dependent on additional variables, particularly the wind speed. Thus to be useful the theory would require observations in the conditions that were to be modelled. Similarly, the measurements of *Thorpe et al.* [1994] are applicable only to the specific conditions that arose during the observations and are difficult to generalize.

Computer modelling gives us the ability to simulate a vast array of different conditions in the upper ocean mixed layer, and to examine how Langmuir circulations regenerate in these different situations. However, there are still tradeoffs that must be accepted. Three-dimensional models of the upper ocean mixed layer contain structure in the downwind direction, but the imposition of a periodic boundary condition along this axis leads one to wonder if the structures are sensitive to the relatively limited size of the computational domain [e.g. *McWilliams et al.*, 1997]. In addition, these models are computationally expensive and are therefore not run for the extended periods of time necessary to study the dispersion of particles. As an example, *McWilliams et al.* [1997] considered the dispersion of particles over a time of 16 minutes. This is less than both an eddy turnover time and the time it would take for the particles to experience strong non-linearities in the down-wind direction.

However, I feel that computer modelling, combined with field observations for verification, is likely to give the most useful parameterization for cross-wind diffusivity.

1.1.2 Reynolds Stress

The horizontal Reynolds stress ($-\rho_0\overline{u'v'}$) is a measure of the flux of momentum in a horizontal direction by the correlated action of current fluctuations. It is common for the Reynolds stress to be approximated in terms of an eddy viscosity acting on the mean flow (e.g. $-\rho_0\overline{u'v'} = \rho_0 A_y \frac{\partial U}{\partial y}$). The use of this parameterization in large-scale computer models of the ocean is common. The resulting flow field solution will be dependent on this chosen value, or parameterization, of the eddy viscosity. However, eddy viscosity is a property of the flow and not the fluid itself, which makes an *a priori* prediction of its value difficult. In order to aid the choice of appropriate values of eddy viscosity it would be useful to have direct measurements of Reynolds stress and the surrounding mean flow. Therefore we need to rely on observations to check both the appropriateness of the approximation and to provide an estimate of a reasonable value.

Although the Reynolds stress is a symmetric tensor, the term is often used to describe the off-diagonal elements of that tensor, namely $-\rho_0\overline{u'v'}$, $-\rho_0\overline{u'w'}$ and $-\rho_0\overline{v'w'}$. By far the greatest amount of oceanographic literature on Reynolds stresses is concerned with the two vertical components, $-\overline{u'w'}$ and $-\overline{v'w'}$, where we drop the density for convenience. The lateral Reynolds stress term, $-\overline{u'v'}$, is a far less studied variable. Near a lateral boundary, one can clearly understand that the transfer of momentum into, or away from, the boundary could have a significant effect on near shore tidal currents. Furthermore, in a coastal environment where stratification reduces the vertical fluxes of momentum, the lateral stress may have a dominant effect. The effect of a lateral boundary on the mean flow and the tides will be one of the primary concerns of this thesis.

Measurements of lateral Reynolds stress reported in the literature are rare.

They fall into two main categories. One is large scale and based upon satellite altimetry [e.g. *Provost and Le Traon*, 1993] or tomography [e.g. *Chester et al.*, 1994], the other is small scale and focuses on stress transfer in bottom boundary layers, particularly on beaches [e.g. *Stanton and Thornton*, 1997]. The medium scale measurements made by our ADCP array are therefore important, at the very least due to their novelty. The array of instruments allows us to go further than just measuring the Reynolds stress, it also lets us examine the relation between the stress and the large-scale shear.

The eddy viscosity parameterization follows from an analogy with the molecular level, where the viscosity is a constant property of the medium. However, the eddy viscosity will vary regionally, being different in the open ocean as compared to a constrained channel within the Gulf Islands. The eddy viscosity is also dependent on the time and space scales resolved, since it attempts to account for the remaining fluctuations. This could cause problems in a computer simulation that attempts to model the complex flow in a region like the British Columbia coast, without resolving the processes responsible for transferring momentum out of the tides and currents.

1.1.3 Lateral Boundary Processes

Lateral boundaries can support a wide range of physical processes, from large-scale Kelvin waves to small-scale turbulent boundary layers. We are concerned with intermediate scale processes, with wavelengths from about one hundred meters to several kilometers. These processes will generally fall below the resolution of many oceanographic models, and thus need to be parameterized. These are also the processes which are largely responsible for the Reynolds stresses I will

calculate. This region of phase space has two dominant physical processes: The internal wave and the vortical mode.

These motions have similar spatial scale, but differ in many aspects: lifetime, intrinsic velocity, vertical structure, governing dynamics. Internal waves are freely propagating motions that can travel great distances from their point of generation. Vortical modes are slow moving features, that are likely to only have a local effect on the ocean. Thus, it seems unlikely that a single parameterization could describe both processes. Tides and mean currents transfer some of their energy to these two types of flow. A regime where most of the energy goes into the vortical mode (e.g. eddies) would have a major impact on the local flow field, whereas an internal wave dominated regime might exert minimal change locally, but causes subtle changes over a large area away from the boundary.

Internal waves are ubiquitous features of the worlds oceans, and as such have been highly studied. A key component of internal wave behaviour is their ability to propagate long distances with little dissipation. This means that regions of the ocean that are far from the boundaries where internal waves are generated can have a reasonably energetic spectrum of internal wave motions. These waves may play an important role in the quiescent interior, by providing a low level of internal wave breaking to maintain stratification. Even if waves generated along the coast were dissipating locally, the region of mixing and its time scales, will depend on the characteristics of the internal wave field.

The vortical mode is a less studied feature than internal waves, and so we should start with this definition by *Kunze* [2001]

> Vortical modes have come to denote both linear and nonlinear sub-inertial (intrinsic frequency $\omega \ll f$) ocean fine-structure with vertical

> wavelengths < 100 m which cannot be described as internal gravity waves.

Here Kunze is trying to describe the collection of small scale features that are in either geostrophic or cyclostrophic balance (and in the context of this thesis will largely refer to meso-scale eddies). In contrast to internal waves, vortical modes are slow moving or stationary features. Therefore they can only exert an influence on the local environment. This is not to say that a steady geostrophic current cannot have a large velocity, but the feature itself is stationary or meanders at a slow rate. In Juan de Fuca Strait, we postulate that most of the vortical mode will be composed of eddies generated by the strong tidal flow along the irregular sides.

The partition of tidal energy into these two forms is an important problem, since the two processes behave quite differently from one another, and will have substantially different parameterizations. In order to differentiate internal waves from vortical modes within the data it is necessary to know their defining characteristics. Although vortical modes are inherently sub-inertial, they can appear at internal wave frequencies in the data due to the Doppler shift effect of the tidal flow. Therefore we must consider the consistency relationships inherent in the dynamics of each type of motion. There are many consistency relations that exist for a given physical process [e.g. *Lien and Müller*, 1992a]. Two of the more commonly studied relations are the ratio of potential to horizontal kinetic energy, and the ratio of counterclockwise to clockwise kinetic energy. Consistency relations are typically derived under assumptions of an infinite ocean and random phase. However, the constrained boundaries of the strait alter these common consistency relationships by imposing a modal structure.

Previous papers have identified the co-existence of internal waves and vortical

modes in oceanic data, and have attempted to partition the energy [Kunze and Sanford 1993, Kunze 1993, D'Asaro and Morehead 1991]. These previous efforts have used arrays of vertical profilers to map out a snapshot of the upper ocean. No one has succeeded in calculating this partition from moored time series.

Unlike the previous regions where this partition was attempted, Juan de Fuca Strait has strong background currents, $O(1\,ms^{-1})$. The resulting Doppler shift can be substantial for medium scale features with wavelengths of hundreds of meters to several kilometers. I thus need to not only explore how consistency relations will be altered by boundaries, but also how our mooring will perceive these relations as the flow field advects them back and forth.

1.2 Goals

This thesis has several goals.

1. To find a parameterization for the cross-wind diffusivity associated with Langmuir circulations, that is applicable over a wide range of sea states. This will include formulae for both neutrally buoyant particles, as well as buoyant particles. The buoyant particle solutions will be for inert tracers, and are thus aimed at reproducing oil droplet dispersion rather than the dispersion of air bubbles caused by breaking wave events.

2. To measure the horizontal Reynolds stress, $\overline{u'v'}$. Having done this at several moorings in an array, we would like to examine how the Reynolds stress compares to the shear in the background flow. This will allow us to gauge the appropriateness of the eddy viscosity parameterization, $\overline{u'v'} = -A_y \frac{\partial U}{\partial y}$. We will also be able to estimate what an appropriate value might be for the

eddy viscosity, and can discuss how this matches what is used in computer models of similar regions. Furthermore, I can examine how the Reynolds stress differs depending upon what I define as the mean flow and what I define as the fluctuations.

3. To partition the observed energy in Juan de Fuca Strait into internal wave and vortical mode components. However, we realize from the outset that this is a difficult, perhaps impossible, task given both our data set and the difficulty imposed by the strong Doppler shift. I would like to be able to unambiguously detect the presence of both processes, and compare observed data with predicted consistency relations. In attempting to do this we will point out many potential pitfalls that exist in the blind use of consistency relations. In the course of our analysis, we will learn much about the nature of each of the two processes.

2 Langmuir circulation

2.1 Craik-Leibovich Theory

Although Langmuir circulation was first described by *Langmuir* [1938], it took many years before the currently accepted theory was proposed, first by *Craik* [1977] and then refined by *Leibovich* [1977b]. This theory, often named CL2, was adapted from earlier work [*Craik*, 1970; *Leibovich and Ulrich*, 1972; *Craik and Leibovich*, 1976] which had reproduced the mechanics of Langmuir circulation but had relied upon assumptions of coherent surface wave structure.

Basic CL2 theory results in a set of equations that are familiar, with the addition of a vortex force term due to the interaction of the Stokes drift and the mean current. This is presented by *McWilliams et al.* [1997] in the form

$$\frac{D\mathbf{v}}{Dt} + f\hat{z} \times (\mathbf{v} + \mathbf{u_s}) = -\nabla\Pi - g\hat{z}(\rho/\rho_0) + \mathbf{u_s} \times \omega + \mathbf{SGS}, \quad (1)$$

$$\frac{D\rho}{Dt} + \mathbf{u_s} \cdot \nabla\rho = SGS, \quad (2)$$

$$\nabla \cdot \mathbf{v} = 0, \quad (3)$$

where $\mathbf{v}$ is the velocity vector, $\mathbf{u_s}$ is the Stokes drift current, f is the Coriolis parameter, g is the gravitational acceleration, $\omega = \nabla \times \mathbf{v}$ is the mean current vorticity, SGS refers to a sub-grid scale parameterization for density mixing, and Π is a generalized pressure given by

$$\Pi = p/\rho + (1/2)[|\mathbf{v} + \mathbf{u_s}|^2 - |\mathbf{v}|^2]. \quad (4)$$

The major feature of these equations is the vortex force term, $F_v = \mathbf{u_s} \times \omega$, in the

momentum equation. This term gives rise to the roll instabilities that we associate with Langmuir circulation. The Stokes drift also advects density gradients and interacts with the Coriolis force in predictable ways; CL2 theory was later modified to allow for the Coriolis force [*Huang*, 1979; *Leibovich*, 1980]. There are additional subtleties that we will not address regarding the time averaging of the surface wave field [see *Leibovich and Yang*, unpublished].

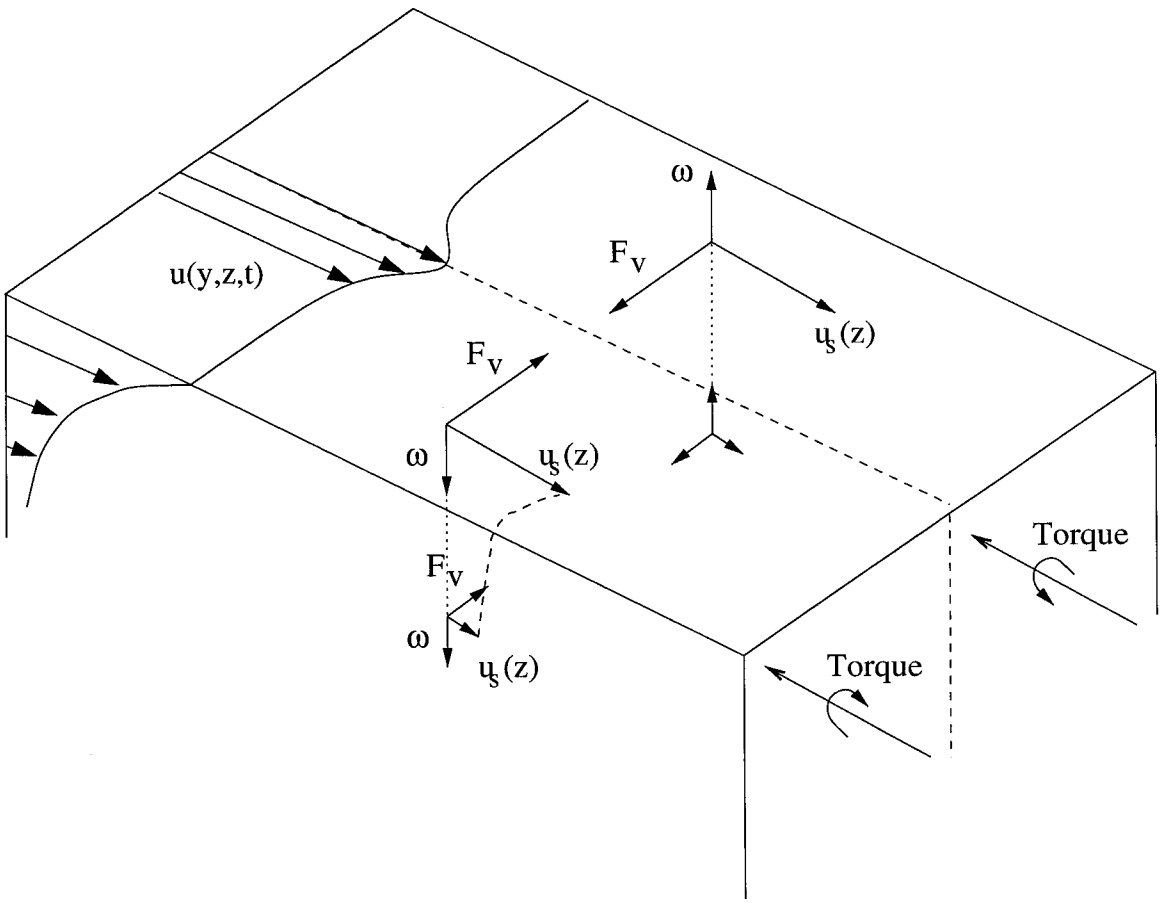

Figure 3: A cartoon illustrating the instability mechanism that leads to Langmuir circulation in CL2 theory. Vertical variation in the Stokes drift current leads to vertical variations in the vortex force and causes a torque leading to overturning.

The dynamics of the CL2 mechanism are represented in figure 3. Given a horizontally uniform current, $U(z)$, assume that there arises a small span-wise perturbation, $u(y,z,t)$. This gives rise to vertical vorticity ($\omega_z = -\frac{\partial u}{\partial y}$) and a horizontal vortex force, $\mathbf{F_v} = -\mathbf{u_s}\omega_\mathbf{z}\mathbf{j}$, that is directed toward the maximum in $u(y,z,t)$. This causes an acceleration toward this maximum where, by continuity, the fluid must sink. Assuming that $\frac{\partial U}{\partial z} > 0$ and ignoring shear stresses, application of conservation of x-momentum shows that as the fluid sinks $u(y,z,t)$ must increase. Therefore a current anomaly leads to convergence and amplification which in turn amplifies the convergence, in the absence of frictional effects. From a kinematic view, the vertical vorticity of the current anomaly is rotated by the Stokes drift and stretched by the shear, leading to convergence and amplification of the anomaly [*Leibovich*, 1983].

These theories are all two-dimensional in nature, in that they assume that the vortex pairs extend infinitely in the down-wind direction. More modern theory, spurred by observations of short vortex pairs and pairs that join at a Y-junction, has begun to examine the instabilities of the windrows in the down-wind direction [*Leibovich and Tandon*, 1993; *Tandon and Leibovich*, 1995].

2.1.1 The Langmuir Number

Leibovich [1977a] showed that for the two-dimensional problem, with constant forcing, that there is only one governing non-dimensional number. He called this the Langmuir number

$$La = \left(\frac{\nu_t^3 k^2}{\omega a^2 u_*^2}\right)^{1/2}, \tag{5}$$

where ν_t is the eddy viscosity, $u_* = \sqrt{\tau/\rho}$ is the friction velocity, and the surface waves have an intrinsic frequency, ω, wavenumber, k , and amplitude, a. The Langmuir number can be interpreted as a ratio of the diffusion of streamwise vorticity to the production of streamwise vorticity [*Leibovich*, 1983]. It can also be interpreted as an inverse Reynolds number.

The three-dimensional problem is typically characterized by two non-dimensional numbers, the Langmuir number, $La = 2S_0/u_*$, and a Reynolds number, $Re = u_* d/\nu_t$, where d is a depth scale, such as the mixed-layer depth or the surface-wave e-folding depth $(1/\beta)$ [*Leibovich and Yang*, unpublished]. *McWilliams et al.* [1997] used two related scalings, the turbulent Langmuir number, $La_{tur} = \sqrt{u_*/S_0}$, and the laminar Langmuir number, $La_{lam} = \sqrt{u_*/S_0 Re^3}$.

2.2 The Large Eddy Simulation (LES) Model

The model is based upon the 3-D LES model of *Skyllingstad and Denbo* [1995], which solves the equations 1 to 3. Although the original model did not include the rotational Stokes drift term, $f\hat{z} \times \tilde{u}_s$, this model does use this term. However we simplify by ignoring the variation of the flow field in the wind direction and representing the effect of sub-grid scale turbulence by a constant eddy viscosity. The model is forced by the wind stress at the surface boundary and has a radiative condition on the bottom boundary. The numerical model has a resolution of 256 (cross-wind) $\times$ 60 (vertical) grid points and a grid spacing $\Delta x = \Delta z = 1\ m$, but higher-resolution runs with 512 (horizontal) $\times$ 120 (vertical) grid points were also computed to test the model's sensitivity to resolution. The time step was chosen to be $\Delta t = 0.5\ s$. The model results were found to be insensitive to the initial condition, but I usually initialized the flow field with a fully developed

circulation field to speed up the cell spin-up process. Surface waves were assumed to propagate in the wind direction, and the induced Stokes drift current had a surface velocity $2S_0 \approx 0.2\ m\,s^{-1}$ and an e-folding depth of $\frac{1}{2\beta} \approx 1.25\ m$. In fully developed sea conditions, this forcing corresponds to a wind speed of $\approx 10\ m\,s^{-1}$. Forcing in the simulations was varied by adjusting the two remaining parameters, u_* and ν_t. Note that the model solves the equations in dimensional form, so that all non-dimensionalization takes place after the computation.

In the primary set of simulations, we fix the wind stress $\tau_w = \rho_w u_*^2$ with a friction velocity of $u_* \approx 0.01\ m\,s^{-1}$. We therefore fix the turbulent Langmuir number and the dynamics are entirely set by varying the Reynolds number through changes in the eddy viscosity, ν_t . In the 2-D model, the only dynamically important parameter is the dimensionless Langmuir number, equivalent to *McWilliams* laminar Langmuir number,

$$La_{lam} = \left(\frac{\nu_t \beta}{u_*}\right)^{3/2} \left(\frac{u_*}{S_0}\right)^{1/2} \tag{6}$$

[*Li and Garrett*, 1993].

A second set of simulations was performed to confirm the validity of using La_{lam} as the only relevant variable. In these simulations all four of the forcing variables could be adjusted to give a set of runs with the same laminar Langmuir number but varying turbulent Langmuir and Reynolds numbers. I found that the use of a single variable, the laminar Langmuir number, to describe the results is warranted and so I will discuss the the results in terms of La_{lam}, hereafter shortened to just La.

Figures 4 and 5 show snapshots of the vertical and downwind velocity fields

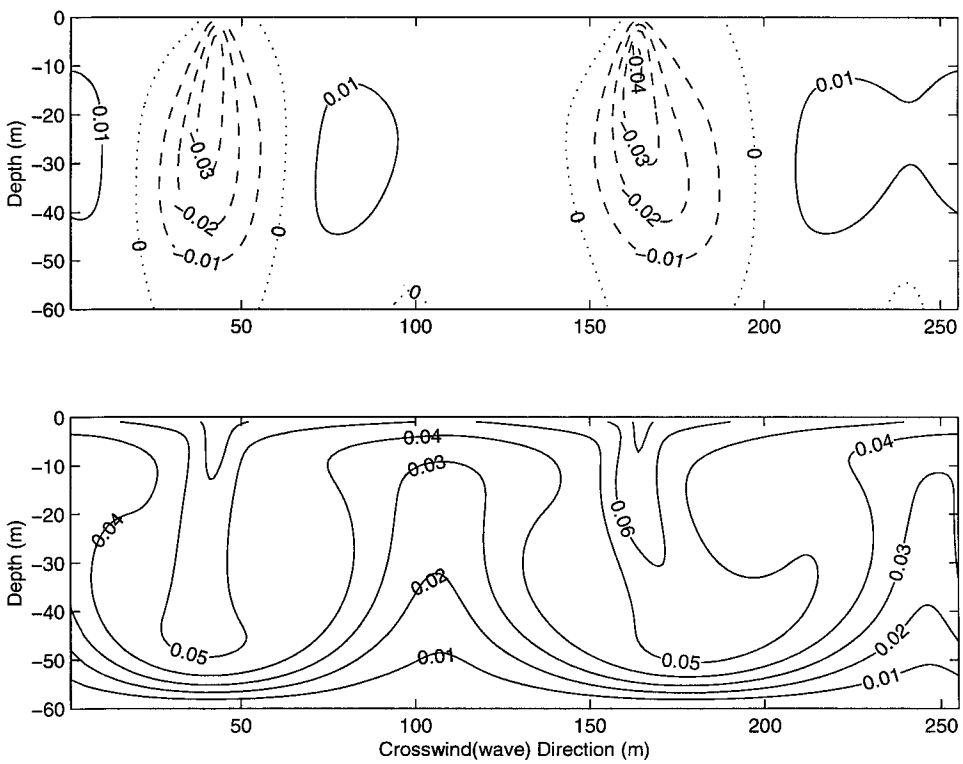

Figure 4: Distribution of the vertical (top) and downwind (bottom) velocities (ms^{-1}) in a cross-wind section at Langmuir number, La = 0.334. In this quasi-steady flow, large cells with nearly uniform size extend down to the bottom of the domain.

at two different Langmuir numbers. At $La = 0.334$, Langmuir cells merge until they reach a quasi-steady state as shown, for example, by *Li and Garrett* [1993]. However, at $La = 0.04$, Langmuir cells with different sizes coexist at all times. Large cells extend down to full depth while small cells appear near the surface. Small cells are constantly being generated near the surface where the Stokes drift forcing is strongest. They grow with time and merge with larger cells while new small cells are generated. Figure 6 shows the cell regeneration and amalgamation process in more detail as we follow the time evolution of the vertical velocity field. We note that in wall-bounded shear flows, the regeneration of streamwise vortices can only be simulated in computational domains that have a large width to depth aspect ratio [*Hamilton et al.*, 1995]. The computational box in our simulations has an aspect ratio of 4 or larger.

A set of 900 particles, in a grid pattern, was released into the Langmuir circulation field and was tracked over a 12-hour period. In addition to the advection by Langmuir circulation, the particles have an imposed random velocity component representing diffusion by the unresolved sub-grid scale turbulent flows. We assume that the turbulent diffusivity of particles is the same as the turbulent eddy viscosity. We treat the upper and lower boundaries as perfectly reflecting walls for particle motion. This is equivalent to a zero-flux boundary condition for particle concentration. Since the particles are released into a small region in the computational domain, there appeared to be some initial coherence between the particles within a few eddy turnover times. We start to calculate particles' spread and cross-wind diffusivity from a time (e.g., $\tilde{t} = 2$ hours or about two eddy turnover times) when the particles have already forgotten their initial locations.

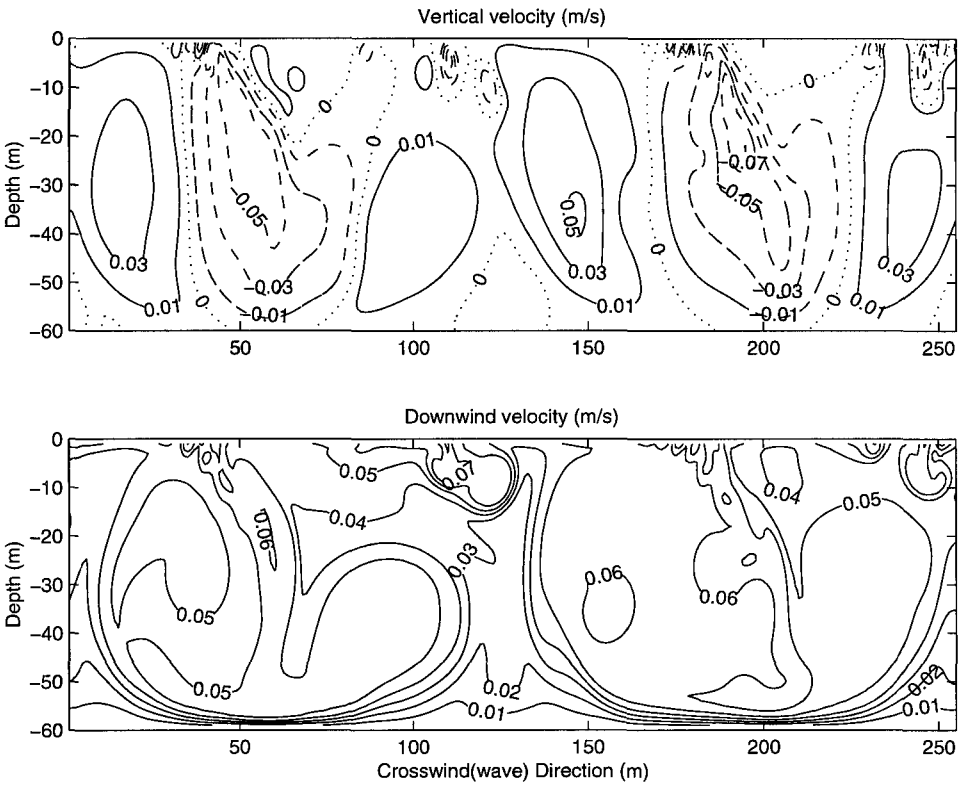

Figure 5: Distribution of the vertical (top) and downwind (bottom) velocities (ms^{-1}) in a cross-wind section at La = 0.040. In this snapshot of the flow field, we see a coexistence of multiple scales. Large cells extend down to the full depth, while small cells appear near the surface.

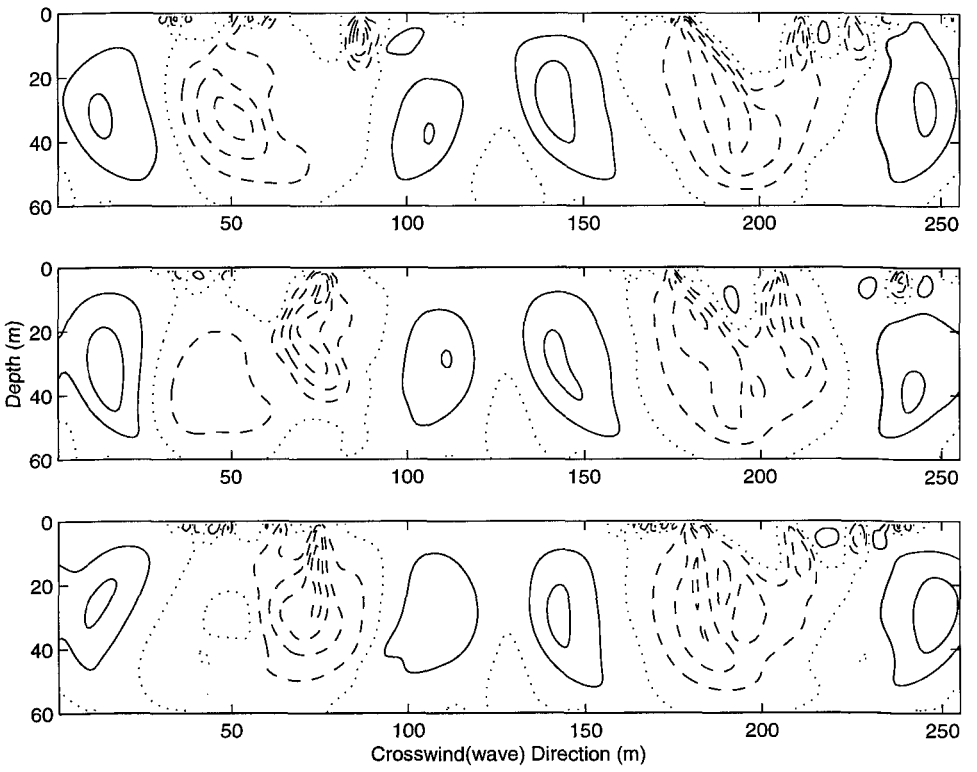

Figure 6: Three snapshots of the vertical velocity field at 12-minute intervals for La = 0.040. Small cells are generated near the surface, and grow and merge with the larger cells. Observe how a small cell (first appearing near x = 85m, top) grows and merges with another larger cell, while the cell regeneration and merging at right (near x = 200m) exhibits more complex behaviour.

2.3 Diffusivity

Csanady [1973] attempted to quantify diffusion in windrows, and stated that a windrow with a life time, T_c, may split into many windrows spaced at l_{cw}, where l_{cw} is the cross-wind spacing of the new windrows.. A purely dimensional argument for the cross-wind diffusivity gives

$$\kappa_y \propto l_{cw}^2 T_c^{-1}. \tag{7}$$

By running an idealized model (statistical and not based on fluid dynamical equations) for a time varying Langmuir circulation field, *Faller and Auer* [1988] found that windrow wandering and meandering are the main mechanisms for dispersion. The empirical fit to their simple model gave

$$\kappa_y = 0.5 \left(\frac{T_c v}{l_{cw}} \right)^{1/2} l_{cw}^2 T_c^{-1} \tag{8}$$

where v is the cross-wind current velocity. These two early attempts at quantifying the cross-wind diffusivity suffer for their dependence on the windrow lifetime, a quantity which is difficult to measure and which is itself dependent on other variables, such as the wind speed [*Farmer and Li*, 1995]. To use such an equation we would first have to make observations during all the conditions that we are seeking to replicate. This need for a predetermined look-up table makes these formulae impractical.

More recently, *Thorpe et al.* [1994] used sonar observations of convergence lines (i.e. bubble bands) to infer the surface dispersion of particles. They found that κ_y varies from 5×10^{-3} to $0.5\, m^2 s^{-1}$ and depends on the windrow life time,

T_c, the cross-wind velocity, v, the excess downwind velocity (i.e. the jet velocity minus the background velocity) in the convergence line jet, Δu, and the mean wind drift, $\overline{u}$. The model showed that the diffusivity generally increases with wind speed. Their sonars scanned the water surface in fixed directions and hence could not directly measure the surface distribution of convergence zones. Assumptions were made regarding the lifetime and length of convergence lines. These semi-empirical models based on actual observations of bubble bands can be used to estimate cross-wind diffusivities at specific field locations, though the results obtained cannot be easily generalized.

2.4 Results

There are two methods that can be used to calculate the cross-wind diffusivity. In the first method, the variance of particles' locations in the cross-wind direction, σ_y^2 ,is calculated as a function of time. Then the cross-wind diffusivity is obtained from [cf. *Csanady*, 1973]

$$\kappa_y = \frac{1}{2}\frac{d\sigma_y^2}{dt}. \tag{9}$$

If a linear fit is made to the time series of the variance, the diffusivity is the slope of the fitted line. In the second method, proposed by *Taylor* [1921], diffusivity can be calculated as the product of the variance of the particle cross-wind velocities and the Lagrangian integral time-scales. Taylor's method is usually more efficient, as it requires a smaller number of particles to be tracked. In our calculations the diffusivities obtained from the two methods were found to agree within 10%.

2.4.1 Neutrally Buoyant Particles

In this section we investigate the dispersion of neutrally buoyant particles. These are passive tracers of the flow field. Figure 7 plots the variance σ_y^2 as a function of time for various Langmuir numbers in the range of 0.02 to 0.7. The variances increase linearly with time for all values of La. However, particles are occasionally clustered and move together into an adjacent Langmuir cell, temporarily causing deviations from the persistent linear trend. Notice also the high correlation of the floats in the initial, discarded segment of the simulation. The slope of the line generally increases as the Langmuir number decreases.

To derive a parameterization for the cross-wind diffusivity, we convert the dimensional quantities (tilde) into non-dimensional ones (no tilde) by using the following formulae [cf. *Li and Garrett*, 1993]:

$$\begin{aligned} \tilde{u} &= u_*^{4/3} S_o^{-1/3} La^{-2/3} u, \\ (\tilde{v}, \tilde{w}) &= u_*^{2/3} S_0^{1/3} La^{-1/3} (v, w), \\ \tilde{t} &= u_*^{-2/3} S_0^{-1/3} \beta^{-1} La^{1/3} t, \\ \tilde{\Omega} &= u_*^{2/3} S_0^{1/3} \beta La^{-1/3} \Omega, \\ (\tilde{y}, \tilde{z}) &= \beta^{-1} (y, z), \end{aligned} \tag{10}$$

where Ω is a streamfunction in the y-z plane.

The cross-wind diffusivity has a dimension of $1/(\beta^2 \tilde{t})$. Using (6) and (10), we obtain

$$\tilde{\kappa}_y = \frac{u_*}{\beta} \left(\frac{S_0}{u_*} \right)^{1/3} La^{-1/3} \kappa_y. \tag{11}$$

Since $\kappa_y(La)$ is a function of La, I can redefine κ_y to include the $La^{-1/3}$ term and

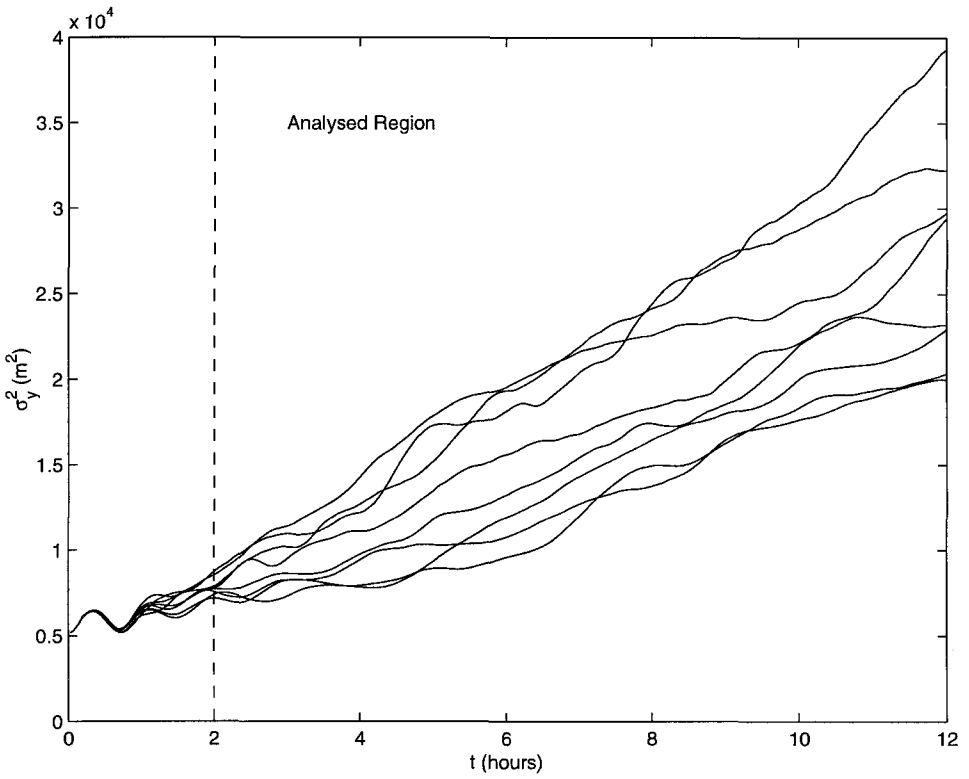

Figure 7: Time series of the variance of particles' locations in the cross-wind direction. Langmuir numbers range from 0.02 to 0.7. The variance increases with time for all Langmuir numbers. The dashed line denotes the time at which the analysis of particle dispersion begins.

thus obtain a non-dimensionalization that depends only on u_*, β and S_0.

Figure 8 summarizes the non-dimensional cross-wind diffusivities which are calculated from time derivatives of the variances. At each La we obtain three estimates of κ_y by averaging over three lengths of time series records starting from $t_0 = 160$ (Figure 8, pluses), 240 (Figure 8, stars) or 320 (Figure 8, circles) minutes. There is only a small spread between the three estimates.

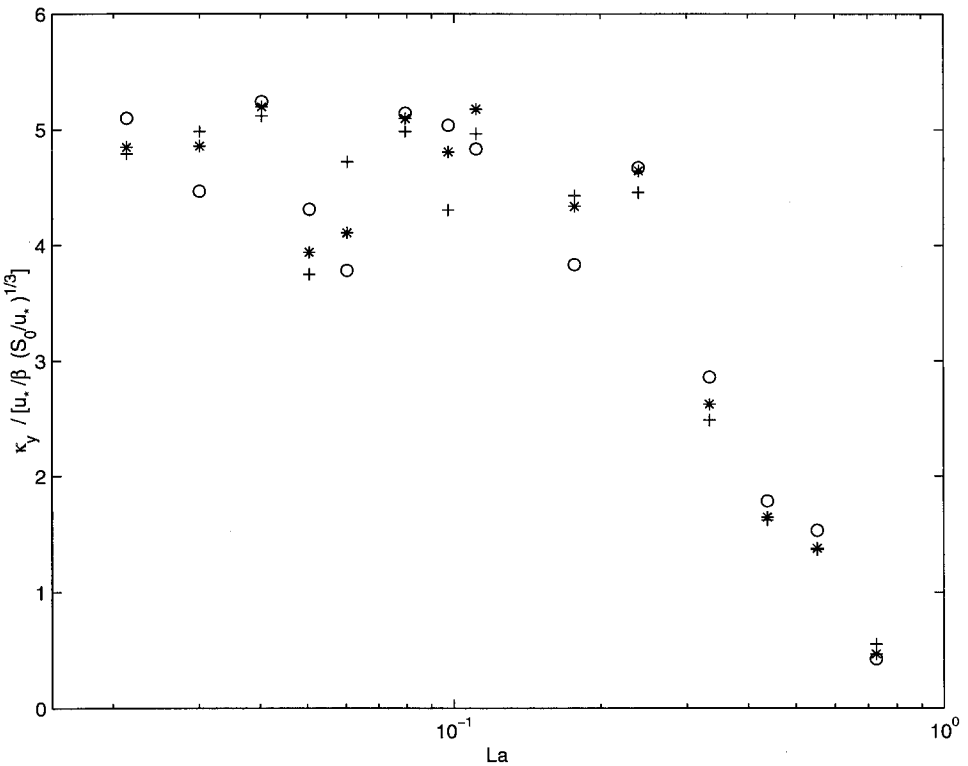

Figure 8: Nondimensional cross-wind diffusivity κ_y versus Langmuir number La for neutrally buoyant particles. Three estimates of κ_y are obtained for each La by averaging over different lengths of time starting from $t_0 = 160$ minutes (plus), $t_0 = 240$ minutes (star) and $t_0 = 320$ minutes (circle).

We see that the non-dimensional diffusivity in figure 8 approaches a constant value of $\kappa_{yC} \approx 4.5$ at small La. If I replace the function $\kappa_y(La)$ in (11) with this

constant, then I obtain a parameterization for the dimensional cross-wind diffusivity (which holds for low Langmuir numbers).

In fully developed seas, the Stokes drift current has a surface drift velocity $2S_0 = 0.016U_w$ and an e-folding depth of $1/(2\beta) = 0.12U_w^2/g$, where U_w represents the wind speed measured 10 meters above the oceans surface [*Kenyon*, 1969]. The friction velocity can be written as

$$u_* = \left(\frac{\rho_a}{\rho_w} C_D\right)^{1/2} U_w \tag{12}$$

[*Gill*, 1982]. Thus at small La,

$$\begin{aligned} \tilde{\kappa}_y &= \frac{u_*}{\beta}\left(\frac{S_0}{u_*}\right)^{1/3} \kappa_{y_C}, \\ &= \left(\frac{\rho_a}{\rho_w} C_D\right)^{1/3} \frac{0.048 U_w^3 \kappa_{y_C}}{g}. \end{aligned} \tag{13}$$

Assuming $\rho_a/\rho_w = 1.26 \times 10^{-3}$, $3.5 \leq \kappa_{y_C} \leq 5$, and $0.001 \leq C_D \leq 0.003$, one obtains

$$1.9 \times 10^{-4}\, s^2\, m^{-1} \leq \frac{\tilde{\kappa}_y}{U_w^3} \leq 3.8 \times 10^{-4}\, s^2\, m^{-1}. \tag{14}$$

The results that are shown in figure 8, and which lead to the parameterization above, are the result of a series of runs where the friction velocity, and thus the turbulent Langmuir number, were held constant while the eddy viscosity, and thus the Reynolds number, were varied. Although this is reasonable, given that the only important parameter in the problem is the laminar Langmuir number, it is also worthwhile to check that this assumption holds in the model. We therefore calculated the diffusivity for several sets of runs where the laminar Langmuir number was held constant but the turbulent Langmuir number changed. The variation

between these runs was no greater than the spread in figure 8.

In the above numerical runs, we assume that the sub-grid scale eddy diffusivity is the same as the eddy viscosity. This is not an unreasonable assumption because turbulent flows should transport momentum and tracers at about the same rate. We have examined the model's sensitivity to the turbulent Prandtl number. If the eddy diffusivity applied to the particles is 10 times larger than the eddy viscosity, the estimated cross-wind diffusivity has a functional form similar to that of Figure 8, though the asymptotic value increases by about $\sim 70\%$ (not plotted).

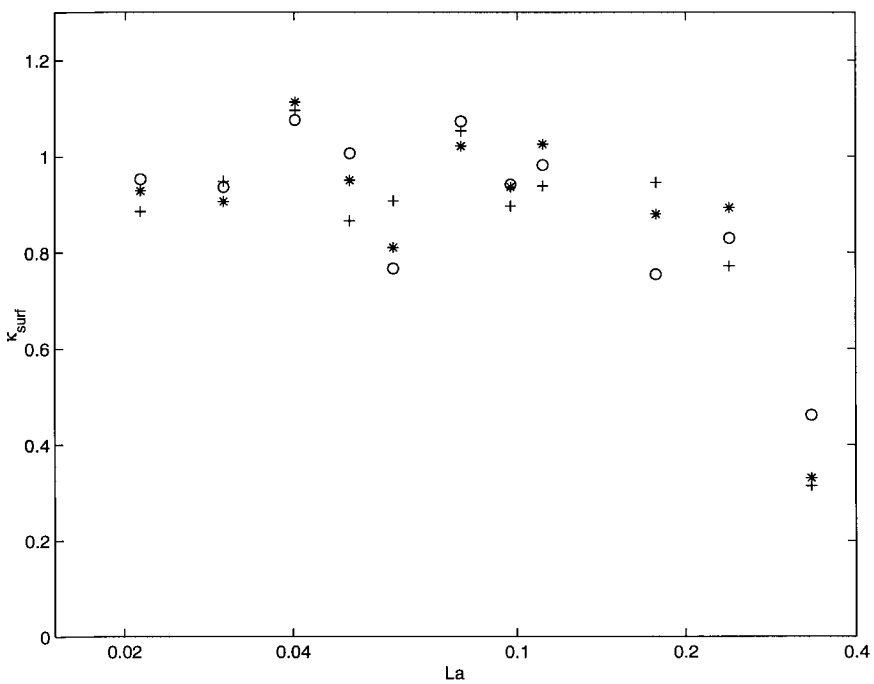

Figure 9: Cross-wind diffusivity for surface-trapped floats as a function of La. Symbols are as in figure 8.

So far, we have studied the dispersion of neutrally buoyant particles which are free to move within Langmuir cells. Dispersion of these particles is different from that of surface-trapped particles investigated by *Thorpe et al.* [1994]. To

demonstrate this difference, we place an artificial barrier at some depth through which floats are not permitted to pass. A set of simulations was undertaken where the particles were constrained to lie effectively on the surface, i.e., within the first subsurface grid box (of 1 m depth). The results of these runs are shown in figure 9. For $La \geq 0.4$, the estimated diffusivity is very small and is not plotted. For $La \leq 0.4$, the diffusivity is $\sim 20\%$ of that for unconstrained particles (figure 8). Again, the remarkable result is that the cross-wind diffusivity approaches a constant at small values of La. Because the particles are prevented from moving downward and advecting around cells, they remain trapped in surface convergence zones until the cells disintegrate or new cells are generated. Hence the surface-trapped floating particles have much smaller cross-wind diffusivities. If the barrier depth is placed deeper than the depth of maximum downwelling velocity in Langmuir circulation, the diffusivity is found to be comparable to that for the unrestrained particles.

The cross-wind diffusivity predicted by the model compares favorably with the diffusivity estimates inferred from sonar images of bubble clouds. At a wind speed of 10 $m\,s^{-1}$, our model for surface-trapped floats gives a diffusivity in the range of $0.06\ m^2\,s^{-1} \leq \tilde{\kappa}_{surf} \leq 0.08\ m^2\,s^{-1}$. This is within the range $0.005\ m^2\,s^{-1} \leq \tilde{\kappa}_y \leq 0.5\ m^2\,s^{-1}$ obtained by *Thorpe et al.* [1994]. Our model for neutrally buoyant unconstrained floats, equation 14, predicts a diffusivity in the range of $0.19\ m^2\,s^{-1} \leq \tilde{\kappa}_y \leq 0.38\ m^2\,s^{-1}$ at a wind speed of 10 $m\,s^{-1}$.

2.4.2 Buoyant Particles

Buoyant particles such as bubbles and oil droplets lie somewhere between neutrally buoyant particles and floating particles. Depending on its size (radius) and

its density difference with the surrounding water, a particle rises in still water at a speed $\tilde{w}_b$. If the drop Reynolds number is small, we have

$$\tilde{w}_b = \frac{2ga^2(1 - \rho_a/\rho_w)}{9\nu_w} \tag{15}$$

where a is the drop radius; ρ_a and ρ_w are the densities of air (or oil) and water, respectively; and ν_w is the kinematic viscosity of sea water [*Batchelor*, 1967]. For large drops where the drop Reynolds number (Re_d) is greater than 1, we use an empirical formula of *Clift et al.* [1978]. Table 1 displays drop rise speeds and drop Reynolds numbers for typical oil droplets and air bubbles. We have taken $\nu_w = 10^{-6}\ m^2\ s^{-1}$, $\rho_a/\rho_w = 1.3 \times 10^{-3}$, and $\rho_0/\rho_w = 0.9$. Similarly, we could consider the rise speed of water-in-oil emulsions (chocolate mousse), which has a density between that of oil and water, $\rho_{mousse} \approx 970\ kg\, m^{-3}$.

Radius, μm	Oil $\tilde{w}_b$, $m\, s^{-1}$	Air $\tilde{w}_b$, $m\, s^{-1}$	Re_{oil}	Re_{air}
10	2.2×10^{-5}	2.2×10^{-4}	4.4×10^{-4}	4.4×10^{-3}
20	8.7×10^{-5}	8.7×10^{-4}	3.5×10^{-3}	0.035
50	5.5×10^{-4}	5.4×10^{-3}	0.055	0.55
100	2.2×10^{-3}	0.017	0.44	4.4
200	6.4×10^{-3}	0.043	3.48	35
500	0.028	0.27	28	273

Table 1: Relation between droplet size and buoyant rise speed $\tilde{w}_b$ obtained from empirical formulas [*Clift et al.*, 1978]

We now track the movement of these buoyant particles (or floats) as they rise under their buoyancy and are advected by Langmuir cells. Figure 10 shows the time-averaged cumulative float density for $La = 0.046$ and at three buoyant rise speeds. A deviation from the general linear trend denotes a more or less densely

populated portion of the water column. For neutrally buoyant particles, the particle concentration has a constant distribution with depth, but more buoyant particles are trapped near the surface as $\tilde{w}_b$ increases. Figure 11 shows the percentage of floats trapped near the surface (within 0.5 m of the surface in the model) as a function of La and w_b. Here w_b is non-dimensionalized using equation 10.

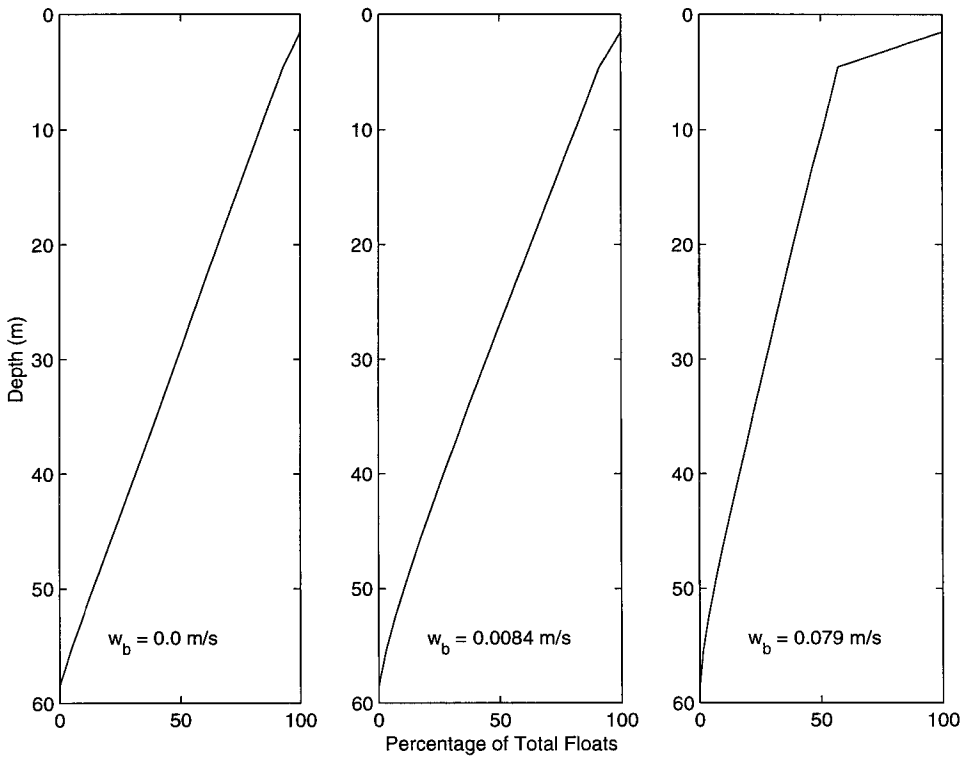

Figure 10: Cumulative float density as a function of depth for three different buoyant rise speeds w_b at $La = 0.046$.

It is illuminating to compare the particle rise speed with the downwelling velocity in Langmuir circulation. On the basis of numerical model results and scaling analysis, *Li and Garrett* [1993] obtained, for the maximum downwelling velocity, $\tilde{w}_{down} \propto u_*^{2/3} S_0^{1/3} La^{-1/3}$. When $\log(La)$ is compared to $\log(\tilde{w}_{down})$ for

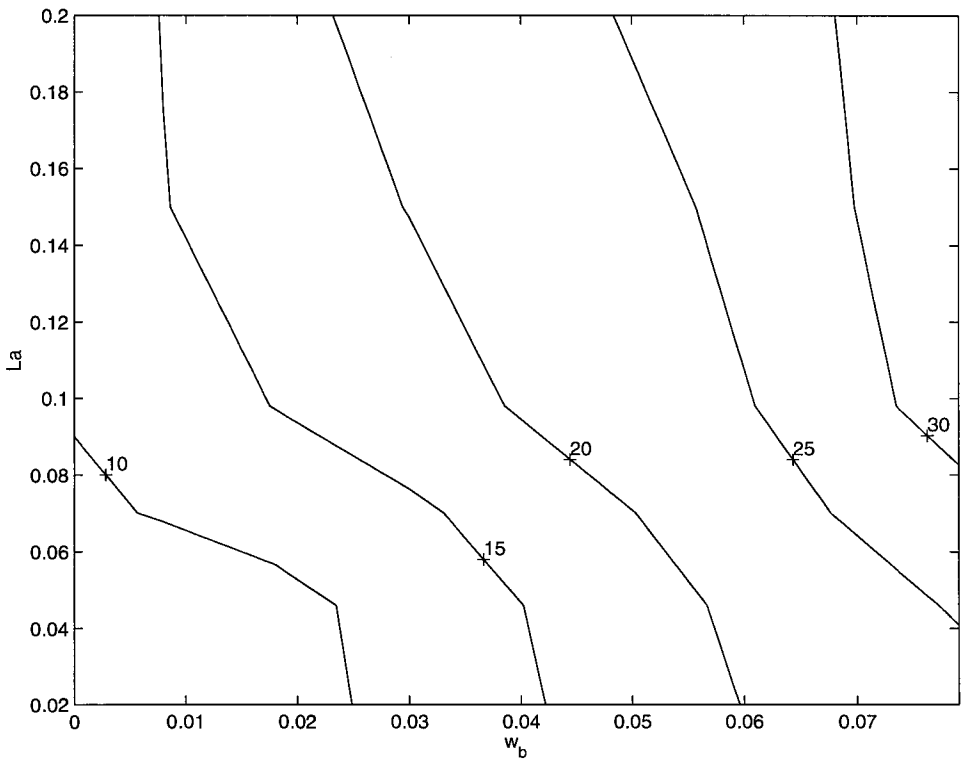

Figure 11: Percentage of floats trapped near the surface as a function of w_b and La. The contours are constructed from 28 data points through linear interpolation and smoothing.

a subset of the runs, we found good agreement with the predicted $La^{-1/3}$ dependence. The constant of proportionality is found to be $w_0 = 1.4 \pm 0.2$. This gives an empirical formula

$$\tilde{w}_{down} = w_0 u_*^{2/3} S_0^{1/3} La^{-1/3} w_{down}. \tag{16}$$

Figure 12 shows the cross-wind diffusivity as a function of La and w_b/w_{down}. When w_b/w_{down} is small, κ_y approaches the value for neutrally buoyant particles. When w_b/w_{down} is large, it approaches that for surface-trapped particles. We find that even when particle rise speed is only a small fraction of the downwelling velocity, the cross-wind diffusivity is reduced substantially. In particular, we find that for floats with $w_b = 0.05\, w_{down}$, the cross-wind diffusivity is reduced by about 20%.

Motivated by dispersion of oil droplets resulting from oil spills, we re-plot Figure 12 using drop radius as the horizontal axis. Using the values from Table 1, we obtain operational plots of the diffusivity as a function of bubble diameter and Langmuir number (Figure 13).

2.5 Discussion

The asymptotic behaviour of the non-dimensional cross-wind diffusivity at small Langmuir number (figure 8) leads to a simple parameterization. This parameterization is of particular use since it is independent of the unknown sub-grid scale eddy viscosity. Instead it depends on more easily determinable properties of the wave and wind forcing, which themselves can be related directly to the wind speed. This is a strong advantage over previous attempts that either relied

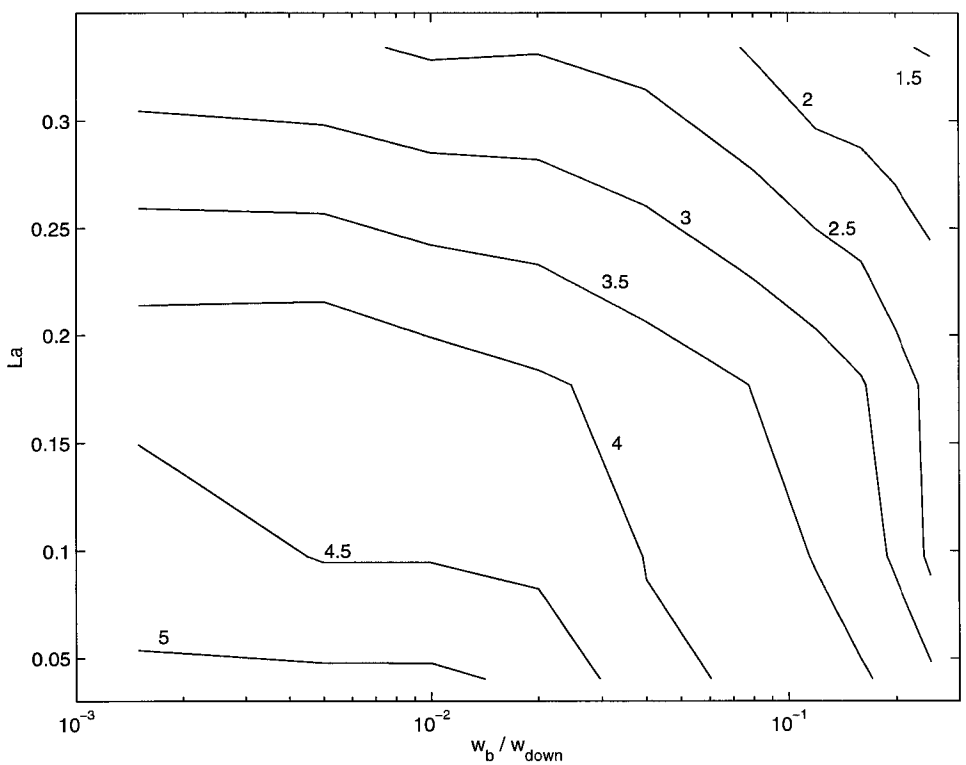

Figure 12: Cross-wind diffusivity as a function of La and w_b/w_{down}. Contours are constructed using 28 data points through linear interpolation and smoothing. The uncertainty in the diffusivity is estimated to be ± 0.5.

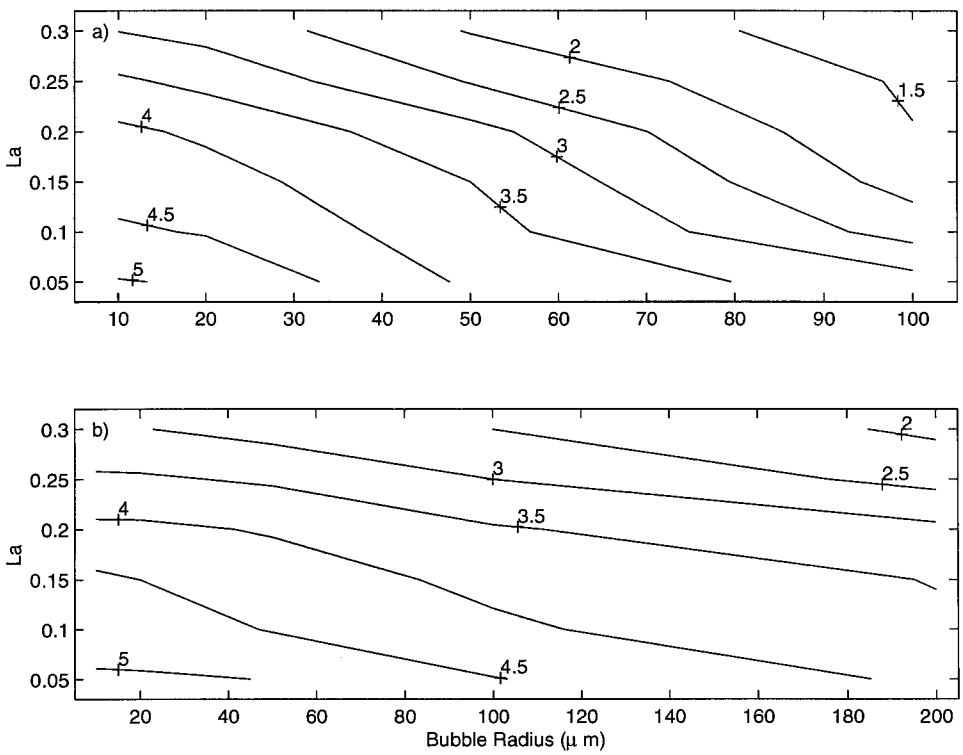

Figure 13: Cross-wind diffusivity for (a) air bubbles and (b) oil droplets as a function of droplet radius and Langmuir number.

on difficult to determine variables or were restricted to specific conditions of applicability.

The asymptotic behaviour is itself unexpected. Before the results of these experiments I would have predicted that the diffusivity increased as the Langmuir number was decreased, due to the increasing strength of the circulations (which it does for large Langmuir numbers). However, the existence of a competing process that limits this growing diffusivity was not expected. It appears that the decreased lifetime of the Langmuir circulation cells may provide this counter-balance to the increased strength of the cells.

Buoyant particles have smaller cross-wind diffusivity, even when their buoyant rise speeds are only a small fraction ($< 5\%$) of the maximum downwelling velocity in Langmuir circulation. The predicted surface-trapped diffusivity is in good agreement with previous observation-based estimates. The significant reduction in diffusivity for buoyant (and surface trapped) floats, as opposed to neutrally buoyant floats, implies that caution needs to be used in applying bubble cloud observations to calculate the diffusivity of a neutrally buoyant tracer.

A major limitation of this study is that we have only considered particle dispersion in a section perpendicular to the wind direction. We have assumed that Langmuir circulation is composed of longitudinal vortices and windrows are parallel to the wind direction. However, observations have shown that windrows or bands of bubble clouds can organize into nonlinear patterns and sometimes join together to form Y-shaped junctions at high winds [e.g., *Farmer and Li*, 1995]. Using a LES model, *Skyllingstad and Denbo* [1995] have found that surface floats released into the Langmuir circulation field tend to congregate at these junctions but with less organized structure than the observations of *Farmer and Li* [1995].

In later studies, *McWilliams et al.* [1997] and *Leibovich and Yang* [unpublished], found similar nonlinear distributions of surface floats. *McWilliams et al.* [1997] also gave particle trajectories over a period of 24 minutes. Unfortunately, this sampling time appears to be too short to obtain a reliable estimate of cross-wind diffusivity that we can compare with the 2-D model.

Despite these limitations, the 2-D model is a useful first step toward obtaining a parameterization of particle dispersion in Langmuir circulations. It is difficult to directly compare this parameterization with previous work, since much of the previous work was semi-empirical and based upon poorly known parameters. However, if I estimate the unknown parameters using rough guesses from the computations, then we find that the previous parameterizations tend to overestimate the diffusivity, particularly at low Langmuir numbers.

3 Theory

Before embarking on the data analysis it is important to understand the context of the thesis in terms of previous work. It will also be necessary to develop some new theory to help explain the observations. I first start with Reynolds stresses and some related boundary layer theory. I then explain internal waves and vortical modes and discuss some of their expected features. I finally examine the effect of the Doppler shift on the preceding sections.

I will focus on two medium scale processes in the data analysis: internal waves and vortical modes. The choice of these two, and only two, processes is motivated by a normal mode decomposition of the equations of motion for a linearly stratified, unbounded ocean, on an f-plane. Following *Lien and Müller* [1992], the linear equations of motion can be rewritten in terms of three new prognostic variables; the horizontal divergence ($HD = \frac{\partial u}{\partial x} + \frac{\partial v}{\partial y}$), the vertical component of the relative vorticity ($RV = \frac{\partial v}{\partial x} - \frac{\partial u}{\partial y}$), and the vortex stretching ($VS = f\frac{\partial \eta}{\partial z}$). Here u and v are horizontal velocities in the x and y directions and η is an isopycnal displacement. This allows us to write

$$\frac{\partial \hat{\psi}(\mathbf{k},\mathbf{t})}{\partial t} + M(\mathbf{k})\hat{\psi}(\mathbf{k},\mathbf{t}) = \mathbf{0},$$

where $\hat{\psi}(\mathbf{k},\mathbf{t})$ is the wavenumber Fourier coefficient of $\psi(x,t) = (HD, RV, VS)$ and M is the matrix

$$M(\mathbf{k}) = \begin{pmatrix} 0 & -f\frac{m^2}{k^2+l^2+m^2} & -\frac{N^2}{f}\frac{k^2+l^2}{k^2+l^2+m^2} \\ f & 0 & 0 \\ f & 0 & 0 \end{pmatrix}.$$

Solving for eigenvalues and eigenvectors yields three solutions, two of which represent linear internal waves, with appropriate dispersion relations. The third eigenvector has zero intrinsic frequency, satisfies the thermal wind equation, and is horizontally non-divergent. It is also evident that the internal waves do not modify the underlying potential vorticity, while the third eigenvector does. This third eigenvector is a steady geostrophic current, and represents the linear limit of the vortical mode. *Lien and Müller* [1992] also discuss weakly non-linear systems where the third eigenvector is in cyclo-geostrophic balance.

The important point to understand is that equations of motion have three prognostic variables (u, v and η, as well as the diagnostic variables w and P), but that the eigenvectors of the system can be characterized by only two processes. One of these processes is internal waves and the other process is vortical modes.

3.1 Reynolds Stress

The Reynolds stress terms arise from the decomposition of the Navier-Stokes equation into a time mean and a fluctuating component. The instantaneous velocity becomes $\tilde{U}_i = U_i + u_i$, the pressure becomes $\tilde{p} = P + p'$, and the density becomes $\tilde{\rho} = \overline{\rho} + \rho'$. Here a variable with a tilde represents the instantaneous measure which is decomposed into a mean, the first variable on the right hand side, and a fluctuation, the second variable. Substituting this decomposition into the momentum equations and taking the time average gives

$$\frac{\partial U_i}{\partial t} + U_j \frac{\partial U_i}{\partial x_j} = -\frac{1}{\rho_0}\frac{\partial P}{\partial x_i} - g\frac{\overline{\rho}}{\rho_0} + \frac{\partial}{\partial x_j}\left(\nu_{mol}\frac{\partial U_i}{\partial x_j} - \overline{u_i u_j}\right) \qquad (17)$$

[*Kundu*, 1990]. This equation is identical to the original Navier-Stokes equation for the mean flow variables except for the last term, $\frac{\partial}{\partial x_j}(\overline{u_i u_j})$. This term represents an additional stress imposed upon the mean flow by the correlated movement of the fluctuating, or turbulent components. The tensor $-\rho_0 \overline{u_i u_j}$ is called the Reynolds stress tensor.

It is important to recognize that the Reynolds stress tensor is symmetric and hence can be diagonalized. In physical terms this means that there exists a reference frame in which the cross-product stresses ($\overline{u'v'}$, $\overline{u'w'}$, $\overline{v'w'}$) are all zero.

3.1.1 Reynolds Stress in a Simple Shear Flow

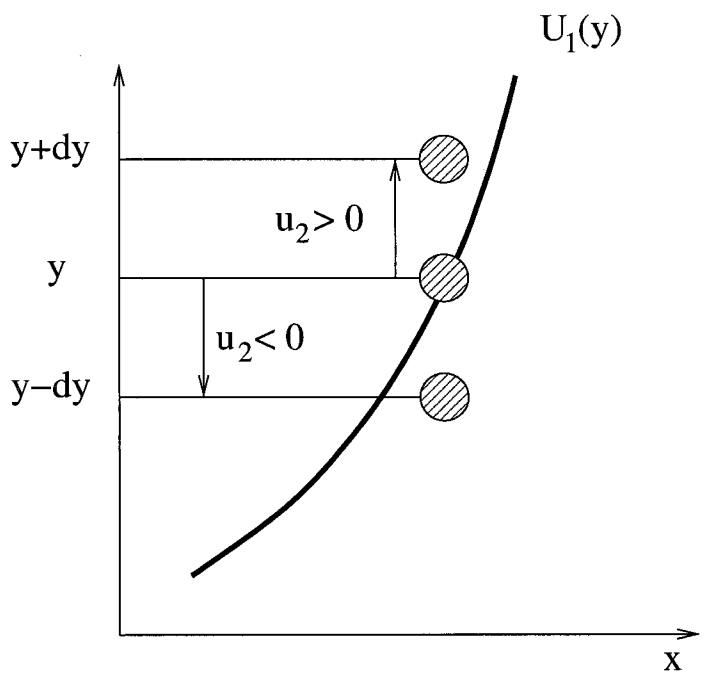

Figure 14: A particle fluctuating in a mean shear flow leads to a non-zero Reynolds stress [after *Kundu*, 1990].

The easiest example of how the correlation of two fluctuating velocities would

not average to zero, even though the velocities themselves do average to zero, is a simple shear flow. Consider the mean flow represented by the curve $U_1(y)$ in figure 14. If a particle initially located at position y is advected to the new position $y+dy$ then it will find itself moving slower then the surrounding flow. An observer at this new location would see less flow in the x-direction ($u_1 < 0$) and a positive flow in the y-direction ($u_2 > 0$). Therefore $u_1 u_2$ would be negative. Consider now a particle from y_0 that is advected to $y - dy$. In this case we would have $u_1 > 0$, since the particle is moving faster then the surroundings, and $u_2 < 0$, since the particle is moving in the negative y-direction. Again this gives the product $u_1 u_2 < 0$. The long term average value of this Reynolds stress component, $\overline{u_1 u_2}$, would be non-zero and negative.

It is not the Reynolds stress itself that appears in the mean momentum equation, but rather its spatial derivative. Therefore the existence of a non-zero Reynolds stress at a given location does not imply that the fluctuations are acting to change the mean flow at that location. It is only a divergence or convergence in the Reynolds stress that influences the mean flow. For instance, consider a linear shear flow $U(y) \propto y$ on an infinite plane in the presence of spatially homogeneous turbulence. In this case the Reynolds stress is everywhere negative and everywhere of the same value, so that there is no effect of the turbulence on the mean flow. However, if we alter the flow by inserting a wall at $y = 0$ then there will be convergence at the boundary and the mean flow will be altered at the boundary. Similarly, if the mean shear flow is non-linear or the level of turbulent fluctuation has some spatial inhomogeneity then we expect gradients in the Reynolds stress.

Any Reynolds stress component is a relative measure, in that it depends upon the choice of axis. Although the vertical axis is obvious, the choice of x and y

axes is more difficult. To see that the Reynolds stress varies, consider the example given in figure 14 where the original Reynolds stress component $\overline{u_1 u_2}$ is negative. Now let us consider a rotation of the axis by 90° clockwise. This maps $u_1 \rightarrow u_2^*$ and $u_2 \rightarrow -u_1^*$, where the starred variables represent the new coordinate frame. Then clearly $u_1 u_2 \rightarrow -u_1^* u_2^*$, and the Reynolds stress component must now be positive. It is also fairly easy to show that the effect of rotation is continuous and so that there must be some intermediate angle at which the Reynolds stress component $\overline{u_1 u_2} = 0$. If we consider a full 360° circle then there will be four angles at which the Reynolds stress disappears, one in each quadrant. Therefore in the data analysis chapter, 5.3, I will need to justify the choice of axes.

3.1.2 The Concept of Eddy Viscosity

In many situations we would like to model the effect of fluctuations on the mean flow but we may not have adequate knowledge of the fluctuations to do this directly. An example would be an ocean general circulation model that wishes to predict the effect of the continental slope on a coastal current but does not have the resolution to capture all the internal waves, vortical modes, turbulence and other small-scale processes that create the Reynolds stress. We wish to parameterize the unknown Reynolds stress components in terms of the known mean flow velocities.

The eddy viscosity parameterization arises by analogy with the kinematic viscosity of molecular diffusion. In the mean momentum equation (17) the molecular viscosity is given by $\nu \frac{\partial U_i}{\partial x_j}$. An eddy viscosity can therefore be defined using

$$A_y \frac{\partial U}{\partial y} = -\overline{uv} = A_x \frac{\partial V}{\partial x}, \tag{18}$$

where $A_{x,y}$ is the eddy viscosity acting in the x- or y-direction. We have gained nothing so far since we have only shifted the uncertainty of $\overline{u_i u_j}$ into an uncertainty of A_x and A_y. The easiest parameterization follows directly from molecular diffusion where ν is a constant of the fluid. Therefore the simplest eddy viscosity would be a constant. It is often assumed that the horizontal fluctuations are isotropic, so that $A_x = A_y = A_H$, but that vertical fluctuations are constrained by stratification and scaling arguments. We therefore need only two numbers to model the mean flow, a horizontal (A_H) and a vertical (A_v) eddy viscosity.

There is however a problem with the above formulation of eddy viscosity. The same eddy viscosity can be defined in two ways (three if we include the z-momentum equation):

$$A_y \frac{\partial U}{\partial y} = -\overline{uv}, \tag{19}$$

and

$$A_y \frac{\partial V}{\partial y} = -\overline{vv}, \tag{20}$$

and similarly for A_x. Furthermore if we assume an isotropic eddy viscosity, A_H, we get four definitions. A problem arises because the eddy viscosities determined in these two different ways are not equal. If we consider a simple shear flow, $U(y)$, then (19) provides a well defined A_y.However in (20), $\overline{vv} = O(\overline{uv})$ but $\frac{\partial V}{\partial y} = 0$, which leads to an undefined eddy viscosity.

We can understand why the equation 20 is a poor definition for the eddy viscosity by recalling what happens in the isotropic turbulent case. In this case [see *Hinze*, 1975] we pull out a turbulent pressure and hence obtain an equation of the form

$$-\overline{u_i u_j} = -P_t \delta_{ij} + \epsilon_m \left(\frac{\partial U_i}{\partial x_j} + \frac{\partial U_j}{\partial x_i}\right).$$

Although a constant eddy viscosity is a gross simplification, it is still a fairly common parameterization in numerical modelling. The magnitude of the eddy viscosity should be scale dependent, since as resolution increases more processes are directly resolved and so the eddy viscosity represents less of these processes. Many ocean general circulation use constant eddy viscosity parameterizations due to the computational efficiency. There are, of course, numerous problems with using a constant eddy viscosity. For instance, it seems likely that near boundaries the fluctuations may have a different character and magnitude than in the middle of the ocean. Thus, coastal waters might require a different value of eddy viscosity then the deep ocean. There are many other potential problems as well, which leads us to seek better parameterizations of the eddy viscosity.

3.1.3 Flow in a Channel

Juan de Fuca Strait is a channel and thus one might assume that it resembles the case of laminar flow between two plates, or plane Poiseuille flow. The velocity in a *fully-developed* portion of the channel is given by

$$U(y) = -\frac{y}{A_H \rho_0} \frac{dP}{dx} \left(\frac{W}{2} - \frac{y}{2} \right), \tag{21}$$

where W is the channel width and x is the along channel direction [*Kundu,* 1990]. This is the expected parabolic form with a corresponding shear stress

$$\tau(y) = \frac{dP}{dx} \left(\frac{W}{2} - y \right). \tag{22}$$

However, in order for this to be the correct functional form of the along-strait velocity the boundary layers from the edges must have already merged (i.e. the

flow is *fully-developed*). However, the boundary layer needs space and time to develop, and so one needs to consider whether having merged boundary layers at the location of our observations is plausible. We assume that the boundary layer width grows, as one progresses away from the entrance, like

$$w_{bl}(x) = \sqrt{A_H x/U}. \tag{23}$$

We want to know what is the minimum diffusivity necessary to have merged boundary layers at the location of our observations. Since a half width of the strait is $w \approx 10km$, an rms velocity is $U = 0.5m/s$ and our moorings are located at $x \approx 50km$ from the Pacific end of Juan de Fuca Strait, this implies $A_H = 1000\, m^2/s$. This is a larger diffusivity than I would expect (as we will see in the data analysis), and hence we must be wary of analogies to simple channel flow problems.

In an oscillating flow we expect that the boundary layer might extend to $w_{bl} \approx \sqrt{A_H/\omega_{M2}}$. This would require $A_H \approx 1.5 \times 10^4 m^2/s$ for the boundary layers to join mid-strait. Again this is an unusually large value to expect for the diffusivity. These simple scaling arguments indicate that the flow in Juan de Fuca Strait might be best described as two independent sloping side walls (i.e. on a semi-infinite plane), rather than channel flow where the boundaries communicate with each other.

3.1.4 Wall-Bounded Shear Flow

The behaviour in a wall-bounded shear flow is a relatively old fluid dynamics problem and can be solved using dimensional arguments. Here we consider a

flow similar to that depicted in figure 14, but with a no-slip boundary at $y = 0$. In a flow with this geometry, the first two momentum equations become

$$\frac{\partial}{\partial y}(\overline{uv} - \nu\frac{\partial U}{\partial y}) = -\frac{1}{\rho_0}\frac{\partial P}{\partial x} \tag{24}$$

$$\frac{\partial}{\partial y}(\overline{vv}) = -\frac{1}{\rho_0}\frac{\partial P}{\partial y}. \tag{25}$$

Taking an x-derivative of (25), under assumptions of along-channel homogeneity, gives

$$0 = \frac{\partial^2 P}{\partial x \partial y}.$$

This implies that $\partial P/\partial x$ is independent of y and allows us to integrate (24) with respect to y and obtain

$$\overline{uv} - \nu\frac{\partial U}{\partial y} = -\frac{1}{\rho_0}\frac{\partial P}{\partial x}y + const. \tag{26}$$

For a vertical side wall, the constant of integration is $-u_*^2 = -\tau_0/\rho_0$ where u_* is called the friction velocity.

The solution has three functional forms depending upon distance from the wall. Nearest the wall is a viscous sublayer where the velocity is linear with distance from the wall (for a smooth wall only),

$$U(y) = \frac{yu_*^2}{\nu}. \tag{27}$$

This region typical extends from the wall ($y = 0$) out to $y \simeq 5\nu/u_*$ [*Kundu*, 1990].

Beyond this is the logarithmic layer where the the velocity profile obeys

$$U(y) = \frac{u_*}{K} \ln \frac{y u_*}{\nu} + C. \tag{28}$$

Here $K \simeq 0.41$ is the Karman constant and C is a constant determined by matching to the viscous sublayer. The log layer extends out to yu_*/ν of order several hundred, and is dependent on the Reynolds number of the flow (the log layer becomes thicker for larger Reynolds numbers) [*Kundu*, 1990].

This derivation assumes that the boundary is smooth, and needs to be modified if the boundary is rough. In the case where undulations in the boundary are of the order of or bigger than the width of the viscous sublayer, the logarithmic form still holds but is modified to

$$U(y) = \frac{u_*}{K} \ln \frac{y}{y_0}, \tag{29}$$

where y_0 is called the roughness parameter. For typical atmospheric flows the roughness parameter varies from $10^{-5}\ m$ over smooth mud flats to $1\ m$ over forested terrain. In an oceanographic context, *Ott* [2000] found that $y_0 = 0.006\ m$ was able to reproduce 50% of observed bottom boundary layer velocity profiles from his Juan de Fuca ADCP mooring.

The third, and largest, section of the boundary layer is characterized by a velocity defect law,

$$\frac{U(y) - U_\infty}{u_*} = F(y/\delta), \tag{30}$$

where U_∞ is the mid-stream velocity beyond the boundary layer, and δ is the width of the boundary layer. The exact functional form of the right hand side of the equation is not determinable from scaling arguments, but can be determined for certain specific geometries.

The log layer is characterized by a constant Reynolds stress, $\overline{uv}$, and a linear eddy viscosity of the form $A_H = Ku_*y$. The scaling arguments that lead to the log layer equation are based upon the assumption that the pressure derivative term in (26) is much less then the constant, u_*^2. We can therefore roughly determine the width of the log layer by deciding for what values of y this is a reasonable assumption.

There are a number of ways in which we can estimate the terms. *Ott* [2000] determined that the along-channel pressure gradient between Port Angeles and Neah Bay varied from a low of about $-0.5 \times 10^{-3} Pa/m$ in the winter to a high of $-5 \times 10^{-3} Pa/m$ in August. Furthermore from geostrophy

$$-\frac{1}{\rho_0}\frac{\partial P}{\partial x} = fV.$$

Assuming V is $0.03\, m/s$ (which is consistent with our data), then both methods give a value for the pressure term of about $3 \times 10^{-6} m/s^2$. However at tidal frequencies, we would expect that

$$-\frac{1}{\rho_0}\frac{\partial P}{\partial x} \approx \omega_{M_2} U \approx 10^{-4}\, m/s^2.$$

Estimating the friction velocity from the drag relation, $u_*^2 = C_D U^2$, would be incorrect on a sloping boundary since the horizontal stress is increased by a factor equal to the 1/slope. One can imagine that a layer of water intersects a greater area of the bottom when the bottom is sloped than when it is vertical. Thus we need to use $u_*^2 = C_D U^2/S$, where S is the slope. The velocity in our lowest ADCP bin, about 2.5 meters above the bottom, can reach 0.8 m/s and certainly is about 0.4 m/s rms. Drag coefficients are generally around 2×10^{-3}. The slope varies from

a high of about $1/6$ near the steepest side walls to about $1/30$ under the moorings. We shall compromise with $S = 1/10$. Thus $u_*^2 = 3 \times 10^{-3} m^2/s^2$, using the rms velocity value. This implies that the width of the log layer must satisfy the inequality

$$\begin{aligned} \frac{1}{\rho_0}\frac{\partial P}{\partial x} y &\ll u_*^2, \\ (3 \times 10^{-6}\, m/s^2)\, y &\ll 3 \times 10^{-3} m^2/s^2, \\ y &\ll 1000m. \end{aligned} \tag{31}$$

In the above I used the mean pressure gradient, but would have $y \ll 30\, m$ if we use the tidal frequency pressure gradient.

There could easily be changes in this result. The along-strait pressure gradient could be concentrated in a few specific locations leaving a much smaller value over most of the strait. Also, one could quibble about the value of the drag coefficient or the value of U. Therefore although we do not expect that a log layer would extend from the side walls out to the distance of our moorings, we will nevertheless check to see if the observations agree with log layer dynamics.

3.1.5 More Complex Boundary Layers

The simple boundary layers discussed above can easily become more complex in the real ocean where rotation, stratification, and sloping topography can all play a role. *Soulsby* [1983] discusses the effect of rotation and oscillating flow on the boundary layer of an unstratified ocean above a flat bottom. The results can be complicated but have a number of commonalities that can be discussed. The solution for oscillating flow in the presence of rotation is found by the superposition of

two distinct boundary layers; one which rotates in the clockwise direction and one which rotates in the counterclockwise direction. These two boundary layers each have a fixed spatial structure which rotates as a whole. However the superposition will vary spatially as the relative angle between the two components varies.

The thickness of the boundary layer and the phase will be different between the counterclockwise and clockwise components. This arises in the equations of motion because the counterclockwise component scales as $(\omega + f)^{-1}$, while the clockwise component scales like $(\omega - f)^{-1}$. Here ω is the frequency of the oscillatory flow and f is the Coriolis parameter. In the northern hemisphere at the latitude of Juan de Fuca Strait this means that at the M2 tidal frequency the counterclockwise component has a boundary layer that is about 7 times thicker than the clockwise component. In principle, the existence of stratification would modify these results by forcing a cap on some of the excessively large counterclockwise boundary layers.

A general result of this analysis is that the tide at the bottom boundary leads the tide further away. The exact phase lag between the boundary and the interior flow depends upon several factors including u_* and the roughness length, as well as ω and f. *Soulsby* [1983], using values of $u_* = 0.0126\,m$ and $z_0 = 0.0009\,m$ for the M2 tide at a similar latitude, found a theoretical phase lag of 4°. Field experiments have confirmed the existence of a phase lag and have frequently found large lags. For instance, *Ott* [2000] found M2 phase lags in Juan de Fuca Strait that exceed 20°, which at an M2 frequency translates to over 40 minutes.

This phase lag holds for oscillatory flow even in the absence of rotation and it therefore seems reasonable to expect a phase lag not just in the vertical direction, above a flat bottom, but also horizontally, away from a side wall.

3.2 Internal Waves

Internal waves are an ubiquitous and consequently well studied process in oceanography. As a first attempt, I will use linear internal wave theory unless otherwise noted.

Internal waves satisfy the dispersion relation,

$$\omega_i^2 = \frac{N^2(k^2 + l^2) + f^2 m^2}{k^2 + l^2 + m^2}, \tag{32}$$

where (k, l, m) are the three components of the wavevector, N is the buoyancy frequency, f is the Coriolis frequency and ω_i is the intrinsic frequency. The waves are thus constrained to a limited intrinsic frequency band set by the stratification and the Earth's rotation.

3.2.1 Internal Wave Consistency Relations

There are nine consistency relations which must be obeyed by linear internal waves in the full wavenumber-frequency space [*Lien and Müller* 1992a]. Consistency relations inter-relate the cross-spectral Fourier components of the prognostic variables from the equations of motion. Thus if one used two different sets of prognostic variables (ie (u, v, η) vs. (HD, RV, VS)), one would obtain two different looking sets of consistency relations. These relations depend upon the intrinsic wave properties, (k, l, m, and ω_i), as well as the imposed environmental factors, (N and f). The observations do not have direct measurements of the horizontal wavenumbers (k and l), so I will choose to use relations that do not depend upon them. This leaves us with two relations; the ratio of potential to horizontal kinetic energy, and the ratio of counterclockwise to clockwise kinetic energy.

These can be written

$$\frac{PE}{HKE} = \frac{N^2(\omega_i^2 - f^2)}{(N^2 - \omega_i^2)(\omega_i^2 + f^2)}, \tag{33}$$

$$\frac{CCW}{CW} = \frac{\omega_i^2 - f^2}{\omega_i^2 + f^2}. \tag{34}$$

The derivation of these expressions involves an assumption of an infinite ocean (or random phase) which is violated in Juan de Fuca Strait due to the phase locking of waves by reflection from a boundary. As an example consider an internal wave reflecting off of a flat bottom. It is clear that in the immediate vicinity of the bottom the potential energy must go to zero, whereas the horizontal kinetic energy need not be affected (ignoring friction). Thus the PE/HKE ratio would go to zero regardless of the intrinsic frequency of the internal wave. Similarly, an internal wave near a sidewall would have its horizontal motion constrained. This phase locking of the incident and reflected wave will create a modal structure, which communicates the presence of the boundary into the interior.

3.2.2 Consistency Relations in the Presence of Boundaries

I shall now consider how boundaries affect the two consistency relations of interest. Let us start with reflection from a horizontal, flat boundary (i.e. the bottom). The details of these calculations can be found in Appendix A. For a monochromatic wave, the sum of the incident and reflected waves satisfies

$$u = 2A_{inc} \tan\theta_{inc}[-\cos\phi_{inc} - if/\omega \sin\phi_{inc}]e^{i(kx+ly-\omega_i t)} \cos(m_{inc}z), \tag{35}$$

$$v = 2A_{inc} \tan\theta_{inc}[-\sin\phi_{inc} + if/\omega \cos\phi_{inc}]e^{i(kx+ly-\omega_i t)} \cos(m_{inc}z), \tag{36}$$

$$w = 2A_{inc} e^{i(kx+ly-\omega_i t)} \sin(m_{inc}z). \tag{37}$$

Here A_{inc} is the amplitude of the incident wave, θ_{inc} is the angle the incident wavevector makes in the horizontal plane, ϕ_{inc} is the angle the incident wavevector makes to the vertical and m_{inc} is the vertical wavenumber of the incident wave. Note that the flat bottom greatly simplifies this calculation since the reflected wave shares most of the incident wave's properties. The above form of (u, v, w) implies

$$\frac{PE}{HKE} = \frac{N^2}{\omega^2}\frac{ww^*}{uu^* + vv^*} = \frac{N^2(\omega_i^2 - f^2)}{(N^2 - \omega_i^2)(\omega_i^2 + f^2)}\tan^2(m_{inc}z). \tag{38}$$

This is the previously determined consistency relation, but now modified by a vertical structure function. It is easy to check that it imposes the required value of zero at the bottom ($z = 0$), but due to the phase locking the ratio will also go to zero at integer values of π/m_{inc}. Similarly the phase locking will create nodes where the horizontal velocities vanish, so that the ratio becomes infinite. In the ocean, one has a spectrum of vertical wavenumbers which will all be phase locked at the boundary. However, as one moves away from the boundary the phase of the waves, with different vertical wavenumbers, will lose coherence. Thus, one would expect to remove the zero and infinity cusps from the interior of the fluid. For a spectrum of waves, with the same intrinsic frequency but different vertical wavenumbers, this gives

$$\frac{PE}{HKE} = \frac{N^2(\omega_i^2 - f^2)}{(N^2 - \omega_i^2)(\omega_i^2 + f^2)}\frac{\int A_{inc}A_{inc}^* \sin^2(m_{inc}z)\, dm_{inc}}{\int A_{inc}A_{inc}^* \cos^2(m_{inc}z)\, dm_{inc}}, \tag{39}$$

where the integrals are over all relevant wavenumbers, and the amplitudes could be wavenumber dependent.

The z-dependence, called $F(z)$, for two different amplitude spectra ranging from white to m^{-2} is shown in figure 15. They both maintain the zero value at the

boundary ($F(0) = 0$), have a thin region of large oscillation and then asymptote toward a value of one ($F(z)_{z\to\infty} = 1$). The thin region of large oscillation away from the boundary is of O($2\pi/m_{max} = \lambda_{min}$) and is smaller for the red spectra than for the white one. Beyond a couple of the smallest vertical wavelengths from the boundary, the consistency relation asymptotes to within 10% of its value in an infinite ocean (at least for red spectra). In Juan de Fuca Strait, one might expect the smallest vertical wavelength to be roughly $10m$ (based upon some rough estimates with the velocity data), which implies that away from the top and bottom boundary layers the open ocean consistency relation is adequate.

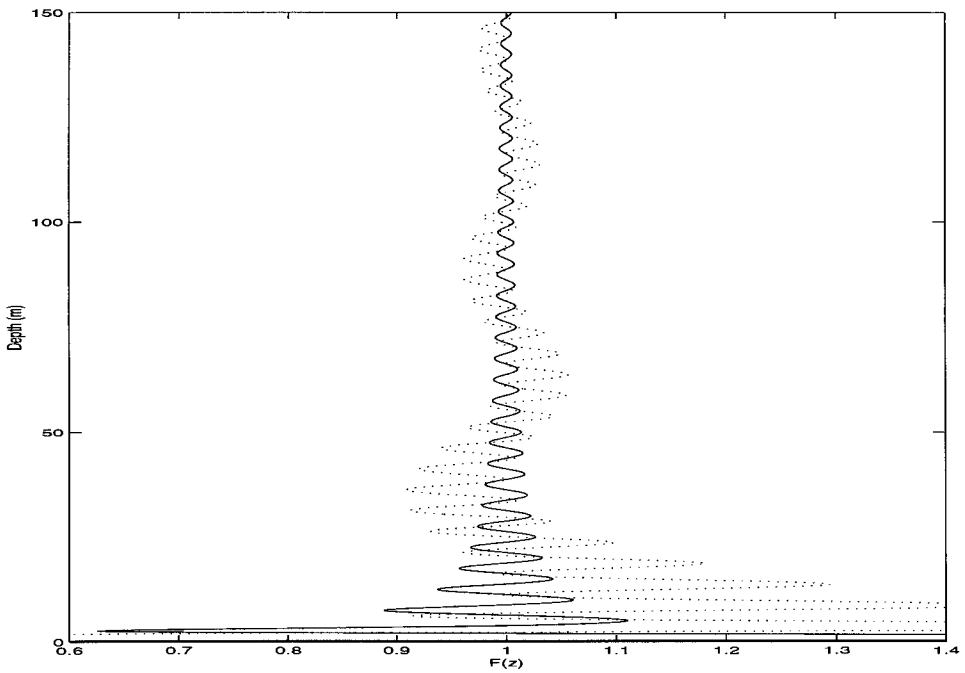

Figure 15: The vertical structure function calculated for two different vertical wavenumber spectra (white spectrum, dotted; m^{-2} spectrum, solid). Both spectra are bounded by the vertical wavelengths of 10 m and 103 m.

In a coastal environment a more reasonable approximation would be a sum

over modes, rather than an integral over wavenumber space. As the number of modes increases, the solution in the interior would asymptote towards the random phase solution. However, in shallow water, where the vertical structure may be dominated by only 2 or 3 modes, one would still expect significant deviations from the random phase limit.

It is easy to see from the velocity relations (equations 35 - 37) that the CCW/CW ratio is unaffected by a flat bottom, because the u and v equations share the same vertical dependence.

If the bottom is not flat, then the solution becomes much more complex because the amplitude and wavevectors of the incident and reflected waves are not as easily related. It is also true that the PE/HKE ratio does not equal zero at the bottom. The bottom slope permits a small vertical velocity, and hence a small isopycnal displacement. Furthermore, as the slope becomes more extreme the potential energy is less constrained, but now the horizontal kinetic energy is effected. If one considers a vertical side wall, one sees that the potential energy is unaffected, but the kinetic energy may be reduced since the flow is constrained to be parallel to the wall. Thus the horizontal kinetic energy at the wall would not necessarily go to zero, but would instead be dependent upon the angle of incidence, ϕ, of the internal waves. To be exact, the expected relationship for a wave incident upon a vertical side-wall at $y = 0$ is

$$\frac{PE}{HKE} = \frac{N^2}{\omega_i^2 + f^2}\frac{\omega_i^2 - f^2}{N^2 - \omega_i^2}\left[(\cos 2\phi + \frac{\sin^2\phi}{\cos^2 l_i y}) - \frac{f\omega}{(\omega^2 + f^2)}\sin 2\phi \tan l_i y\right]^{-1}, \tag{40}$$

where l_i is the incident wavenumber perpendicular to the side-wall (see Appendix

B for details). Note that at the wall ($y = 0$) this reduces to

$$\frac{PE}{HKE} = \frac{N^2(\omega_i^2 - f^2)}{(N^2 - \omega_i^2)(\omega_i^2 + f^2)} \sec^2 \phi. \tag{41}$$

This is expected since the wave motion is perpendicular to the wave vector. Thus a wave oriented directly into the wall is not constrained by the wall, whereas one oriented along it is completely blocked.

The CCW/CW ratio will be affected by a vertical sidewall, since the motion at $y = 0$ will be rectilinear and thus $CCW/CW = 1$ at the wall. In fact one can show (Appendix C) that for reflection from a wall at $y = 0$, the velocity takes the form

$$u+iv = i[(1-B)\sin(ly) - A\cos(ly)]\, e^{i\omega_i t} - i[(1+B)\sin(ly) + A\cos(ly)]\, e^{-i\omega_i t}, \tag{42}$$

where A and B are given by

$$A = \frac{(\omega_i^2 - f^2)kl}{\omega_i^2 k^2 + f^2 l^2}, \tag{43}$$

$$B = \frac{\omega_i f(k^2 + l^2)}{\omega_i^2 k^2 + f^2 l^2}. \tag{44}$$

Thus the ratio of counterclockwise to clockwise spectral kinetic energy is

$$\frac{CCW}{CW} = \frac{(1-B)^2 \sin^2(ly) - A(1-B)\sin(2ly) + A^2\cos^2(ly)}{(1+B)^2 \sin^2(ly) + A(1+B)\sin(2ly) + A^2\cos^2(ly)}. \tag{45}$$

This has the desired property of going to 1 at the wall, $y = 0$, and of returning the random phase solution when integrated over a spectrum of wavenumber, l.

3.2.3 Vorticity and Divergence

The previous consistency relations all relate velocity and displacement at a single point. There are however other distinguishing characteristics between internal waves and vortical modes. As the name suggests vortical modes can modify the underlying potential vorticity. The measurements do not allow an estimation of potential vorticity, but one can measure relative vorticity on the scale of the mooring separation. Although an eddy could clearly have relative vorticity on this scale it is important to realize that internal waves also have a relative vorticity signature.

If one chooses the x-axis to lie along the wavevector (noting that vorticity is independent of the reference frame) and choose a modal structure in the vertical for a uniform-N ocean, then one can write the vertical component of the relative vorticity, $\zeta = \frac{\partial v}{\partial x} - \frac{\partial u}{\partial y}$, as,

$$\zeta(x,z,t) = -\frac{if m_n}{\omega_i} \cot(m_n z)\, w(x,z,t), \tag{46}$$

$$= f m_n \cot(m_n z)\, \eta(x,z,t), \tag{47}$$

where $m_n = n\pi/H$ is the vertical wavenumber, and where

$$w(x,z,t) = w_0 \sin(m_n z)\, e^{i(kx-\omega_i t)}.$$

Equation 47 has an advantage over equation 46, in that the proportionality factor does not involve the intrinsic frequency, ω_i. This is preferable since the Doppler shifting of the observations by the tides makes a determination of ω_i difficult.

One can similarly obtain the divergence as,

$$\nabla \cdot U = -m_n \cot(m_n z)\, w(x, z, t). \tag{48}$$

3.2.4 Other Relations

One useful relation for internal waves is that the potential energy is directly related to the vertical kinetic energy, through

$$\frac{PE}{VKE} = \frac{N^2}{\omega_i^2}. \tag{49}$$

This allows us to write an internal wave consistency relation for VKE/HKE. There is a potential advantage in VKE/HKE since it only uses velocity data, which would be recorded by the same ADCP. In contrast, PE/HKE mixes data from the ADCP with a thermistor string mooring, which is not co-located. One could run into a problem, if there were strong gradients in the statistical properties of the waves between the ADCP and thermistor moorings. That said, the vertical kinetic energy relies on an accurate measurement of the vertical velocity. This is not necessarily an easy task with an ADCP.

3.3 Vortical Modes

Perhaps, the defining characteristic of a vortical mode is the modification of the potential vorticity field. It is also inherently sub-inertial. These two characteristics alone should make vortical modes easily distinguishable from internal waves. However, the first relies on an accurate measurement of potential vorticity, which requires that one have synchronous spatial and temporal measurements of velocity

and density. The moorings that measure velocity and density are not co-located, so we lack the ability to inter-relate the vortex stretching of the density field with the relative vorticity of the velocity field, on an instantaneous basis. This is important since an internal wave, while having no potential vorticity, does have both relative vorticity and vortex stretching, but they cancel each other. The sub-inertial character of the vortical mode is complicated by the strong tidal currents, which can Doppler shift the vortical modes into the inertial range of the spectrum, and similarly shift internal waves outside of their normal range (i.e. $f < \omega_i < N$). Although these characteristics still distinguish vortical modes from internal waves, we will not be able to apply them in a straightforward manner.

3.3.1 Ertel's Potential Vorticity

Ertel's potential vorticity is an important concept in physical oceanography [*Müller* 1995]. Notably, Ertel's potential vorticity is a globally conserved quantity, being modified only by irreversible processes, and is materially conserved for many oceanographic considerations. It thus acts as a governing equation for many important types of oceanographic motion. Ertel's potential vorticity is defined as

$$\Pi = (f + \nabla \times \mathbf{U}) \cdot \nabla(\mathbf{B} + \mathbf{b}), \tag{50}$$

where f is the Coriolis vector, $\mathbf{U}$ is the velocity vector and $B(z) + b(x, y, z, t) = -g\rho'/\rho$ is the buoyancy. Here the buoyancy has been subdivided into two parts such that $B(z)$ represents the horizontal and time average, and $b(x, y, z, t)$ is the remainder. Expanding the above equation and ignoring the horizontal gradients of

vertical velocity leads to

$$\Pi = fN^2 + fb_z + (v_x - u_y)N^2 + (v_x - u_y)b_z - b_x v_z + b_y u_z, \qquad (51)$$

where we use the fact that $B_z = N^2$, and where subscripts denote differentiation. Here the first term represents planetary vorticity, the second vortex stretching, the third relative vorticity, and the last three various nonlinear components [*Kunze and Sanford* 1993]. For oceanic measurements, it is common to linearize and just use potential vorticity,

$$PV = f + (v_x - u_y) - f\eta_z, \qquad (52)$$

where η is the vertical displacement of an isopycnal [e.g. *Müller et al.* 1988]. However, Kunze and Sanford [1993] point out that for closely spaced instruments the isopycnal tilting due to internal waves can cause the non-linear terms in (51) to become large, and thus make (52) a poor approximation.

Dividing (51) by the first term gives the following scalings,

$$\frac{\Pi}{fN^2} = 1 + \eta_z + R_\zeta + \eta_z R_\zeta + Fr^2. \qquad (53)$$

Here η_z is the strain, $R_\zeta = \zeta/f$ is the vorticity Rossby number and $Fr = (u_z^2 + v_z^2)/N^2$ is the Froude number and is formed by combining the last two terms [*Kunze and Sanford* 1993]. In our data set both the strain and vortical Rossby number can be order one, however the Froude number squared is generally two orders of magnitude smaller. It thus seems appropriate to neglect the last two terms in (51), but the others are potentially significant.

3.3.2 Thermal Wind

Geostrophic motions obey the thermal wind equations

$$fv_z = b_x = -\frac{g}{\rho_0}\rho'_x, \tag{54}$$

$$fu_z = -b_y = +\frac{g}{\rho_0}\rho'_y \tag{55}$$

(Note that the signs are correct, since there is a negative sign incorporated into the definition of $b(x, y, z, t)$). This implies the relation

$$\frac{f^2(u_z^2 + v_z^2)}{b_x^2 + b_y^2} = 1. \tag{56}$$

Fofonoff [1969] has shown for internal waves, under typical assumptions of random phase, that this ratio becomes

$$\begin{aligned} \frac{f^2(u_z^2 + v_z^2)}{b_x^2 + b_y^2} &= \frac{f^2 m^2}{N^2(k^2 + l^2)} \frac{HKE}{PE}, \\ &= \frac{f^2(N^2 - \omega_i^2)^2(\omega_i^2 + f^2)}{N^4(\omega_i^2 - f^2)^2}. \end{aligned} \tag{57}$$

This provides an additional consistency relationship for internal waves and geostrophic motions. The problem arises in the use of the thermal wind equations, which correspond to geostrophic flow (i.e. $R_\zeta \ll 1$). Much of the vortical mode structure in Juan de Fuca Strait may consist of eddies in cyclostrophic balance (i.e. $R_\zeta \approx O(1)$), which will not satisfy the thermal wind equations. Kunze and Sanford [1993] have also noted that the observed horizontal density gradients (or relative vorticity) will be dominated by motions at the array scale, whereas vertical shear (or vortex stretching) will be dominated by motions from the largest scale

near-inertial waves. Thus errors can arise if the array does not adequately capture these large scales. This is almost certainly the case in our observations where the array spacing is $\approx 1\ km$.

3.3.3 PE/HKE for the Vortical Mode

The consistency relations for the vortical modes differ from those for internal waves in that they are not expressed in terms of an intrinsic frequency. Instead, they are expressed in terms of a scaled aspect ratio, called the Burger number,

$$B = \frac{N^2 H^2}{f^2 L^2}, \tag{58}$$

(where H and L are height and length scales) and the vortical Rossby number,

$$R_\zeta = \frac{|\zeta|}{f}. \tag{59}$$

For purely geostrophic motions, the vortical Rossby number vanishes ($R_\zeta = 0$), so that the consistency relations reduce to equations in only one variable (the Burger number, B).

Kunze [1993] has shown that the potential to horizontal kinetic energy ratio for vortical modes is given by,

$$\frac{PE}{HKE} = \frac{(1 + R_\zeta/2)^2}{B}. \tag{60}$$

It is easy to see that for geostrophic motions this reduces to $PE/HKE = 1/B$, which is derivable from the thermal wind equations above. It is also worth noting that the above equation breaks down if $R_\zeta > N/f$, since then the shear is sufficient

to overcome the stratification, and one has fully three-dimensional turbulence.

I do not expect boundaries to have a direct impact on the vortical mode consistency relations. Lateral boundaries will, of course, constrain the location of the vortical mode, since an eddy cannot reflect back upon itself as in the same manner as an internal wave.

Although one cannot transform the vortical mode consistency relation into frequency space, one can put the internal wave consistency relations into Burger number space, through the dispersion relation. For internal waves one can write

$$\frac{PE}{HKE} = \frac{B\left(1+f^2/N^2\,B\right)}{2+\frac{N^2+f^2}{N^2}B} \approx \frac{B\left(1+f^2/N^2\,B\right)}{2+B}. \tag{61}$$

3.3.4 CCW/CW for the Vortical Mode

The ratio of counterclockwise to clockwise energy is easy for the vortical mode, since the velocity field is always locally rectilinear [*Kunze and Sanford*, 1993], and thus

$$\frac{CCW}{CW} = 1. \tag{62}$$

Again, one might expect that the rectilinear nature of the vortical mode is unaffected by boundaries. Recall that we are considering CCW and CW in the time domain at a fixed point, so that an eddy which is stationary may have CCW or CW vorticity, but the time series at a fixed location is constant, and therefore rectilinear.

The above relation is in contrast to an internal wave where the ratio must obey $0 \leq CCW/CW < 1$. As before one can write the internal wave relation in terms

of Burger number to get,

$$\frac{CCW}{CW} = \frac{(1 - f^2/N^2)\, B}{2 + (1 + f^2/N^2)\, B} \approx \frac{B}{2 + B}. \tag{63}$$

3.3.5 Divergence

Kunze and Sanford [1993] state that the divergence (∇) of a vortical mode is negligible if the twisting terms in the Ertel's potential vorticity equation are small. As mentioned above, these terms are small in our data set. Thus any divergence must be coming from the internal waves. *Fofonoff* [1969] shows that linear internal waves, under assumptions of random phase, satisfy $\nabla^2/\zeta^2 = \omega_i^2/f^2$. Also, since internal waves have more divergence then vorticity, if we observe that the vorticity is larger than the divergence in our data it implies the presence of vortical modes. Thus an array of moorings gives us additional constraints for the internal wave/vortical mode partitioning that are unavailable from a single mooring.

3.3.6 Linking Vorticity and Isopycnal Displacement

If one imagines a vorticity containing structure as a circular eddy in either geostrophic or cyclostrophic balance, then one can derive a simple scaling between the isopycnal displacement and the vorticity. We can characterize the eddy by a number of parameters: a half width, L, an isopycnal displacement at the center, η, an azimuthal velocity, U_{az}, and a water depth, H. From thermal wind, (55) or (54), one can write

$$\frac{fU_{az}}{H} = \frac{N^2\eta}{L}.$$

I can then write the vortical Rossby number as,

$$R_\zeta = \frac{\zeta}{f} = \frac{U_{az}}{fL} = \frac{N^2 \eta H}{f^2 L^2}. \tag{64}$$

To determine the length scale, we use the fact that the vortical mode is inherently sub-inertial, so that the intrinsic frequency is negligible compared to the Doppler shift frequency. Thus

$$\omega = \omega_i + U_d k \approx U_d k = \frac{\pi U_d}{L},$$

and consequently

$$R_\zeta = \frac{N^2 \eta H \omega^2}{\pi^2 f^2 U_d^2}. \tag{65}$$

If the eddy were in cyclostrophic balance then one would instead have

$$\frac{U_{az}^2}{L} = g' \frac{\partial \eta}{\partial y}, \tag{66}$$

which gives

$$R_\zeta = \frac{N\sqrt{\eta H}}{fL} = \frac{N\sqrt{\eta H}\omega}{\pi f U_d}. \tag{67}$$

3.4 Doppler Shift

The problem with moored instrument time series is that the measured frequency (ω) is Doppler shifted away from the intrinsic frequency (ω_i) by a factor proportional to the current speed (**U**) and the horizontal wavenumber, (**k**). Namely $\omega = \omega_i + \mathbf{U} \cdot \mathbf{k}$. In many circumstances the effect of the Doppler shift is negligible. For instance in the deep ocean a typical velocity is $0.02\, m/s$ and a wavenumber

is $2\pi/5000\,m$, which leads to a maximum $\mathbf{U}\cdot\mathbf{k}$ of $2.5\times10^{-5}\,s^{-1}$. This is equivalent to about 1 cycle every 100 hours, much less then most intrinsic frequencies of interest. However in Juan de Fuca Strait, we can easily have a velocity of $0.8\,m/s$ and a wavenumber of $2\pi/1000\,m$, which leads to a maximum $\mathbf{U}\cdot\mathbf{k}$ of $5.0\times10^{-3}\,s^{-1}$. This is equivalent to 1 cycle every 21 minutes, a value greater then the intrinsic frequency of many processes.

This Doppler shifting means that distinguishing between internal waves and vortical modes based on only a sub-inertial/supra-inertial split of the energy is impossible. One can no longer say that an observed high-frequency motion is an internal wave. It could instead be a vortical mode that is advected over the moor-ing. Similarly a sub-inertial motion could be an internal wave that is propagating against the current.

Furthermore, it is not true that there is only one wavenumber in the problem. The observations are really an integral over all waves and vortical modes. Finally, we lack any direct measurement of horizontal wavenumbers.

Although this problem seems insurmountable, I will work in reverse by taking some synthetic data sets and observing how Doppler shifting changes them. Thus, we shall attempt to built up a level of intuition that will enable us to talk about plausible, if not definite, scenarios.

3.4.1 Steady Advecting Flow

Consider first the simplest case of a monochromatic spectrum of waves in a constant current. We might take the vertical velocity to be described by

$$w(x,y,z,t) = w_0\cos(kx + ly + mz - \omega_i t),$$

where ω_i is the intrinsic, single frequency. Now consider that any other variable of interest (eg. u, v, ρ, η, P,etc.) can be written as

$$A(x,y,z,t) = F(\overline{k}, \omega_i, \rho_0, N, f, g) w_o \cos(kx + ly + mz - \omega_i t + \theta_0),$$

where $A(x,y,z,t)$ is any given variable, $F(...)$ is a predetermined function that can depend on anything except the space-time variables (x,y,z,t), and θ_0 is a fixed phase.

We assume that the water is moving relative to us with a velocity, $[U,V]$. Therefore our observed vertical velocity is

$$\begin{aligned} w(x-Ut, y-Vt, z, t) &= w_0 \cos(k(x-Ut) + l(y-Vt) + mz - \omega_i t), \\ &= w_0 \cos(kx + ly + mz - \omega t), \end{aligned}$$

where $\omega = \omega_i + Uk + Vl$ is the observed frequency. Similarly we can write

$$A(x-Ut, y-Vt, z, t) = F(...) w_o \cos(kx + ly + mz - \omega t + \theta_0).$$

We note that the Doppler shift from ω_i to ω occurs only within the sinusoidal term and not within the function F. Also the shift in observed frequency has not affected the observed phase difference. This implies for frequency spectra in a Doppler shifted frame of reference

$$S_A(\omega) = F^2(\omega_i\,,\,...)\, S_w(\omega).$$

Here $S_w(\omega)$ and $S_A(\omega)$ are the power spectra of w and A in the observed frequency

space. Thus, even in observed frequency space, the ratio of terms is determined by F, which depends on the intrinsic frequency. It is easy to see that this would generalize for the case of a constant current advecting a broad spectrum of frequencies.

To proceed further let us consider a specific case of interest, where

$$S_w(\omega) = \omega_i^2 \, S_\eta(\omega).$$

Now let us assume that we are ignorant of the magnitude of the Doppler shift and so we plot the two quantities $S_w(\omega)$ and $\omega^2 \, S_\eta(\omega)$. Now if

$$\omega^2 S_\eta(\omega) > S_w(\omega) = \omega_i^2 \, S_\eta(\omega),$$

then this implies that

$$\omega^2 = (\omega_i + Uk + Vl)^2 > \omega_i^2.$$

Assuming $\omega_i > 0$, this inequality is easily solved to give

$$Uk + Vl < -2\omega_i \;\text{ or }\; Uk + Vl > 0.$$

Similarly

$$\omega^2 S_\eta(\omega) < S_w(\omega),$$

implies $\omega^2 < \omega_i^2$ which gives $0 > Uk + Vl > -2\omega_i$.

Physically this result is easy to understand. If $Uk + Vl$ is positive then the waves are being advected past the observer in the same direction as they are prop-

agating, and hence appear at a higher frequency. If $Uk+Vl$ is negative but greater then $-\omega_i$ then the waves are being retarded by the flow and appear at a lower frequency. For $Uk + Vl = -\omega_i$ we would have lee waves. For $Uk + Vl < -\omega_i$ the waves are being pushed backwards and so their apparent frequency increases away from 0 as $Uk + Vl$ decreases, until at $Uk + Vl = -2\omega_i$ the waves are being pushed backwards at what appears to be their intrinsic frequency, although negative. Hence, one can use the observed spectral ratios to infer the value of the Doppler shift.

3.4.2 Time Varying Advecting Flow

Instead of a steady current let us now consider a time-varying current. If we take the current to have the form $[U_{max}\sin(\alpha t), V_{max}\sin(\alpha t + \phi)]$ then one can write the vertical velocity as seen by an observer as,

$$w(x - \int U dt,\ y - \int V dt, z, t) = w_0 \cos(kx + ly + mz - \omega t),$$

where

$$\omega = \omega_i + \frac{kU_{max}}{\alpha t}(1 - \cos(\alpha t)) + \frac{lV_{max}}{\alpha t}(\cos(\phi) - \cos(\alpha t + \phi)).$$

If the advecting flow is changing on time scales much slower then the internal waves ($\alpha \ll \omega_i$), then we can obtain a WKB type separation of variables. Then the solution would look like the sum of solutions for a number of constant current examples taken at successive phases of the advecting flow.

To examine this further, I have numerically modelled the observed frequency spectrum given various input spectra and advecting currents. Figure 16 shows the

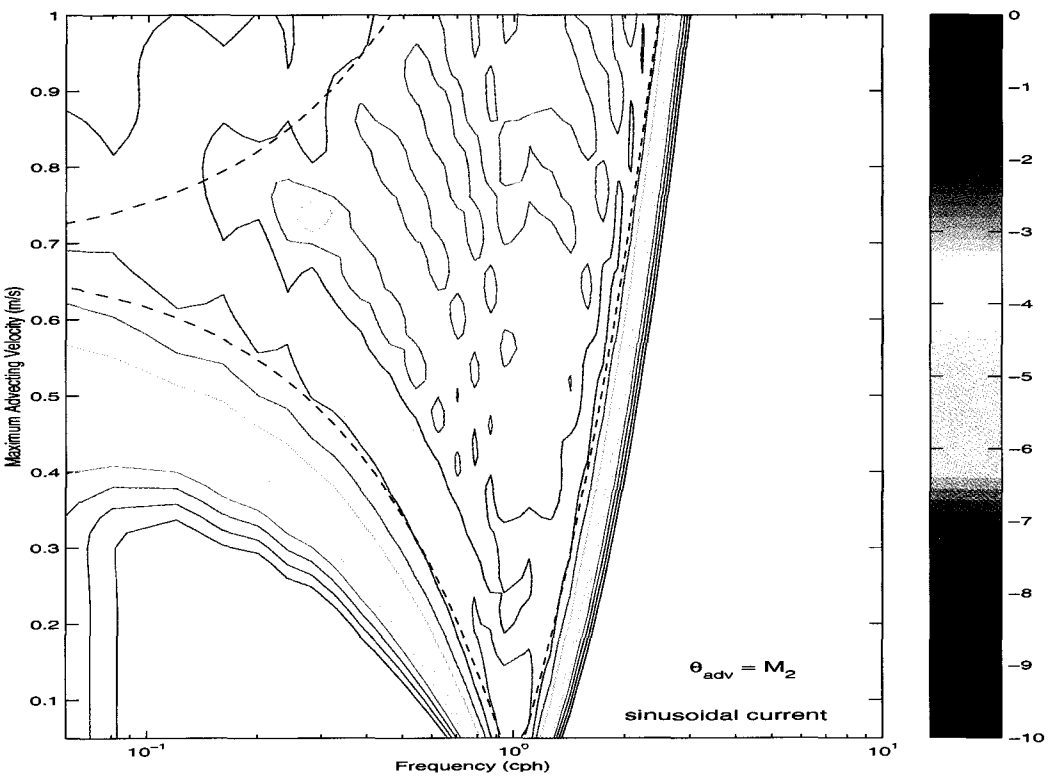

Figure 16: The logarithm of the observed spectra for a wave at 1 cph advected by a current at the M_2 frequency,as a function of the current strength. The dotted lines represent the curves $\omega_i \pm U_{max}k$.

spectrum versus ω as a function of the maximum barotropic velocity, for a sinusoidal advecting current at M_2 frequency, acting on an internal wave with intrinsic frequency $\omega_i = 1$ cph. I have estimated the horizontal wavenumber based upon a first mode assumption using a water depth of 120 m and an average buoyancy frequency of $N = 0.018\, s^{-1}$ (similar to our mooring locations, and corresponding to $c = 0.34$ m/s). The dashed curves in figure 16 represent $\omega_i \pm U_{max}k$, and so provide the theoretical limits over which the energy could be distributed. Note that the dashed curve in the upper left corner represents a reflection of the portion of the $\omega_i - U_{max}k$ curve that is less than zero. The sinusoidal current spends a greater proportion of time near its maximal values than near zero. Since there is a strong spectral gap between the Doppler shifting frequency and the intrinsic frequency of the internal wave, one expects that the observed spectra should resemble probability distribution functions (pdfs) of the advecting current. Generally this is the case with a strong ridge of energy just inside the two bounding curves, $\omega_i \pm U_{max}k$. Energy outside the bounding curves, and some of the structure inside is a function of the finite time series used in the calculation aliasing energy to different frequencies.

Since $\omega_{M_2} \ll \omega_i = 1$ cph, I do not expect that the resulting observed frequency spectra are dependent upon the actual choice of frequency for the advecting flow (as long as it is still sufficiently smaller than ω_i). To check this I can generate a new figure based upon the same internal wave, but now with the advecting frequency equal to that of K_1 instead of M_2. The plots are practically indistinguishable.

I can also vary the form of the advecting current from a sinusoidal to a sawtooth or a square wave. In these cases, one would still expect the advected energy to be constrained within the bounding curves, $\omega_i \pm U_{max}k$, but that its relative

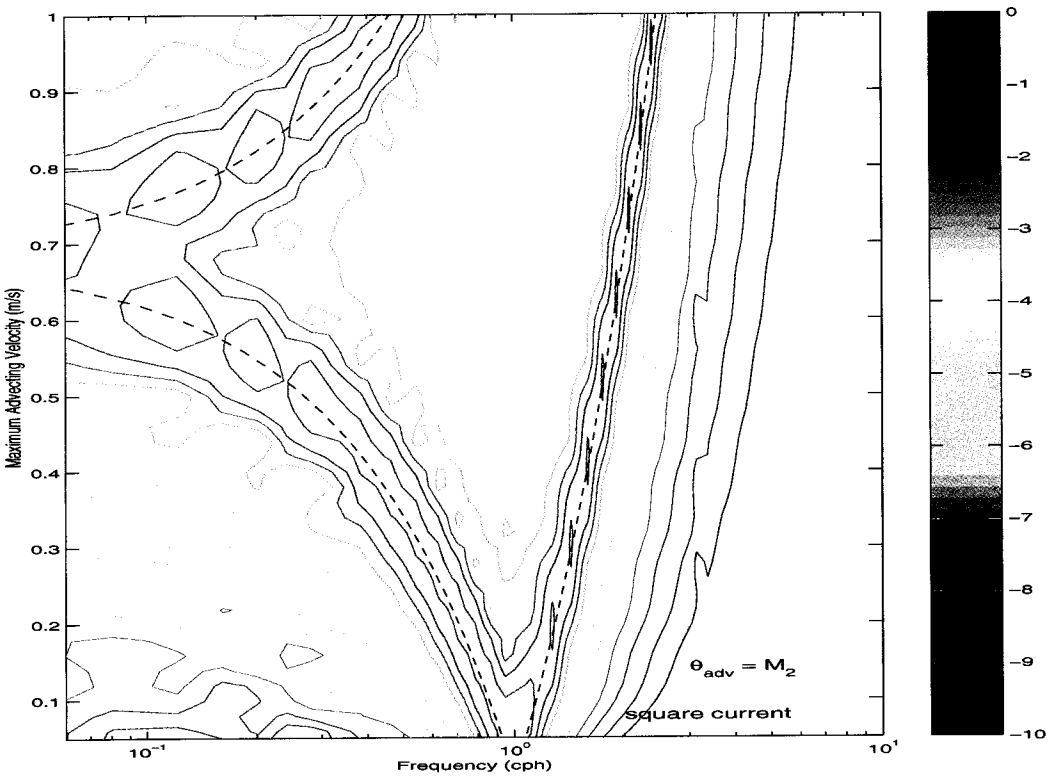

Figure 17: As in figure 16, but for a square wave current as opposed to a sinusoidal one.

distribution would change since the pdfs of the advecting currents are different. A sinusoidal wave is bimodal with peaks near, but slightly smaller than, $\pm U_{max}$, the sawtooth wave is equally probable at all velocities between $-U_{max}$ and U_{max}, and a square wave is strictly limited to the two extreme values. The square wave current at M_2 frequency advecting an internal wave at 1 cph is shown in figure 17. It behaves as expected with almost all the energy confined to the two curves, $\omega_i \pm U_{max}k$.

As one can see, a simple conceptual model produces good results for the case when the advecting frequency is considerably smaller then that of the advected wave. However in our data there is not a significant difference between the tides, doing the advection, and the background internal waves, being advected. Furthermore, there is more than just one frequency which characterizes both the the tides and the waves.

I will now look at how a sinusoidal current at the M_2 frequency would transform a spectrum of waves. Figure 18 shows the observed frequency spectra as a function of intrinsic frequency. The main features of the figure are still easily understandable, especially for frequencies which are considerable higher than the M_2 frequency, since they behave as described above. The energy outside the bounding curves, and some of the aliasing at high frequencies is a result of the chosen sampling period (1-2 minutes), which was matched to that of the ADCPs. For the lower frequency signal, that is similar to the frequency of the advecting tides, we see some indication of increasing energy in the double frequency band. This is expected since $\sin(At)\sin(Bt)$ is going to be expressible in terms of as $\cos((A-B)t)$ and $\cos((A+B)t)$.

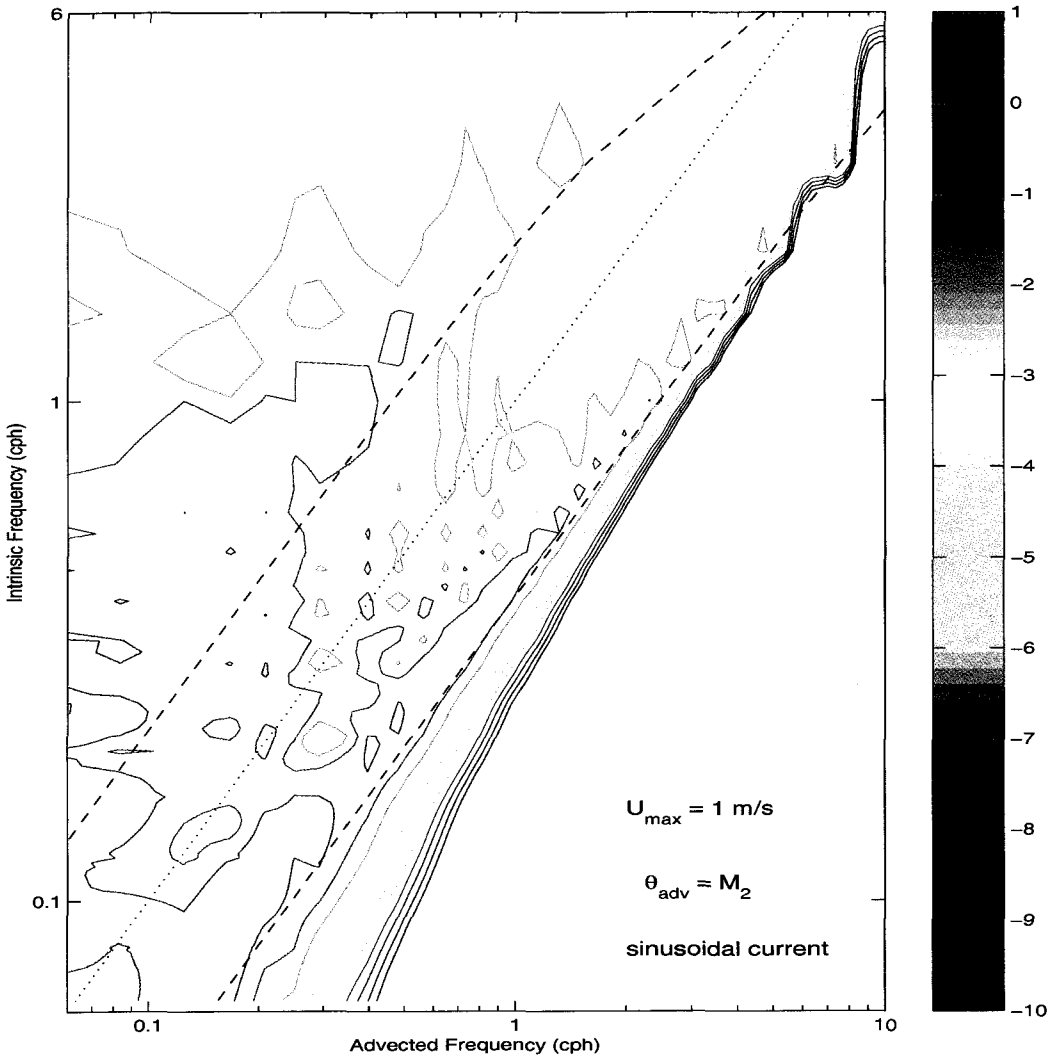

Figure 18: The logarithm of the observed frequency spectrum as a function of the intrinsic wave frequency, for waves Doppler shifted by a sinusoidal current at the M_2 frequency, and with a maximum current of 1.0 m/s. The dotted line represents $\omega = \omega_i$, the dashed lines are $\omega = \omega_i \pm U_{max}k$.

3.4.3 Using the Observed Tidal Currents

I can produce intrinsic-to-observed frequency maps for waves that are Doppler advected by the observed tidal currents (figure 19). Because a pdf of the tidal current is much more uniform then a simple sine wave, we see that the energy distribution, at a given intrinsic frequency, is close to a white spectrum. However there is still a peak, or pair of peaks, in the observed frequency spectrum that are not too far removed from the intrinsic frequency (dotted line in figure 19).

This matrix provides a means of generating the observed (advected) spectrum given an input intrinsic frequency spectrum. To get a better idea of how the Doppler shift distorts the kinetic energy spectrum, we shall take a well known spectrum representing internal waves (Garrett-Munk), and calculate the resulting observed spectrum after advection by the observed tidal currents. The result is shown in figure 20. The blue curve represents a Garrett-Munk spectrum for values of f and N that are representative of Juan de Fuca Strait. The red curves represent two possible advected spectrum. One for waves that are propagating eastward against the mean flow, and one for waves propagating westward with the mean flow. At high frequencies, we expect (and find) that the Doppler shift is insensitive to direction of propagation. However, at frequencies close to tidal, one might expect that there could be phase locking between the internal wave and the advecting current, which could cause strong directional assymetries. However, we see that the effect is almost non-existent. Similarly, the advected spectrum is relatively insensitive to the addition of a random phase. For comparison, the green curve represents a typical kinetic energy spectrum from our data.

The advected spectra are less steep than the original, as is the observed spectrum. This is expected, since the effect of the Doppler shift is to diffuse energy

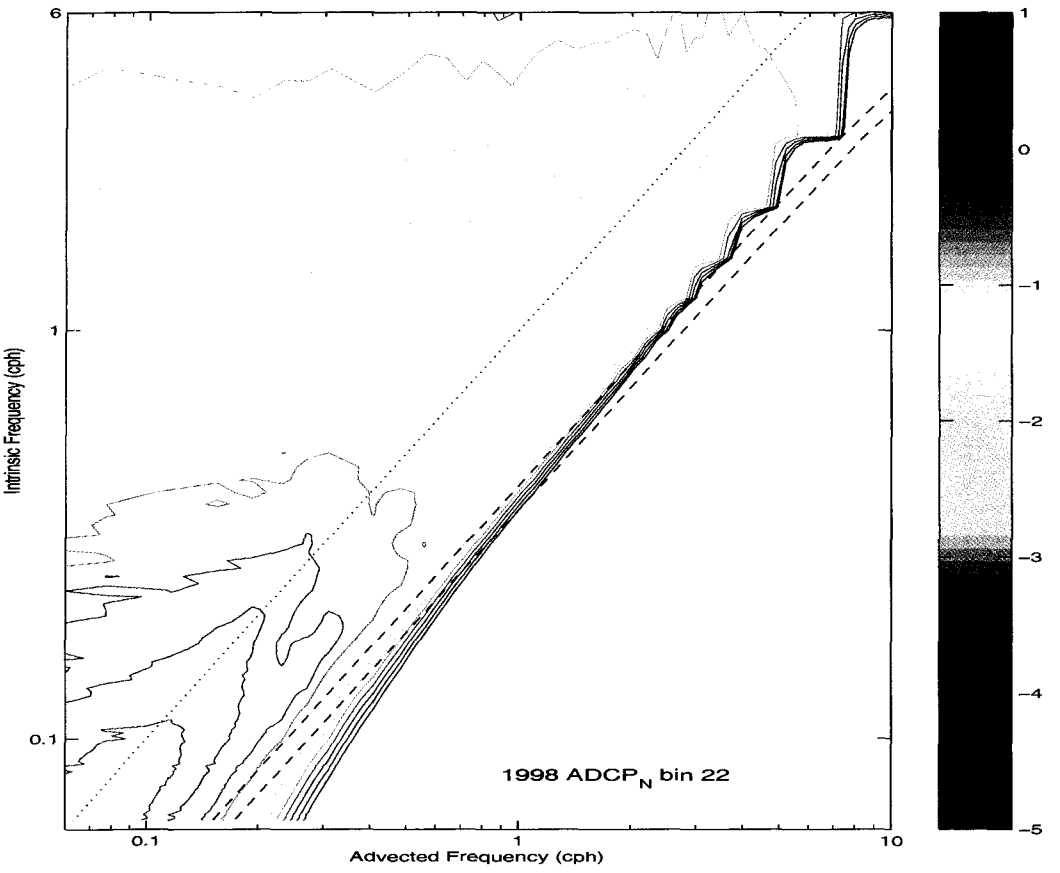

Figure 19: As in figure 18, but where the Doppler advecting flow is given by a representative tidal velocity in the data (the along-strait tidal velocity from mid-depth for the 1998 North ADCP).

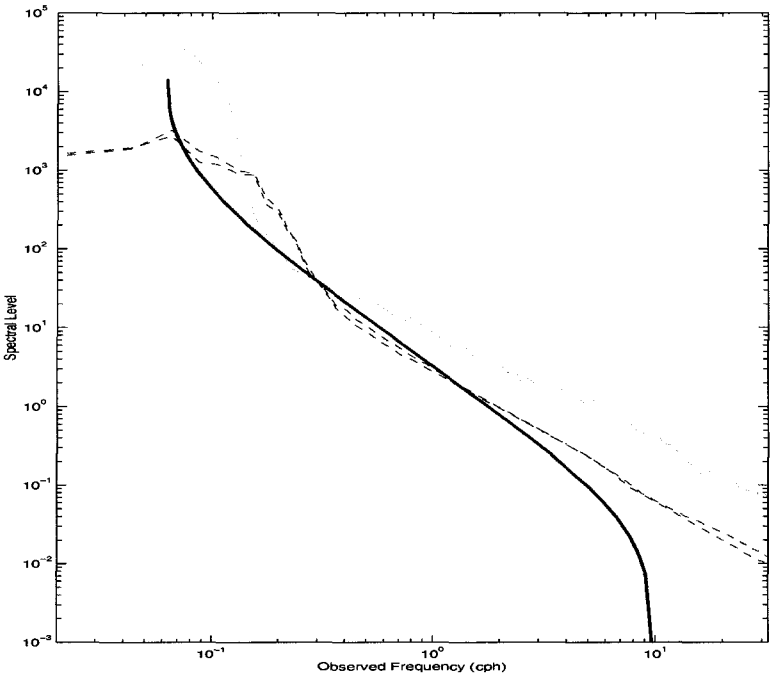

Figure 20: A Garrett-Munk spectrum (blue), the advected spectra for waves heading into and out of the mean current (dashed reds), and the observed de-tided spectrum (green). Doppler advecting tidal current and de-tided spectrum are from mid-depth at the 1998 North ADCP.

in the advected spectrum, and hence we expect a Doppler shifted spectrum to be whitened. The sharp inertial peak in the Garrett-Munk spectrum is broadened into a plateau that extends to approximately 0.2 cph. Despite these modifications, the Doppler shifted spectrum is still reasonably similar to the original.

Mathematically, we are able to invert the matrix that maps from intrinsic frequency to observed frequency. If one assumes that all the observed energy is due to internal waves (not vortical modes), and that the internal waves were all first mode, then we can multiply our observed frequency spectrum by the inverted matrix and obtain the intrinsic frequency spectrum. The first mode assumption is not unreasonable. The data show that about 65% of the energy is in the first mode. However, the kinetic energy spectrum could contain a large component due to the vortical mode. There is no reason why the vortical mode and the internal wave energy at the same observed frequency should be generated by processes with the same horizontal wavenumber. This would only be a reasonable assumption if $U \cdot k \gg \omega_i$, namely the observed frequency is dominated by the Doppler shift, not the inherent frequency.

Despite all these caveats, I did invert the matrix and generated a first guess intrinsic frequency spectrum. The problem is that the inversion of the matrix has no physical constraints on it, so that the inferred intrinsic frequency spectrum is unphysical (contains negative energy). A number of methods of smoothing the matrix and constraining the inversion were attempted, but none succeeded in producing a physically plausible result.

Therefore to proceed further, we will have to start from estimated (guessed) internal wave and vortical mode spectra and Doppler shift them. Then we can see if they are consistent with observations. An alternative approach, based upon

the similarity between the shifted and original Garrett-Munk spectra, is to ignore Doppler shifting to first order, and only invoke it as an explanation for discernible differences.

3.5 Summary

It will be helpful to have a simple summary of all the preceding pages. As a first point let us review the four primary consistency relations.

	CCW/CW	PE/HKE	Divergence/Vorticity
Internal Waves	$\frac{\omega_i^2-f^2}{\omega_i^2+f^2}$	$\frac{N^2(\omega_i^2-f^2)}{(N^2-\omega_i^2)(\omega_i^2+f^2)}$	$\frac{\omega_i^2}{f^2}$
Vortical Modes	1	$\frac{(1+R_\zeta/2)^2}{B}$	0

first relation (CCW/CW for the internal waves) is affected by side boundaries, but not top and bottom boundaries, and can be modified by the Doppler shift. The second relation (PE/HKE for internal waves) is affected by both side boundaries and top boundaries, and can also be affected by the Doppler shift. The third relation (CCW/CW for the vortical mode) is insensitive to all other factors. Finally the last relation (PE/HKE for the vortical mode) is affected by Doppler shift, but in a helpful manner since it provides a means of relating Burger number to observed frequency.

We shall also use the relation $PE/VKE = N^2/\omega_i^2$, which is true for internal waves. This relation is unaffected by boundaries, but can be affected by the Doppler shift. It is not true for the vortical mode. For instance, an eddy may have potential energy associated with the doming of isopycnals, but this energy is not converted into vertical velocity.

4 Observations

d programs were run in Juan de Fuca Strait during the summers of 1997-1999. They consisted of the deployment of temperature chains and bottom-mounted, upward looking acoustic Doppler current profilers (ADCPs) for periods of 1-2 months, timed to coincide with the peak freshet from the Fraser River. Concurrent to the mooring work, general hydrographic measurements were conducted. Table 2 gives a summary of the primary instruments used in this thesis. Moorings that were relatively close to each other, in a given year, are grouped together in the table. The positions of the moorings in table 2 are plotted in figure 21.

In addition to these moored instruments, general hydrography was performed with a variety of CTDs. The CTD measurements consisted of two principal transects: one across the strait near Jordan River (C-Line), and one running the length of the strait in the middle on the international border (A-Line). In addition, survey work, including 24 hour time series, was conducted near the mooring locations.

4.1 Acoustic Doppler Current Profilers

ADCPs use the Doppler shift between a transmitted and returned acoustic signal to determine the velocity of the backscatterer, projected along the axis of the sound beam. The time that it takes for the sound to return is translated into a distance along the beam using an estimate of the speed of sound in water. Thus each transducer measures the velocity toward or away from it along a beam perpendicular to the plane of the transducer head. Although early Doppler velocimeters used a simple frequency shift between the transmitted and received pulses to determine the velocity of the reflecting water, this is no longer the method employed. In-

Table 2: A list of the moorings used in this thesis.

	Depth (m)	Deployment Length (d)	Depth Resolution (m)	Time Resolution (s)	Offshore Distance (km)
97 ADCP	122	31	2	45	1.9
97 T-Chain N	99	30	5 - 10	10 - 180	1.5
97 T-Chain E	101	30	5 - 10	10 - 180	1.4
97 T-Chain S	128	30	5 - 10	10 - 180	2.6
98 ADCP North	135	28	2	40	5.5
98 T-Chain East	145	28	5 - 10	10 - 180	5.5
98 T-Chain West	138	28	5 - 10	10 - 180	5.5
98 ADCP South	101	28	2	60	0.6
98 T-Chain South	110	28	5 - 10	10 - 180	0.7
99 ADCP South	112	52	1	120	1.8
99 ADCP East	100	31	2	120	1.0
99ADCP North	77	49	1	60	0.35
99 T-Chain South	129	49	5 - 10	20 - 300	2.5
99 T-Chain North	102	49	5 - 10	20 - 300	1.0
99 T-Chain East	122	49	5 - 10	20 - 300	1.7

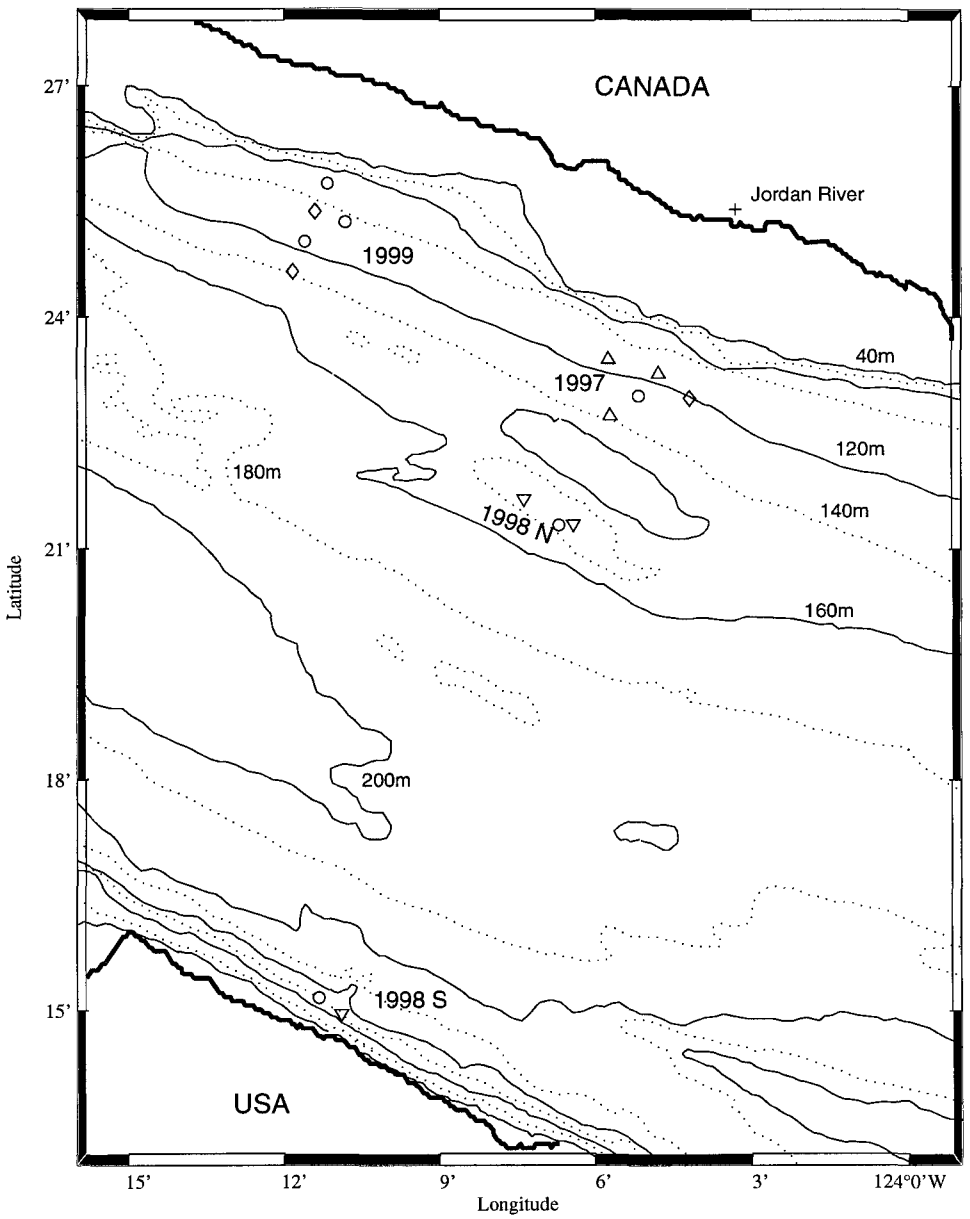

Figure 21: The location of moorings used in this thesis. Groups of moorings are labelled with the relevant year. Symbols represent ADCPs (circles), 1997 T-Chains (upward triangles), 1998 T-chains (downward triangles) and 1999 T-Chains (diamonds). Contours represent the bathymetry in intervals of 20m from 40m to 200m depth.

stead, the instrument emits two closely timed pings, each of which has been phase coded so that they can be distinguished upon return. Now instead of comparing the frequency shift between the emitted and received pulses, the instrument measures the phase shift between the first and second pulses. The idea is that the first pulse will encounter a scatterer and reflect; the scatterer will then move a small amount before the second pulse hits it and returns. This small distance that the scatterer moved is translated into a phase difference between the first and second pulses. Along with the known time separation between the pulses, at emission and return, this translates into a scatterer, and therefore water, velocity estimate.

The bottom-mounted ADCPs used in these observations are all 300 kHz broadband Workhorse models from RD Instruments. All except one of the ADCPs, (1999 ADCP E), had Janus configured transducer heads. The Janus configuration consists of four transducer heads aligned with the four axes, $[+x, +y, -x, -y]$, and oriented at 20° from the vertical. The other ADCP (1999 East) had a specially designed head with one transducer pointing directly upward, while the other three were spaced at 120° intervals around the circumference and were again oriented at 20° from the vertical. Together the four heads on the ADCP sample the water in a cone which starts at the instrument and proceeds away from it with a spreading angle of 40°. The velocities that are measured in this way are referred to as being in beam coordinates.

For ease of use it is often desirable to transform from beam coordinates into a standard x, y and z reference frame. To do this we need to combine velocities from one beam with velocities from the other beams. However, this assumes that the water being measured on one side of the instrument is moving in exactly the same way as water on the other side of the instrument. This is a good approximation

near the instrument itself, but as the beams travel away from the instrument they diverge at an angle of 40°. As an example, two opposite facing beams at $100m$ above the instrument are separated by $73m$ in the horizontal. Phenomena with wavelengths much larger than this spacing are measured accurately, whereas the signal from smaller processes is spatially aliased.

Although there is no method to alleviate this problem we do at least get an estimate of its magnitude. We use the four beam velocities, at a given distance, to solve for three velocity components, (u, v, w). Because there is a level of redundancy in our calculations, we can measure the best fit u, v and w, and then calculate the deviation of individual beam velocities from this best fit. The maximum value of this discrepancy will be called our error velocity. If the instrument is aligned exactly with the vertical than this calculation is simple. Two opposite facing beams measure u and w, which can be combined to give an estimate of the vertical velocity, say w_u. Similarly, the two beams at right angles to our first pair measure v and w, and lead us to an estimate w_v. We would then say that our best guess for the vertical velocity is $w = (w_u + w_v)/2$ and our error is $e = 1/2(w_u - w_v)$. Finally, the (u, v, w) velocity triad is then rotated into an (East, North, w) velocity which is termed the Earth coordinate frame.

Aside from the aliasing in space that happens during the beam-to-Earth coordinate transformation, there is averaging in time that happens as well. It is impractical to store every ping, and hence every velocity profile, that is generated by the ADCP. Therefore, it is necessary to perform some form of ensemble average over multiple pings. This ensemble averaging can be helpful since for physical processes that are stationary over the length of the ensemble we get a better measure of velocity. In our observations we programmed the ADCP to col-

lect in burst mode. This means that the ADCP would collect a fixed number of successive pings, as closely spaced as possible, for a short period of time, O($15s$). The ADCP would then store the average value of these pings and wait quietly until the next sampling time before collecting another burst of samples.

There are several other factors which influence our data set. First, the transducer head that generates the sound pulse takes a finite time to stop vibrating. The return signal from water immediately in front of the transducer occurs within a time period during which the head is still ringing. We are therefore unable to measure the velocity profile closer than $2m$ from the instrument.

Second, the sound beam produced by the transducer has some spread to it, $\approx 1°$, and also has some energy in side lobes. In the case of a bottom-mounted ADCP, we might envisage a side lobe that is closer to the vertical than the main transducer beam. A signal from the side lobe beam could leave the instrument, reflect off of the sea surface and return to the transducer in the same length of time as a reflection from some backscatter along the main beam, but at a level below the sea surface. Hence, the side lobes limit the accuracy of the velocities measured close to a reflecting boundary, such as the sea surface for our upward looking instruments. It is therefore customary to ignore backscatter returns which arrive after the time it would take for a side lobe beam to leave the instrument, reflect off of the sea surface, and return to the instrument. The amount of the water column that this eliminates depends on the beam spread angle. In our case of a 20° beam angle, we loose the top 6% of the water column.

Another possible concern when analyzing ADCP data involves the nature of the backscatterer. If the backscatter comes from small, suspended particulate one might believe that it accurately measures the velocity of the water contain-

ing the particles. There might be a problem if the backscatter comes from zoo-plankton, since they are capable of self-propulsion. The speed of a zoo-plankton, O(1 cm/s), is insignificant with respect to our observed horizontal velocities, but could bias the observed vertical velocities. However, analysis by *Ott* [2000] leads us to believe that the vertical velocities measured are accurate.

4.2 Temperature Chain Instrumentation

The temperature chains were equipped with a variable number of internal recording temperature sensors from Richard Brancker Industries. Although the vast majority of the sensors recorded only temperature, five also recorded pressure (T/P sensors) and four also recorded conductivity (T/C sensors). Each chain was outfitted with two S4 current meters near the top and bottom as well.

The temperature sensor on all the pods was external to the instrument, and had a reasonably fast response time of $\approx 1s$. The stated accuracy of the temperature sensors was $\pm 0.05°C$ with a resolution of $0.002°C$. The temperature pods were pre- and post-calibrated to within this temperature accuracy. The majority of these temperature-only pods had an extended memory package which allowed for the storage of 256,000 records. This translates into one measurement every 10s for a month-long deployment. Interspersed with these were several older instruments that had only one quarter of the above memory capacity. The internal clocks in the temperature cells were all pre-synchronized. The manufacturer stated that the clock drift was less than 2 seconds/day, however post-deployment checks revealed that the drift was often much larger, O(10 seconds/day). The individual time series from each instrument were corrected under the assumption that the drift was linear throughout the deployment.

The temperature-pressure instruments had the same temperature cell, but also contained an additional pressure sensor. The pressure sensor was accurate to ≈ 0.15 psi with a resolution of ≈ 0.05 psi, which translates into a depth accuracy of about 0.1 m. The pressure sensors were primarily used to measure mooring motion, which could be calculated and corrected for after recovery. These instruments lacked the internal memory of the dedicated temperature pods, and were therefore confined to recording once every $3 - 5$ minutes, depending on the deployment length.

The temperature conductivity cells had the same temperature package as all the other instruments, but also measured conductivity. The conductivity sensor had a resolution of $25\,\mu S/cm$ and an accuracy of $75\,\mu S/cm$. This translates into a salinity resolution of $\approx 0.004\,psu$ and an accuracy of $\approx 0.012\,psu$. The conductivity cells were pre- and post-calibrated for salinity as well as temperature. The conductivity sensors had the same limited memory capacity as the T/P pods above.

The S4 current meters were only used for the evaluation of mooring motion, although they do contain additional sensors. The measured velocity had a resolution to $0.002\,m/s$ with a full scale range of $3.50\,m/s$. The standard accuracy is taken to be 2% of the reading $\pm\, 0.01\,m/s$.

4.3 Conductivity Temperature Depth Instruments (CTDs)

The CTD measurements provide a number of advantages over the moored temperature chains. They allow us to map out spatial variability through transects and thus allow us to estimate large-scale mean density gradients. They also provide better depth resolution than can be obtained by the temperature chains. This

depth resolution allows the calculation of Thorpe scales and therefore gives an estimate of vertical mixing [*Stansfield et al.*, 2001]. Most importantly for our purposes is that they measure both temperature and salinity and thus allow us to determine the T-S relationship near our mooring. Together with the four moored temperature-conductivity sensors, we can construct an estimate of the evolution of the T-S relation near our mooring over the entire deployment. This gives us the ability to map our temperature observations to density, with certain predictable uncertainties.

Three types of CTDs were employed, and their sampling accuracies are listed in Table 3. All the CTDs were pre- and post-cruise calibrated to within the listed precisions.

	App. Microsystems Ltd. STD 12+	Sea-Bird 911+	Sea-Bird Seacat 19
Sampling Rate (s^{-1})	15	24	2
Δz (m)	0.05	0.07	0.03
ΔT ($^{\circ}C$)	0.01	0.002	0.01
ΔC ($S\,m^{-1}$)	0.003	0.0004	0.001
$\Delta \rho$ ($kg\,m^{-3}$)	0.038	0.006	0.022

Table 3: The accuracies of the three types of CTD used in the observations [*Stansfield et al.* 2001].

The CTD work always included several repetitions of the across strait (C-Line) and along strait (A-line) transects (Figure 22). In addition, across strait transects were occasionally performed at the ridge south of Victoria, near Race Rocks, and at the entrance to Juan de Fuca Strait, near Cape Flattery.

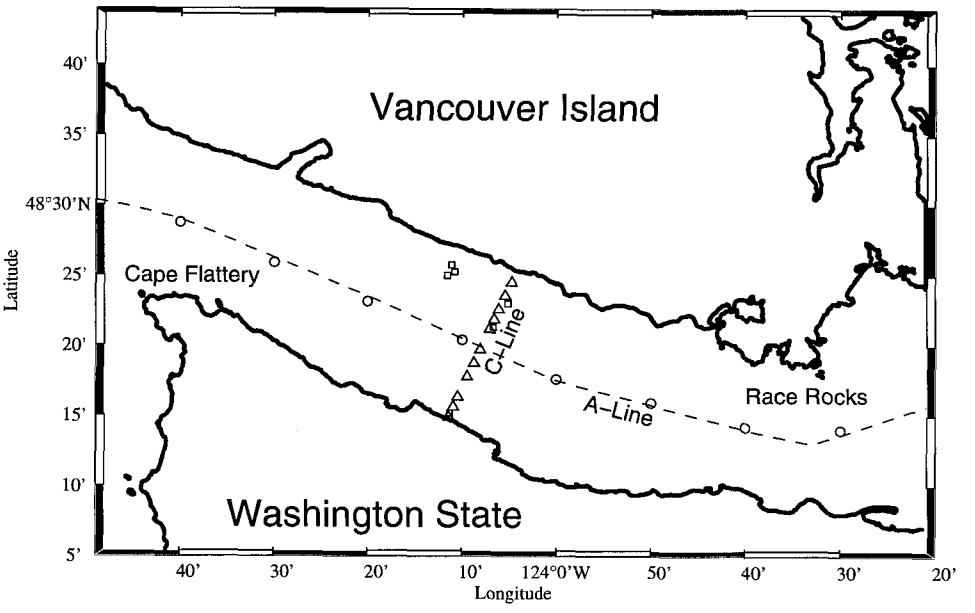

Figure 22: The A-Line (circles) and C-Line (triangles) CTD transects. For reference the locations of ADCP moorings for 1997 through 1999 are shown as squares (refer to figure 21).

4.4 Mooring Design

Although the moorings were located in different locations and water depths over the three years of the observations, the basic design of the moorings did not change significantly. We shall therefore present two generic moorings. Any exceptions to this basic form will be noted.

4.4.1 Bottom-Mounted ADCP Mooring

This mooring consisted of two parts connected by a long ground line. The ADCP itself was housed in an aluminum pyramid with the transducers pointing up out of the apex. Attached to this by a polypropylene ground line was a set of buoys linked to an anchor by an acoustic release (Figure 23). The need for an entirely subsurface mooring was dictated by the heavy ship traffic in Juan de Fuca Strait, and the design of the ADCP bracket was intended to make it trawl-resistant. The aluminum ADCP bracket was $\approx 1.5m$ on a side and the transducer heads were $\approx 1.2m$ above the bottom. The Workhorse ADCP was fitted into a gimble system which allowed it to point vertically upward even though the bracket itself was located on a slope. Bolted to the bottom of the Workhorse was an additional battery pack which was itself wrapped in lead sheeting. This additional weight was used to increase the moment arm of the ADCP with respect to the gimble, in order to ensure that the ADCP was closely aligned with the vertical.

4.4.2 Taut-Wire Temperature Chain Mooring

The temperature chain mooring was a simple taut-wire mooring, with an anchor on the bottom and a float located $\approx 15m$ below the surface (Figure 24). The temperature pods were fitted into individual plastic brackets which were bolted

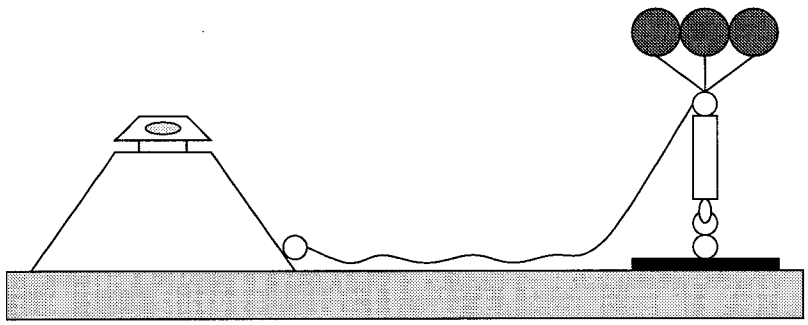

Figure 23: Cartoon of the bottom-mounted ADCP mooring configuration

onto the steel wire at pre-selected locations. In addition two S4 current meters were located in-line at the top, just below the float, and the bottom, just above the acoustic release. The subsurface float used in 1998 and 1999 had a special aerodynamic design in order to reduce drag. The float was very effective in the strong tidal currents, with a vertical excursion of only $3m$ at peak velocity (surface tide has been removed by subtracting the pressure record from the sensor at the bottom of the temperature chain). In comparison, the 1997 mooring in similar conditions with a standard 36 inch round float had vertical excursions of almost $30m$. We will discuss the correction for this mooring motion later [section 5.2].

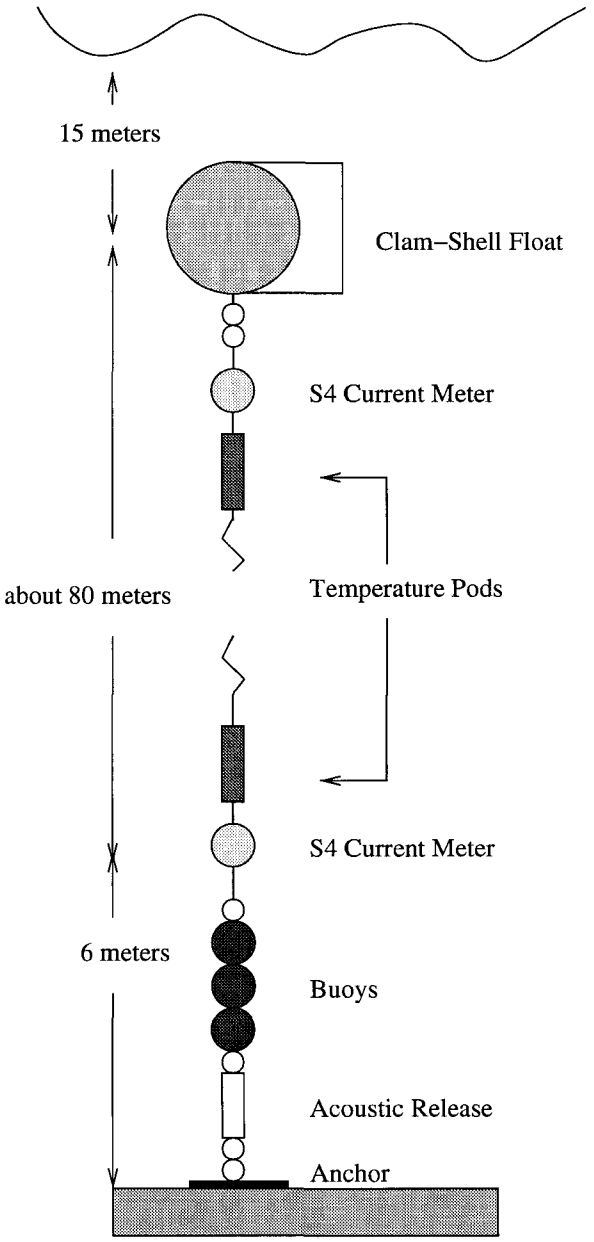

Figure 24: Cartoon of the temperature chain mooring

5 Data Analysis

The raw data recorded by the moored instruments provides a particular view of the physical environment surrounding the instruments. This view may be quite detailed, but it is often spatially selective, contaminated with noise, and may contain gaps. In order to obtain a data set that is useful for comparison with theory it is often necessary to reanalyze the data, transform it to a common spatial and temporal grid, and mark or selectively fill regions of poor data quality. Furthermore, certain quantities of interest, such as vorticity and Reynolds stresses, are not measured directly but require some analysis of the data. This section details both the initial data quality and discusses any fixes applied, and explains the methods used to create more complex data products.

5.1 ADCP Data

The RDI acoustic Doppler current profilers that were used to collect our observations are extremely good, reliable instruments which have performed as expected in the field. The only problems with data quality have been due to the environment itself not the instrument. For example, parts of the water column may at times be very low in scatterers, so that the returned signal is weak. In this case the ADCP records no signal at that location and time so that we have a gap in the data, but this data gap is not due to any failing in the instrument. The only other problems with interpreting ADCP data are known *a priori*, and are primarily concerned with assumptions about water homogeneity near the instrument, which is necessary to compare signals from different beams.

The acoustic Doppler current profiler records the velocity, backscatter inten-

sity and percent good (a measure of the number of returned pings above a minimum intensity threshold) for each of the four beams, as a function of distance along the beam. It also records the heading, pitch, roll, and temperature at the instrument.

5.1.1 Raw Data Products

Figure 25 shows both a beam velocity, from beam 3, and the associated backscatter intensity. Beam 3 was pointed roughly West in this deployment, so the velocity signal is dominated by the barotropic semi-diurnal tide, but there are also high frequency signals apparent on top of the tides. The strong line undulating across the top of the figure is caused by sound reflecting off the ocean surface. It is not truly indicative of the water depth since this reflection comes from a side-lobe of the main sound beam (for this deployment the water depth was 112 m). The undulation in the pseudo-surface is due to the tidal change in water depth.

The backscatter signal is strongest near the instrument and is reduced in strength further away. Away from the strong reflections near the instrument, which are generally indicative of the bottom boundary layer, there are a number of non-random streaks and clouds of increased backscatter. The most noticeable such structure consists of a downward arc, between julian day 209.2 and 209.35, and an upward arc, between 209.75 and 209.9. Between these two arcs the upper water column has relatively low backscatter. This signal is the result of the daily migration of zoo-plankton [*Thomson and Allen*, 2000]. The zoo-plankton feed in the upper water column, but during the daylight hours they migrate to depth to avoid predation.

The majority of the data are 100% good, meaning that all the pulses that went into that ensemble returned a sufficiently strong signal over the water column.

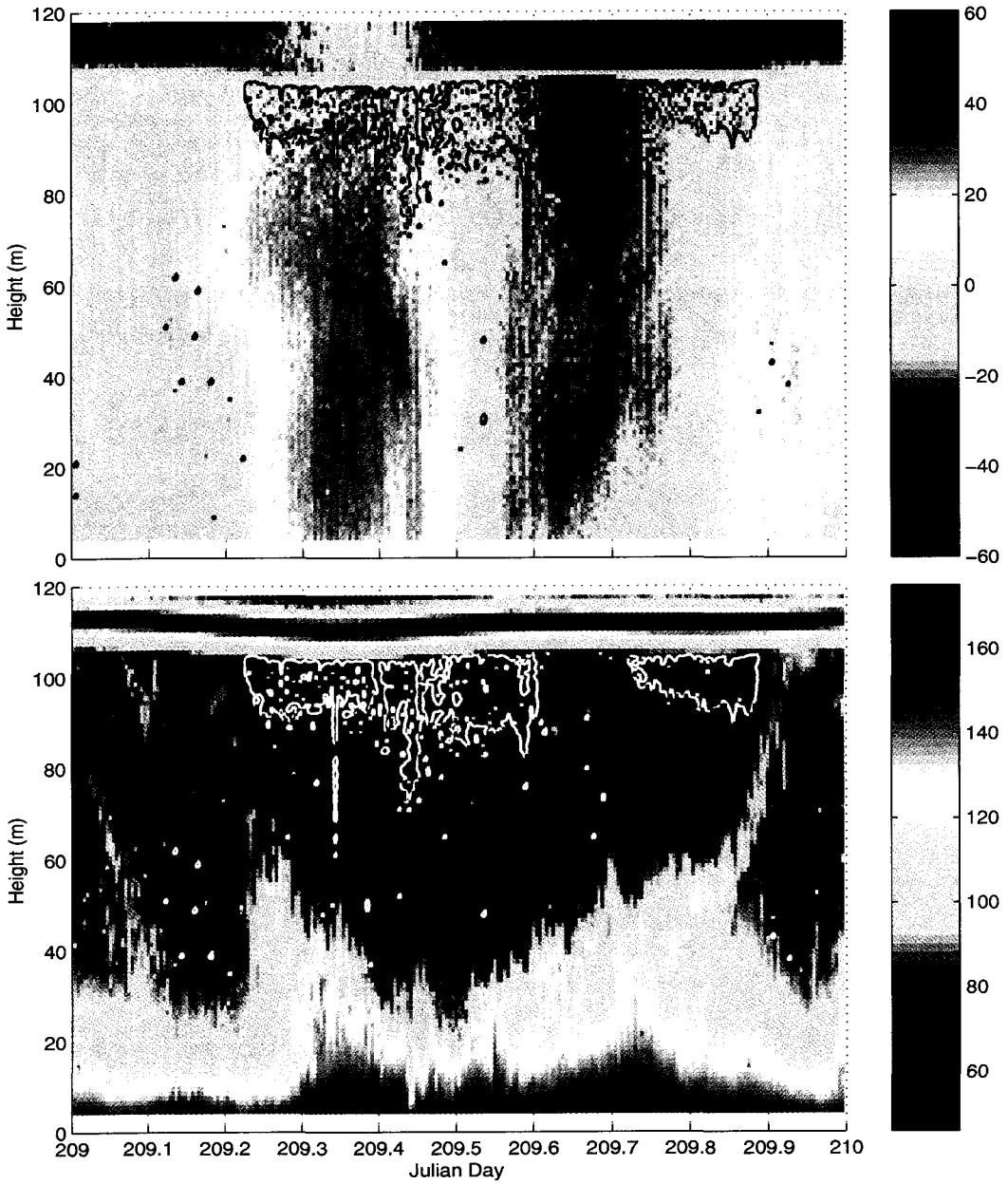

Figure 25: One day of velocity (top, in cm/s) and backscatter (bottom, in counts) from beam 3 of the 1999 ADCP South mooring. Also outlined is the 90% good contour.

The figure shows the 90% good contour. Through most of the lower water column the signal is perfect with only a few random instances where the return is less than optimal. However, there are two large regions of consistently poor return in the upper water column during the day. We show only the 90% good contour, since the majority of data are 100% good and where the data are less then 100% they quickly deteriorate, so that there is little difference between the 90% good contour and the 30% good contour. In general, the velocity signal returned from regions of low percent good is suspect. Note the high amount of variation in the recorded velocity signal in the low percent good region between 209.7 and 209.9. These regions of low percent good in the upper water column are also regions of low backscatter (lower panel) and are likely due to the absence of scatterers [*Ott*, 2000]. Note that the percent good signal returns to acceptable levels during the ebb, between 209.6 and 209.75, perhaps due to the increased particulate material in the outflow.

The loss of data from one of the beams, due to low percent good, does not necessarily result in a data gap in the processed Earth coordinates. There is a level of redundancy in the beam-to-Earth transformation, since four beam velocities map onto only three Earth velocities. The calculation can, lacking four beams, transform the three remaining beam velocities directly into the three Earth velocities. Therefore signals must be lost from at least two of the beams before a gap is introduced in the Earth velocity data. This prevents many of the "random noise" gaps in the beam velocities from being mapped into the Earth velocities. However the low percent good signal from the upper water column during the day is present in all four beams and results in a velocity that is unreliable in this region.

Figure 26 shows the heading, roll and pitch for the 1999 ADCP South moor-

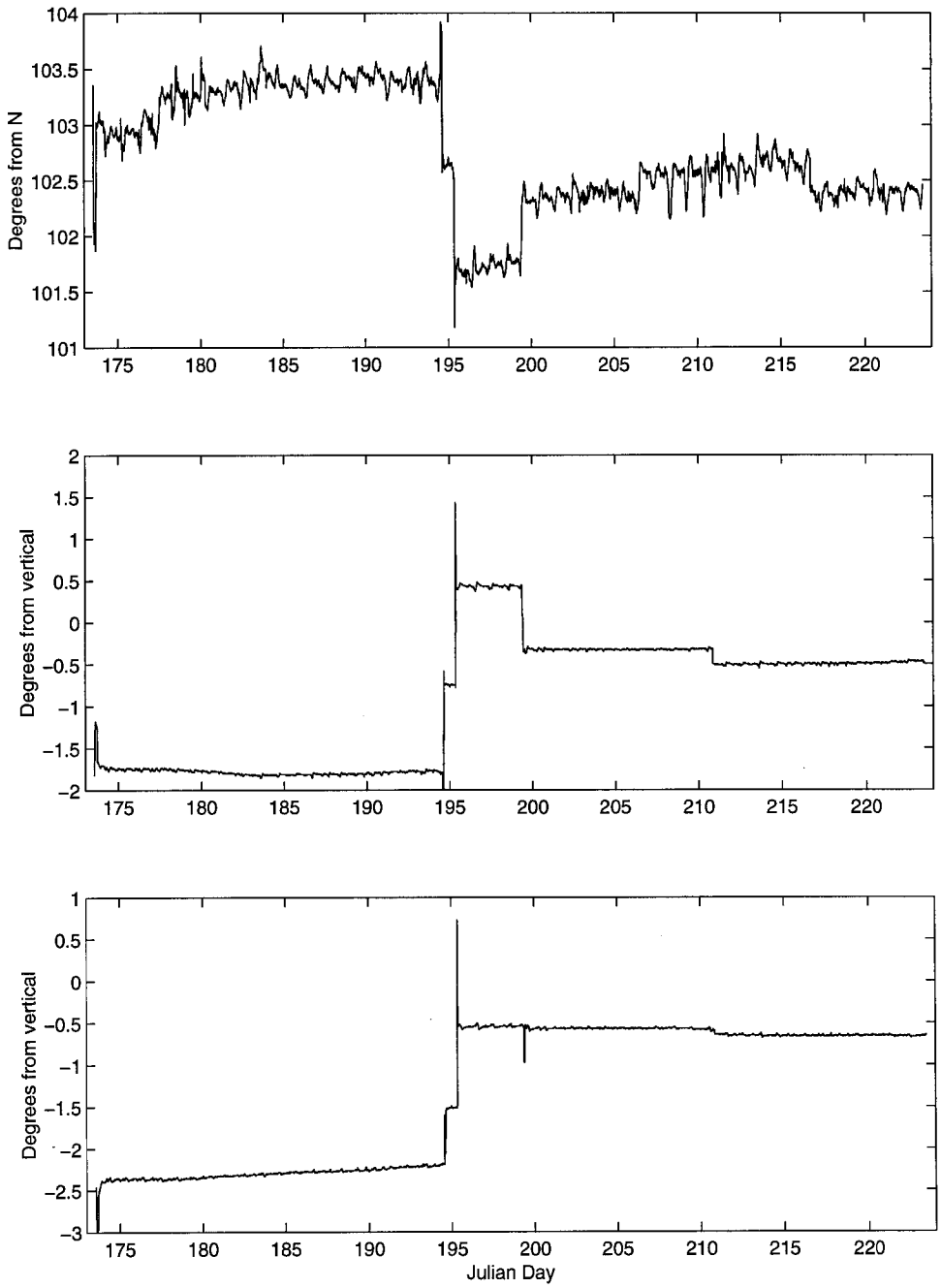

Figure 26: The heading (a), pitch (b) and roll (c) from the 1999 ADCP South mooring.

ing. The readings are generally constant with a weak tidal signal, broken by several dramatic shifts. The shifts are synchronous across all three sensors and are thought to be due to the bracket shifting and settling in the soft sand of the bottom. The dramatic shifts are really fairly slow changes over a period of about one hour, and are thought to be due to the moored bracket slipping into a tidally scoured depression, followed by a relaxation as the gimbles attempt to rectify the motion. The slight upward linear trend in the heading, of order $0.02°/\text{day}$, is likely due to the battery pack draining and changing its magnetic field.

5.1.2 The Transformation to Earth Coordinates

The ADCPs were programmed to record in beam coordinates, and then the data are transformed after recovery into the more useful Earth coordinate (ie. East, North, and vertical). The reasons for this are four-fold. Firstly, the internal conversion from beam to Earth coordinates supplied by RDI is non-optimal in its bin mapping, although the errors are usually small [Ott, 2000]. Secondly, the conversion from beam to Earth coordinates is non-reversible due to the bin-mapping. The third reason concerns a loss of data when recording in Earth coordinates. In beam coordinates the ADCP records the four beam velocities as well as a percent good for each beam. In Earth coordinates the ADCP compares the percent good to a preset tolerance and masks the values less than this tolerance with NaNs. Although this is what will be done to the beam coordinates eventually, doing it post-deployment allows us some latitude in picking the percent good tolerance. If we chose Earth coordinates we are stuck with whatever tolerance we preprogrammed into the instrument. Lastly, the high-frequency component of the signal, that is above the buoyancy frequency, is unlikely to be spatially coherent over the spread

of the beams and so the beam coordinates retain the statistical variability of this signal which is smoothed by the transformation to Earth coordinates.

The beam coordinates are first transformed to a set of coordinates that are fixed relative to the instrument and labelled instrument coordinates (under assumptions of spatial homogeneity). To understand this transform consider that we can relate beam and instrument coordinates by the following matrix,

$$\mathbf{B} = \begin{pmatrix} b_1 \\ b_2 \\ b_3 \\ b_4 \end{pmatrix} = \begin{pmatrix} \sin\alpha_1 \sin\gamma_1 & \sin\alpha_1 \cos\gamma_1 & \cos\alpha_1 \\ \sin\alpha_2 \sin\gamma_2 & \sin\alpha_2 \cos\gamma_2 & \cos\alpha_2 \\ \sin\alpha_3 \sin\gamma_3 & \sin\alpha_3 \cos\gamma_3 & \cos\alpha_3 \\ \sin\alpha_4 \sin\gamma_4 & \sin\alpha_4 \cos\gamma_4 & \cos\alpha_4 \end{pmatrix} \begin{pmatrix} u_{instr} \\ v_{instr} \\ w_{instr} \end{pmatrix} = \mathbf{MU_{instr}} \tag{68}$$

where b_i is the ith beam velocity, α_i is the elevation angle of beam i, γ_i is the azimuthal angle of beam i and $(u, v, w)_{instr}$ is an (x, y, z) orthogonal set of velocities whose orientation is fixed relative to the instrument. It should be noted that this transform really shows what the expected beam velocities would be for a given set of Cartesian velocities, under assumptions of no lateral gradients. This transform can take account of the fact that the transducers are not perfectly aligned with the ideal specifications. As an example, one of our instruments has actual azimuths that are located at 271.44°, 91.43°, 358.57° and 178.56° as opposed to the ideal angles of 270°, 90°, 360° and 180°. We note that opposite transducers are very closely to being 180° apart but that the two pairs themselves are aligned at $\approx$ 87° as opposed to 90°. Additionally the elevations are not perfectly aligned at $-70°$ (the instrument is always assumed to be pointing downwards), but rather at $-69.77°$, $-69.48°$, $-69.65°$ and $-70.08°$. These angles will change between different instruments and are measured by the manufacturer.

The matrix $\mathbf{M}$ is not invertible in its current form since we are mapping the three instrument velocities into four beam velocities. What we need to do is introduce a fourth instrument velocity, e_{instr}, which is called the error velocity. This means that a fourth column is now added to the matrix $\mathbf{M}$. We shall choose this fourth column such that it is orthogonal to the first three columns of $\mathbf{M}$. Having done this we can find the inverse of the matrix $\mathbf{M}$ and then we have

$$\begin{pmatrix} u_{instr} \\ v_{instr} \\ w_{instr} \\ e_{instr} \end{pmatrix} = \mathbf{M^{-1}} \begin{pmatrix} b_1 \\ b_2 \\ b_3 \\ b_4 \end{pmatrix}. \tag{69}$$

This gives us a set of velocities that are in a regular orthogonal frame but are not yet in the desired Earth coordinates. To transform into the Earth coordinates we need to account for heading, pitch and roll. This is a simple set of rotations and can be expressed as

$$\begin{pmatrix} u \\ v \\ w \end{pmatrix} = \begin{pmatrix} \cos H & \sin H & 0 \\ -\sin H & \cos H & 0 \\ 0 & 0 & 1 \end{pmatrix} \begin{pmatrix} 1 & 0 & 0 \\ 0 & \cos P & -\sin P \\ 0 & \sin P & \cos P \end{pmatrix} \begin{pmatrix} \cos R & 0 & \sin R \\ 0 & 1 & 0 \\ -\sin R & 0 & \cos R \end{pmatrix} \begin{pmatrix} u_{instr} \\ v_{instr} \\ w_{instr} \end{pmatrix}, \tag{70}$$

where (u, v, w) are the East, North and vertical velocities, H is the heading, P is the pitch and R is the roll. However, the measured pitch and roll need to be adjusted before use in the above equations. Firstly for upward looking ADCPs the desired roll is actually the measured roll plus $180°$. Furthermore, the reported pitch is not really pitch since it is fixed within the roll sensor and hence contami-

nated by the roll. The corrected pitch is given by

$$P = \arcsin\left(\frac{\sin p \cos r}{\sqrt{1 - \sin^2 p \sin^2 r}}\right), \tag{71}$$

where p and r are the pitch and roll recorded by the ADCP [*Ott,* 2000].

The resulting Earth velocities from this calculation are shown in figure 27, for the same day and mooring as used above in figure 25. We note that both the East-West (u), and the North-South (v) velocities are dominated by the tidal signal, although the magnitude of the East-West velocity is greater since the tide is constrained to flow principally along the axis of Juan de Fuca Strait. The vertical velocity has little signature of the tide, probably because the bottom slope at this mooring is quite small. Instead there appear to be numerous high-frequency events.

In converting to Earth velocity, we have used all the available data regardless of the percent good. Therefore the velocity in the upper water column during the day, where the returned signal was weak, is quite erratic. The horizontal velocities of the tide are, arguably, reproduced but most of the high frequency signal appears to be lost in the noise. In particular the vertical velocity in most of this region is unreliable.

5.1.3 Pitch, Roll and the Vertical Velocity

It is clearly important to accurately measure the orientation of the instrument so that the vertical velocity can be distinguished from the horizontal velocity. Since the horizontal velocity, u and v, is of at least one and often two orders of magnitude larger than the vertical velocity, w, a slight error in orientation could severely

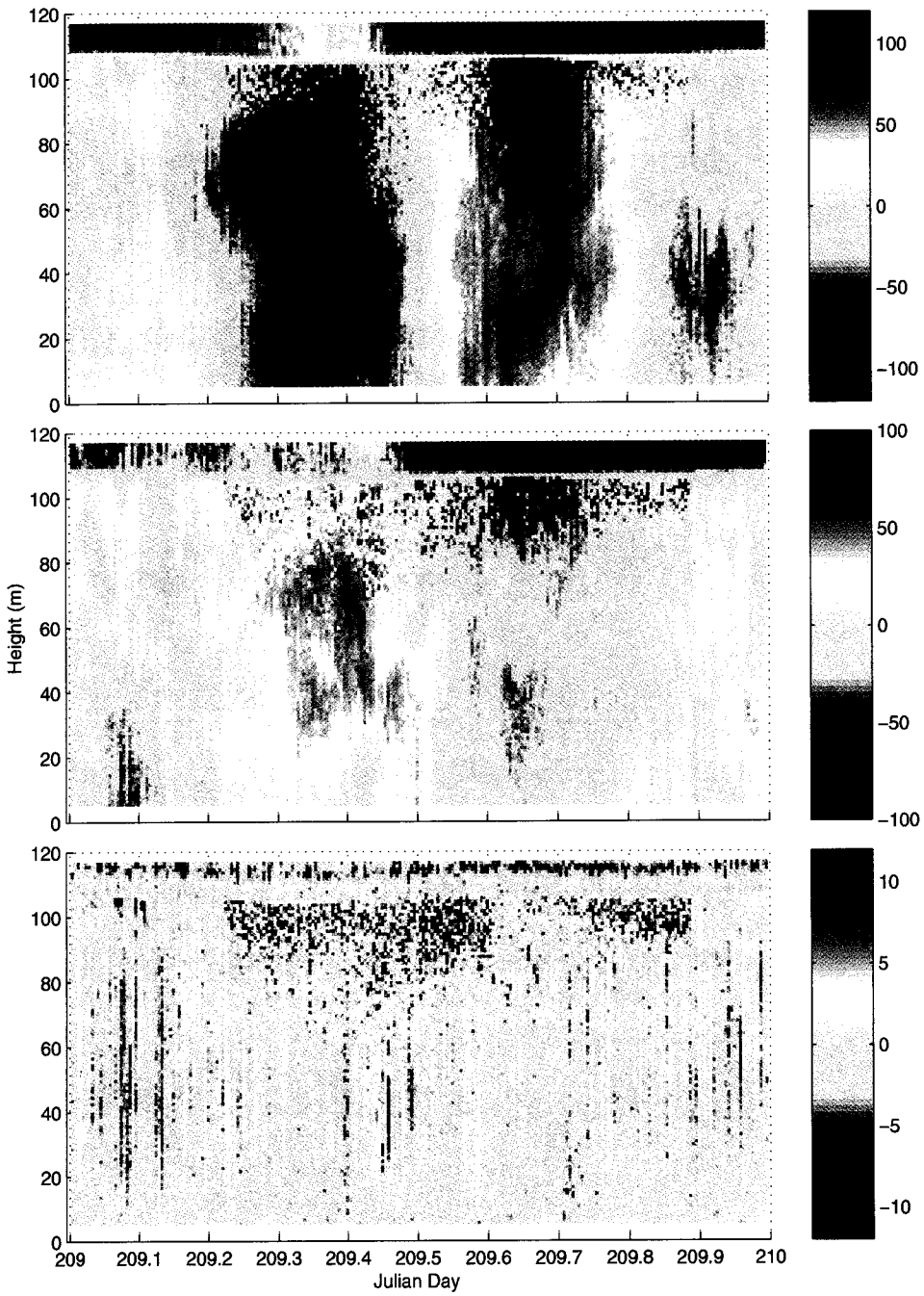

Figure 27: The East (top), North (middle) and vertical (bottom) velocity from the 1999 ADCP South mooring (in cm/s).

contaminate w. Conversely, the horizontal velocities are relatively insensitive to the pitch and roll, since u with a small component of w is still reasonably close to u. The potential problem is that the pitch and roll sensors on the ADCPs are not extremely accurate. Although, the sensors record to a precision of $0.1°$ they are in fact only accurate to $1.0°$.

Let us consider the worst case scenario where the instrument claims to be perfectly vertical but is actually inclined at $1.0°$ in pitch and roll. Then we would observe

$$\begin{aligned} w_{obs} &= w\cos(1°)\cos(1°) + u\sin(1°)\cos(1°) + v\cos(1°)\sin(1°) \\ &= 0.9997w + 0.0174(u+v). \end{aligned}$$

Therefore, the worst case would see the vertical velocity contaminated with 1.7% of the horizontal velocity. This would be completely unacceptable since the contamination from u and v would overwhelm w, at least for motions whose axis was predominantly horizontal and whose inherent frequency is significantly less than the buoyancy frequency. Furthermore, since $\sin\theta\cos\theta$ is linear in θ for small θ, the contamination of w with u and v varies linearly with the assumed error in θ.

Ott [2000] performed detailed analysis on the vertical velocity recorded by an ADCP, located roughly at the position of our 1998 North ADCP mooring. His findings indicated that the vertical velocity signal is generally much more reliable than the above maximum error would indicate. However, the usefulness of the vertical velocity is highly variable between different moorings.

5.1.4 Tidal Analysis

The tides play an important role in the dynamics of Juan de Fuca Strait. They represent both a large component of the observed velocity and act as a forcing for other motions, such as internal waves and eddies. We therefore would like to identify the tidal motion within the total velocity field and thus be able to separate the total velocity into tidal and residual components. Luckily the tides are well-behaved, regular phenomena with known frequencies for the different astronomical components. We therefore seek to separate the tides by fitting sinusoids with known tidal frequencies to the data. We employ a standard tidal analysis package [*Foreman* 1976] to perform this decomposition. The resulting output provides major and minor axis amplitudes plus inclinations and phases for all the resolved components.

The number of resolvable tidal constituents depends upon the length of the record. The Rayleigh criterion states that only constituents that are separated by at least a complete period over the length of the record are distinguishable. In practice, with modern accurate instrumentation this criterion can be eased so that constituents that are separated by only a fraction of a period are differentiated in the analysis. We have chosen a Rayleigh criterion of 0.8 for our analysis, although we gain little by lowering from the theoretical value of 1.0. This is because the length of our time series allows for the direct resolution of most of the more energetic tidal constituents. There are two pairs of astronomical constituents that are not capable of being distinguished in a time series of the given length. These are the diurnal components P1 and K1 and the semi-diurnal components S2 and K2. The analysis package infers the value of the smaller components (P1 and K2) from the larger ones (K1 and S2). The ratio and phase of the smaller to larger

components is based upon previous long-term tidal records from the surrounding waters.

Depending on the length of the time series at a given mooring, the analysis package identifies between 32 and 38 tidal constituents plus a mean. Table 4 presents a selection of the results from the analysis of bin 60, approximately mid-depth, of the 1999 ADCP South mooring. Although this table represents only one depth bin at a single mooring the results are not radically different at other depths and moorings, except for the phases. We note that the M2 constituent is the single largest and typically accounts for about 25% of the total tidal energy, with K1 the second largest containing about 18% of the tidal energy, and O1 third with about 11%. Together these three components account for more than half of the total tidal energy. The majority of the tidal current components have major axes oriented at about 160°, measured counterclockwise from East. This aligns them with principal axis of Juan de Fuca Strait, indicating that the major axes are oriented predominantly along isobaths.

Note that the discrepancy in inclination of the low-frequency components (MM and MSF) and the principal astronomical components is unexplained and only apparent in this mooring. In the analysis of other moorings the low-frequency tidal components are more closely aligned with the isobaths. This could be due to the fact that the spring-neap cycle has two influences on our data, which are slightly out of phase with one another. The first factor is the purely astronomical and affects the currents. The second is due to the modulation of mixing within the Gulf Islands, which causes the freshwater forcing at the eastern end of Juan de Fuca Strait to change on a fortnightly cycle [*Griffin and LeBlond* 1990]. Although the mixing within the Gulf Islands is in phase with the astronomical signal

the propagation of that mixed water out to sea will lag the astronomical signal.

Tidal Constituent	Period (h)	Major Axis (cm/s)	Minor Axis (cm/s)	Inclination (degrees)	Phase (degrees)
MM	661.31	4.151	0.652	141.7	0.2
MSF	354.37	4.445	1.705	134.9	45.7
O1	25.82	22.143	-2.089	160.6	264.3
P1	24.06	11.270	-0.719	162.0	286.1
K1	23.94	34.056	-2.173	162.0	286.1
N2	12.66	9.283	0.039	160.6	250.9
M2	12.42	43.938	1.705	157.8	283.9
S2	12.00	11.426	-0.618	153.7	303.8
K2	11.97	3.110	-0.168	153.7	303.8
MK3	8.18	2.739	-0.260	70.8	285.4
M4	6.21	2.885	-1.567	42.9	275.6
MS4	6.10	1.801	-0.889	53.3	268.7
2MK5	4.93	2.477	-1.036	22.8	54.3

Table 4: A selection of the results from the tidal analysis of the velocity for bin 60 of the 1999 ADCP South mooring.

The diurnal tidal components and the semi-diurnal components are about equally energetic with $41 \pm 4\%$ in each frequency band. The fortnightly component (MSF) and monthly component (MM) each account for $\approx 2\%$ of the energy, with the remainder ($\approx 11\%$) in the higher frequency components.

Figure 28 shows the East velocity (u) from bin 60, approximately mid-depth, for the 1999 ADCP South mooring. The top panel shows the velocity record for the entire two month deployment. We note that the velocity is dominated by the tidal signal, which is of a mixed diurnal/semi-diurnal nature and hence exhibits strong spring-neap variation. The lower panel shows two days of data with the results of the tidal analysis superimposed. We clearly see that the tides are responsible for the vast majority of the kinetic energy, and also that the tidal

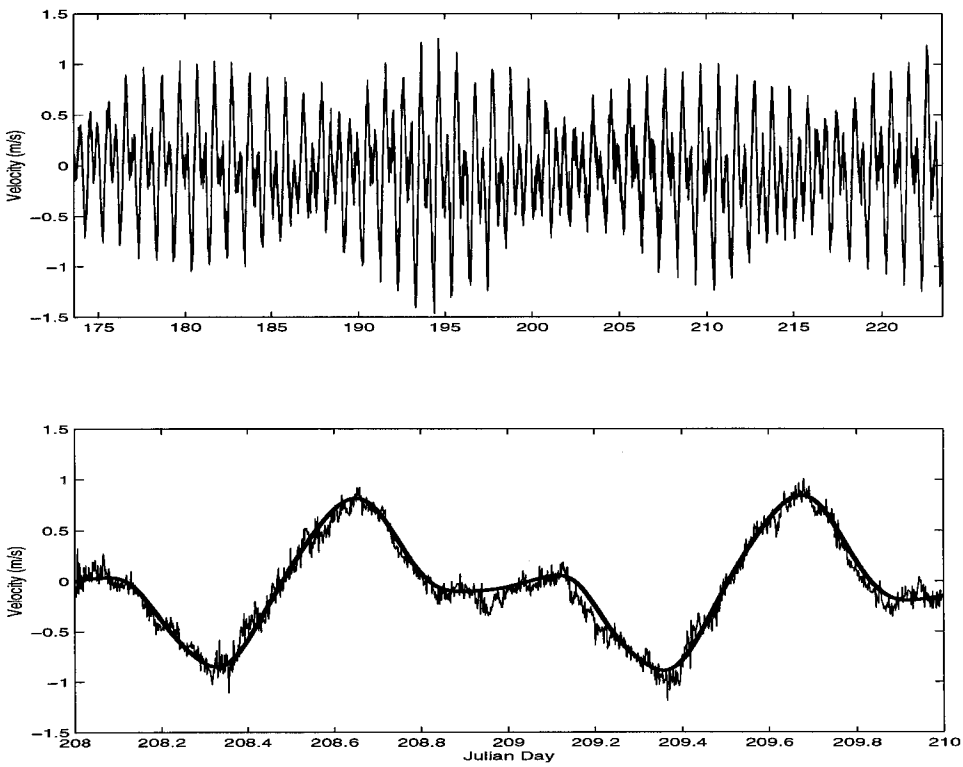

Figure 28: The total East - West velocity for the entire 1999 ADCP South deployment (top) and the total velocity with the tidal fit superimposed for a two day subsection (bottom).

prediction is quite accurate.

5.1.5 The Mean Flow

Just as one wants to separate the tidal component of velocity from the overall velocity, one also wishes to separate the mean estuarine flow from the total velocity. In essence one could take the mean of the entire record at each depth and come up with a profile. However this assumes that the estuarine flow is constant in time over the one or two month deployment. This is a doubtful assertion.

The estuarine circulation is forced by the input of fresh water from rivers flowing into the Strait of Georgia and Puget Sound. The Fraser River accounts for approximately half of all the fresh water that exits through Juan de Fuca Strait, and is well monitored. Records of volumetric flow from Hope show that the annual mean discharge is steady through April, quickly climbs to a peak in mid-June and then slowly decreases until by October it has largely returned to the winter low [*Ott*, 2000]. The moorings are generally deployed by mid-June, at or slightly before the peak freshet, and are recovered one to two months later. However, two months after the peak freshet the annual mean volumetric flow at Hope is reduced by about 40%. It is to be noted that the record from individual years is considerably noisier and can have several peaks. Regardless, the point is that the freshwater input into the estuary can have significant variation over the length of the deployment, and so the estuarine flow may not be best estimated as the mean over the entire record.

As well as the annual cycle of freshwater input into the Strait of Georgia, there is a spring-neap variation in the mixing within the Gulf Islands [*Griffin and LeBlond,* 1990]. This has the effect of varying the volume of brackish water output from the islands into Juan de Fuca Strait, such that more water is exported during

neap portions of the cycle than during spring tides. Thus, I will usually estimate the estuarine flow by applying a filter with a cut off at about 4 days.

5.2 Temperature Chain Data

The temperature chain data consist of individual time series from a number of internal recording sensors located on simple taut-wire moorings. First we shall discuss some problems with the time-series, then map the individual time series into a depth frame and finally map from temperature to density.

5.2.1 Temperature Time Series

We first need to adjust the time series for clock drift, which could be as much as 10 minutes over the entire record. We assume that the drift is linear and adjust the time series accordingly. Note that this now means that all the temperature pods are on a slightly different time basis. We therefore interpolate to a standard 6 minute grid across all instruments.

The temperature time series were generally quite good from the multi-sensor instruments (T/Ps and T/Cs). However, many of the temperature-only sensors experienced significant holes in the data record. It was only when plotting a spotty record alongside a complete record from a nearby temperature pod that it became evident that the pods had not simply recorded for a while and failed, but had rather turned on and off intermittently.

To fix these breaks I would use a nearby complete record, and trace along in time until they obviously decorrelated. The spotty record was then broken at this point and translated along the remainder of the complete record until the two correlated again. Certain temperature records would have quite a few of these

breaks. After doing this a few times I noticed that the width of the break was exactly one day. Checking across all the instruments showed that they seemed to have an engineering flaw whereby they went to sleep at random periods, usually for an integral number of days, and then woke up again. Data fragments that were not clearly able to be correlated with adjacent time series records were ignored. Small data gaps of less than eight points were filled with splines.

5.2.2 Mapping Instruments to Depth

If the mooring was locked in space then the instruments would be fixed to a particular height above the bottom. However, the strong tidal currents can exert significant drag on the mooring, causing it to lay over in the water column. The mooring motion was modelled with R. Dewey's mooring motion routines, using the velocity records from the S4 current meters [*Dewey* 1999]. This program is able to map the height of a given instrument as a function of time as the mooring moves about in the tide. For the 1998 and 1999 temperature chain moorings the maximum displacement of the top of the mooring was never more than 3 or 4 meters. However, the earlier 1997 T-chains used a standard round float, rather than an aerodynamic clamshell float, and had displacements of over 20 meters. The data were interpolated to a standard height grid to give temperature every 5 meters in the vertical and 6 minutes in time for each temperature chain mooring.

We should note that in certain cases where one or more adjacent temperature pods failed, one may have a large segment (20 meters) in the middle of the water column with no data. No attempt to interpolate across holes of this size was made, instead the data blank was left blank.

5.2.3 Mapping Temperature to Density

Before proceeding to the hard problem of determining density from temperature, we should check that the temperature records are sensible. To do this I compared CTD drops that were within a $1.5\,km$ radius of the mooring to the gridded temperature record. An example of this type of comparison is given in figure 29. The dots represent all the temperature measurements for a half-hour window flanking the CTD drop. This gives an indication of the heaving of isopycnals by high frequency internal waves. The temperature records seem to capture the large scale structure, and often flank the CTD temperature which in these cases was taken between the two moorings. I therefore trust the temperature gridding to be reliable.

Temperature is not the dominant contributor to density in Juan de Fuca Strait. In order to determine density one needs to examine the T-S characteristics of the water. This means that one needs the T-S correlation to be fairly tight over the portion of the water column that one is using, and one needs to adequately measure the time variability of this T-S relation. I have two types of instruments that simultaneously measure both temperature and salinity. The four T/C pods give us a time series of T-S, albeit at only one depth. The CTD casts give good spatial structure but lack the temporal resolution. I shall attempt to merge these two records to give a full depth, slowly time-varying T-S relation. Obviously, I need to perform this calculation separately for each year, but also separately for widely spaced moorings (such as 1998 North and 1998 South).

I actually perform the easier task of mapping a select set of isopycnals onto temperature. Thus for a given density, I calculate a time series of matching temperatures which optimally fit the data. Because the T-C pods are located either at

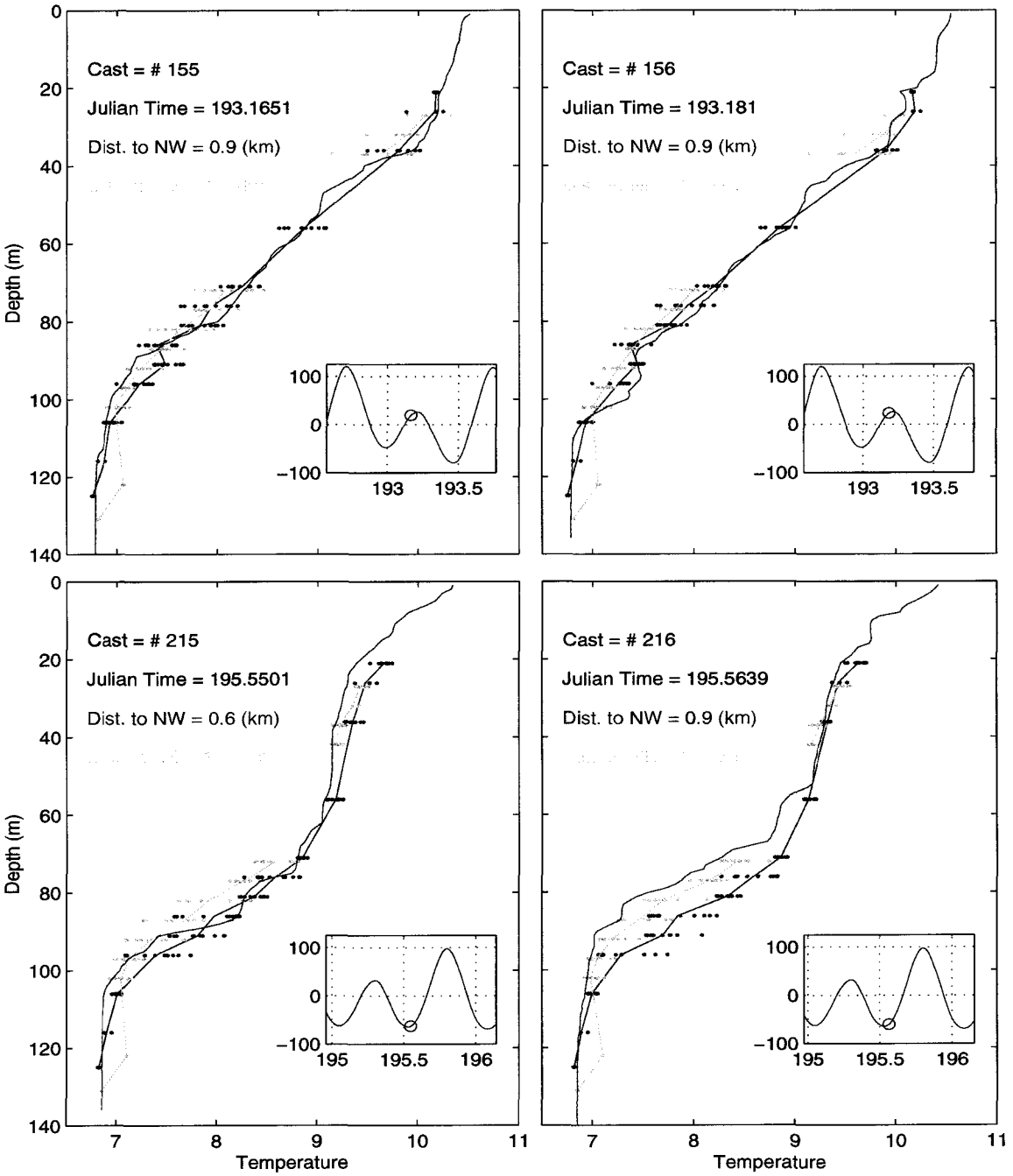

Figure 29: A comparison of four CTD profiles (blue) with the nearby temperature chains from 1998. The dots represent the T-Chain temperatures for the surrounding half an hour, to account for internal wave heaving, while the red and green lines are the average of the dots. The phase of the tide is shown in the small insets.

the very top or the very bottom of the temperature chain, they are only of marginal use. The top ones are in the near surface water whose T-S relation is quite variable, which makes the individual sensor records interesting, but difficult to generalize to the rest of the water column. The lower pods are very near the bottom, located in a relatively uniform pool of deep in-flowing water. Thus, the CTDs end up supplying much of the interpolation input, which is problematic since there are large stretches of time when no CTDs were taken.

To move further, I assume that the $T \rightarrow \rho$ relation is dominated by two resolvable time scales; a long-term drift encompassing seasonal changes, and a spring-neap cycle. There is a dominant tidal cycle visible in the temperature records, but it is not prominent in the density since salinity compensates. The highly sampled periods around deployment and recovery are used to infer the magnitude and phase of the spring-neap cycle for each of my selected isopycnals. On top of this is overlayed a slowly varying drift inferred from all the CTDs and the T-C pods. This results in a daily grid of temperatures, that correspond to the pre-selected isopycnals. Splines are then fit to this temperature mapping, to generate a $T \rightarrow \rho$ lookup table on the same time grid as the temperature pod records.

Because I have inherently ignored the diurnal and semi-diurnal tides, these will be wrong in the data. They will tend to be overestimated since we don't resolve the compensating salinity fluctuations. Although, I suppose that it is possible that the salinity could change in a manner so as to increase the density gradient, but this does not seem likely. It would be nice to fix this, but I lack the data to perform a better mapping. One could look at the T-C pods and perform a spectral analysis that calculates the transfer function between T and ρ, and then use this to correct ρ-spectra. However, one could not generalize the observed transfer

function to other depths with any confidence.

5.3 Reynolds Stress Calculation

The calculation of the Reynolds stress must be undertaken with care since the results will depend on both the temporal decomposition, into mean and fluctuation, and the choice of spatial orientation of the axes. Furthermore the average Reynolds stress may be hidden by significant variability, which requires careful ensemble averaging to expose.

As discussed in 5.1, the velocity data are decomposed into three components (the mean flow, the tidal flow, and the residual). The mean flow is the large scale, slowly-varying, estuarine circulation. The tidal component is derived from a harmonic analysis of the data, and includes both barotropic and baroclinic tides. The residual is a complex mixture of internal waves, vortical modes, and turbulence, as well as seiches. These three components each have an associated frequency band. The estuarine circulation is slowly varying with frequency, $\omega < 1$ cpd. The tidal component is composed of several discrete peaks with most of the energy at frequencies near 1 cpd and 2 cpd. The residual flow covers a broad frequency band, since it encompasses everything else, but its energy is primarily constrained within the internal wave range, $f < \omega < N$.

We shall calculate two distinct lateral Reynolds stresses. The first will consider the "mean" to be the tidal flow, while the second will consider the "mean" to be composed of the estuarine circulation. These two lateral Reynolds stresses will not be the same since they encompass different time and space scales, and hence average over a different set of processes.

5.3.1 Ensemble Averaging in the Time Domain

If the band of frequencies characterizing the residual fluctuations was higher than the frequencies characterizing the tide, we would have a spectral gap. This would mean that within each averaging window (1 hour) there would be several periods of fluctuations. Thus the Reynolds stress calculated over that window would be an independent measure of the "true" Reynolds stress. However in this case, the fluctuations occur on the same time scale as the tides, and so no spectral gap exists. One therefore needs to ensemble average the results of many measurements taken under similar conditions to achieve a statistically significant measure of the Reynolds stress. This assumes that the phase of the fluctuations is randomly distributed with respect to the phase of the tide.

When considering the effect of residual motion in transporting the momentum of the mean tide, I will start with a time block of length one hour, and consider sensitivity to this choice later. The choice of a one hour window means that there is a slight overlap between two neighbouring tidal phases. For example, a tidal current of $+30\,cm/s$ accelerating usually occurs less than an hour after the tidal current was $+10\,cm/s$ accelerating. Therefore, two one-hour blocks centered at these two points will overlap.

I choose to decompose the time series based upon the speed of the tidal current at the southern mooring, and also to distinguish between accelerating and decelerating currents. The southern mooring was chosen since it is furthest away from the boundary, and hence most likely to resemble the far-field tidal forcing. The accelerating and decelerating characteristic is used to distinguish between different phases of the tidal cycle.

Specifically, I take the depth-averaged tidal current for the southern mooring

and select times at which the tidal speed belongs to the set ($\pm 10\, cm/s$, $\pm 30\, cm/s$, $\pm 50\, cm/s$, etc.) One hour blocks centered on these times are then formed. Here the positive velocity refers to floods and the negative to ebbs. We avoid taking averages around slack since the tidal velocity is never zero. A $-10\, cm/s$ tide means that the tidal speed is $10\, cm/s$ and that the velocity projected onto an along-strait axis is oriented out to sea. Since the speeds are determined from the tidal decomposition only, which is a smoothly varying function, we do not encounter problems with picking multiple points clustered within the same one hour period.

Since the tide in Juan de Fuca Strait is mixed diurnal and semi-diurnal, any particular tidal state (eg. $+30\, cm/s$, accelerating) occurs almost twice per day on average. Thus for the 52 day deployment of the southern mooring we obtain almost 100 samples of the most common tidal states. The stronger tides occur less frequently since diurnal constituents often reduce the magnitude of one of the two floods/ebbs.

We could subdivide our group of ensembles even further by distinguishing between spring and neap, or by separating the first half of the record from the second (in order to account for changing freshwater input). However as a first attempt, I will only consider the phase of the tide as the only distinguishing variable. This ensures that the number of samples in each ensemble remains high and therefore should provide better statistics.

5.3.2 Choosing the Reynolds Stress Axis

Now that we have a given one hour block of the time series, one needs to choose the orientation of the axes, since this will determine u' and v'. Before proceeding it is useful to give a simple illustrative example of how the lateral Reynolds stress

is dependent on the choice of coordinate system. Figure 30 shows the same set of three fluctuations (with zero mean) in three different reference frames. The Reynolds stress estimate changes from zero in the top figure, to a negative number in the second and finally to a positive number in the third. The middle and lower panels are rotated by 26.5° clockwise and counterclockwise respectively.

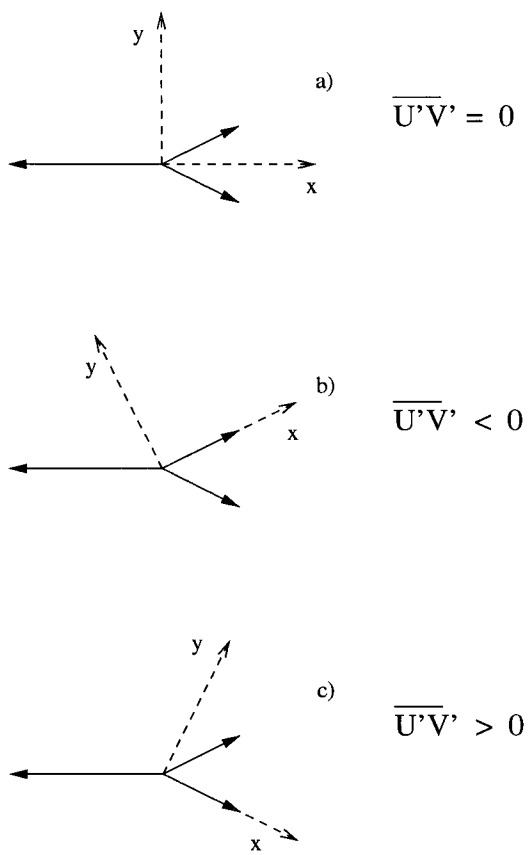

Figure 30: The same three fluctuations in three different reference frames. Rotating the reference frame changes not only the magnitude but also the sign of the Reynolds stress.

There are three obvious choices for an axis in this problem. The first is to choose the x-axis to lie along the mean isobaths near the mooring site. This choice

assumes that the bathymetry plays an important role in steering the fluid. The second choice is to set the x-axis to lie along the mean tidal velocity during that one hour block. This choice could be further subdivided into a depth-dependent (baroclinic) or depth-averaged (barotropic) frame. A third choice would be to pick the x-axis to lie along the major axis of the M2 tidal ellipse, since it is the largest single tidal component. Again this could be either a depth-dependent or depth-averaged quantity.

I will choose to use the depth-dependent average tidal velocity during the ensemble as the reference frame, although I will discuss sensitivity to the other choices. I choose not to use the bathymetric reference frame since it assumes that the bottom steers the fluid. Although this is predominantly true there are asymmetries between the flood and ebb. The M2 tidal ellipse does represent the single largest tidal component, however it still only captures 25% of the total tidal energy, although most of the other large constituents are similarly aligned. It also is incapable of capturing flood/ebb asymmetries. However the most compelling reason to choose a depth-dependent mean flow is to provide an unbiased measure of $\overline{uv}$ which is not contaminated by $\overline{uu}$ or $\overline{vv}$. As discussed earlier, an eddy viscosity assumption is not a good parameterization for the diagonal elements of the Reynolds stress tensor. Hence the more an axis differs from the direction of the "mean" current, the more of $\overline{uv}$ comes from the diagonal stresses, and the harder it is for an eddy viscosity to model the measured $\overline{uv}$ stress.

The average of the tidal velocity is calculated separately for each ensemble member, even for ensembles with the same tidal phase. In principle we could set the mean tidal velocity to be the average over all ensemble members with similar phase. However that choice would probably add a small amount of aliased tidal

current to the measured lateral Reynolds stress.

The axis was calculated based upon the tides at the southern mooring, for a given ensemble member, but this same axis was also used at the northern and eastern mooring. It is unlikely that the axes determined separately for the north and east mooring would coincide with the axis for the southern mooring. However, one needs to have a consistent x and y-direction for the comparison of the lateral Reynolds stress between moorings. This implies that the Reynolds stress calculated at the northern and eastern moorings will be contaminated by $\overline{u'u'}$ and $\overline{v'v'}$, but I need to pick some consistent axis in order to compare the stresses at different moorings.

5.3.3 Comparing Reynolds Stress at Different Moorings

Having determined the lateral Reynolds stress, $\overline{u'v'}$, at each mooring we now want to compare the values at different moorings. One could do this in a number of ways but for intuitive reasons, I have decided to compare data along isopycnals, as opposed to depth (height), or fractional water depth (height). In practice, isopycnal matching does not produce substantially different results from either a fractional depth or fractional height matching. The isopycnal depth structure is based upon CTD casts near each mooring, with a slowly-varying time component based upon the temperature chain time records.

In reality this ends up being much work for little gain. The isopycnal depths mapped between moorings are often very similar to mapping across a constant depth. Also, errors that appear in the isopycnal height calculation have little effect on the inter-mooring comparison, since the depth variation of the shear and stress is in general small. The bottom 20 m of the water column is usually masked to

remove the Reynolds stresses in the bottom boundary layer.

5.3.4 Cross-Channel Shear

The cross-channel shear is needed to calculate the eddy viscosity, through $\overline{u'v'} = -A_H \, \partial U/\partial y$. To calculate the cross-channel shear, as a function of depth, for each ensemble the axis is set to be the same as in the Reynolds stress calculation. The mean tidal velocity over an ensemble member plus the mean estuarine velocity at each mooring is projected onto the x-axis and this becomes the large-scale current, U. Although I am primarily interested in the tides, the fluctuating processes cannot distinguish between tidal shear and estuarine shear, so the mean flow shear has been included in the eddy viscosity calculation. The estuarine mean flow is predominantly along-channel so that neglecting it in the choice of axis calculation does not make a significant difference. Generally, the tidal currents appear to have little spatial divergence so that picking a single axis to represent the whole mooring array is plausible.

The change in the large-scale tide, ΔU, is calculated along isopycnals in the same manner as the Reynolds stresses. The cross-channel locations of the moorings are projected onto the y-axis and this gives a set of Δy values. I am also implicitly assuming that $\partial U/\partial x \; \Delta x \ll \partial U/\partial y \; \Delta y$, where Δx is the distance between moorings when projected onto the x-axis. With this mooring array $\Delta x \simeq \Delta y$, so that the assumption is that the cross-channel gradient is much larger then the along-channel gradient. This is generally a good assumption (and largely holds true in the data).

Because there are only three moorings with full depth resolution we can only measure the shear at three places: half way between the North and South mooring,

half way between the North and East mooring, and half way between the East and South mooring. It is therefore difficult to predict the shear at the two extreme moorings (North and South) but we get a reasonable measure of the shear at the East mooring by using the difference in velocities between North and South (refer to figure 21). If all the three shears looked similar (ie. the current was linear), I would be somewhat confident in extending that value to the outside moorings. There are S4 current meters on the top and bottom of the temperature chains, one in the center of the ADCP triangle and one even further offshore than the southern mooring (figure 21). These provide some confidence that the scale of variation in the tidal current is larger than our array, but the lack of full-depth coverage means that they cannot be used in the lateral shear calculations.

We now have three sets of depth-dependent lateral Reynolds stresses (measured at the moorings) and three sets of depth-dependent cross-channel mean shear (measured at the mooring mid-points). These give a number of different eddy viscosities depending on the pairing of stress with shear. The most believable set is given by comparing the lateral Reynolds stress from the East mooring (ie. central ADCP) with the shear calculated from the North and South moorings (ie. outside ADCPs). However this will under-estimate the shear in cases where the curvature of the tidal flow ($\partial^2 U/\partial y^2$) is important. It also assumes that the flow can be regarded as slowly varying in the along-channel direction. Regardless, I shall use it as the primary example with occasional referrals to other possible pairings.

5.3.5 Uncertainties and Error

Error bars will need to be determined for the Reynolds stresses and the shear and subsequently for the eddy viscosity. We will primarily use a bootstrap method [*von Storch and Zwiers*, 1998] to calculate confidence limits, but I also wish to discuss an alternate method of looking at the error for lateral Reynolds stresses.

Given a set of three horizontal Reynolds stresses ($\overline{u'v'}$, $\overline{u'u'}$, $\overline{v'v'}$) in a given reference frame one can calculate the angle, θ, through which the axis must be rotated to give $\overline{u'v'} = 0$. This is given by the solution to

$$2\overline{u'v'}\cos 2\theta + (\overline{v'v'} - \overline{u'u'})\sin 2\theta = 0. \tag{72}$$

There will of course be one of these angles in each quadrant. We can then express the uncertainty in $\overline{u'v'}$ using as the angle between the chosen axis and the axis at which the lateral Reynolds stress would vanish. The advantage in this case is that we are not necessarily dismissing small values of the lateral Reynolds stress, which might be statistically indistinguishable from zero in a bootstrap sense.

5.4 Computing Vorticity and Divergence

With three moorings measuring two velocity components each, we are able to calculate first spatial derivatives of the velocity under the assumption that the higher spatial derivatives of velocity, ($\frac{\partial^2 u}{\partial x^2}$, $\frac{\partial^2 u}{\partial y^2}$, etc.) are negligible. So there is a unique solution set ($u_0, v_0, \frac{\partial u}{\partial x}, \frac{\partial u}{\partial y}, \frac{\partial v}{\partial x}, \frac{\partial v}{\partial y}$) which reproduces the observed velocities ($u_N, v_N, u_E, v_E, u_S, v_S$) given the array geometry.

Equivalently, one can obtain the vorticity through a circulation calculation. This inherently has the same assumption about neglecting higher derivatives, since

one estimates the velocity along an array side by taking the average of the two end-point velocities. It is easy to show that the two methods produce an identical estimate of the vorticity

5.4.1 Array Response to Internal Waves

The 1999 array is not measuring the relative vorticity at a point that was calculated for internal waves in section 3.2.3. Instead it is inferring vorticity from the measurement of velocity at three distinct points. Thus we need to calculate the relative vorticity that the array would measure given the presence of internal waves.

One can set the x-axis to lie along the direction of the wavevector, which gives internal wave velocity components of,

$$\begin{aligned} u(x,z,t) &= \frac{im}{k} w(x,z,t), \\ v(x,z,t) &= \frac{fm}{\omega k} w(x,z,t), \\ w(x,z,t) &= w_0 \sin(mz)\, e^{i(kx-\omega_i t)}. \end{aligned} \tag{73}$$

With no loss of generality the array looks like the following.

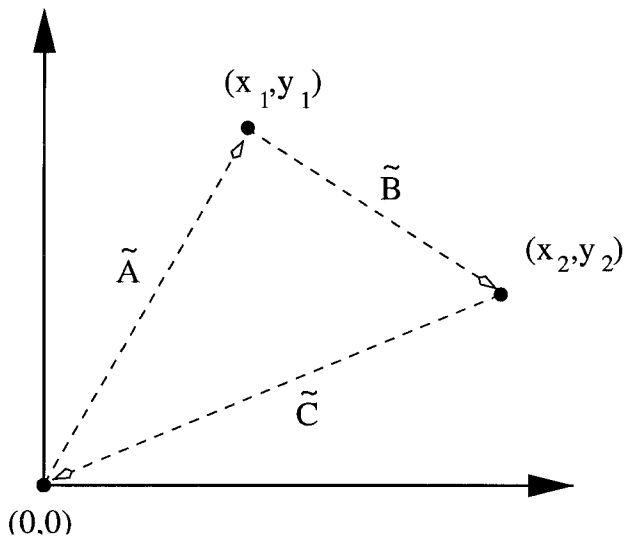

The circulation can be expressed as

$$\Gamma = \frac{1}{2}(\tilde{u}_A \cdot \tilde{A} + \tilde{u}_B \cdot \tilde{B} + \tilde{u}_C \cdot \tilde{C}), \tag{74}$$

where $\tilde{u}_A$ is the velocity at the mid-point of the vector $\tilde{A}$, etc. For the internal waves in (73) this gives,

$$2\Gamma = \left((1 - e^{ikx_2})(ix_1 + \frac{f}{\omega}y_1) + (e^{ikx_1} - 1)(ix_2 + \frac{f}{\omega}y_2) \right) \frac{m}{k} w_0 \cos(mz)\, e^{-i\omega_i t}. \tag{75}$$

Given the area of the enclosed triangle, $\Delta ABC = \frac{1}{2}(x_2 y_1 - x_1 y_2)$, then the vorticity can be written,

$$\zeta = \frac{(1 - e^{ikx_2})(ix_1 + \frac{f}{\omega}y_1) + (e^{ikx_1} - 1)(ix_2 + \frac{f}{\omega}y_2)}{x_2 y_1 - x_1 y_2} \frac{m}{k} w_0 \cos(mz)\, e^{-i\omega_i t}. \tag{76}$$

If the wave is large compared to the size of the array, ($kx_1 \to 0$, $kx_2 \to 0$),

then the exponentials can be approximated as $e^{ikx} \approx 1 + ikx$, and the vorticity reduces to the expected form

$$\zeta = -\frac{ifm}{\omega} w_0 \cos(mz)\, e^{-i\omega_i t}. \tag{77}$$

However, if the internal wave is of the order of the array, or smaller, then the measured vorticity can be seriously skewed. Consider for simplicity, a wave propagating at an angle such that $x_1 = 0$. Then the vorticity reduces to

$$\zeta_{x_1=0} = \left(\frac{1 - \cos(kx_2)}{kx_2} - i\frac{\sin(kx_2)}{kx_2} \right) \frac{fm}{\omega} w_0 \cos(mz)\, e^{-i\omega_i t}.$$

Clearly, if the array is large compared to the wavelength of the internal wave, $kx \to \infty$, then the measured vorticity goes to zero. Even if the wavelength is four times (two times) the array separation, then $kx_2 \approx \pi/2$ ($kx_2 \approx \pi$), and the measured vorticity is off by a factor of $2\sqrt{2}/\pi$ ($2/\pi$). Furthermore if the array is exactly the same size as the wavelength then $kx_2 \approx 2\pi$, and one measures no vorticity at all. Thus the array will underestimate the vorticity for most internal waves. One can similarly show that divergence is poorly resolved for waves that are not at least twice as long as the array spacing, O(1 km).

There is also directional sensitivity in the array, so that the fraction of measured to intrinsic vorticity is dependent on the angle at which the wave encounters the array geometry. One can calculate this directional sensitivity for our array as a function of incident angle, θ, and horizontal wavelength, $\sqrt{k^2 + l^2}$ (or alternatively frequency). Although there is a dependence on angle, it is not generally overwhelming. Also I have no way of using this information to correct the observed vorticity. It thus seems best to just note its possible influence, but ignore

the effect of wave directionality.

5.4.2 Doppler Shift Effects on Vorticity

I expect that the Doppler shift of the current will have an effect on my ability to correctly diagnose vorticity. In particular, there will be a problem in linking the observed vorticity frequency spectrum to the predictions for internal waves, because frequency is not properly resolved.

Let us consider that the vorticity for an internal wave propagating in the x-direction can be equally well represented as any of the following,

$$S_\zeta(\omega) = \frac{f^2 m^2}{\omega_i^2} \cot^2(mz)\, S_w(\omega), \tag{78}$$

$$= \frac{f^2 k^2(\omega_i)}{\omega_i^2} S_u(\omega), \tag{79}$$

$$= k^2(\omega_i)\, S_v(\omega), \tag{80}$$

where ω_i is the intrinsic frequency, and $S_\zeta(\omega)$ is the frequency spectrum of ζ, etc. The problem in diagnosing will arise since the coefficients relating any two spectra depend on the intrinsic frequency, as opposed to the observed Doppler shifted frequency. However, one could correct for this by first insisting that the different methods of predicting vorticity all give comparable vorticity spectra. There is an inherent assumption about the contribution of the vortical mode vs. the internal wave to each of the three velocity spectra. However, it does enable one to make a very crude estimate.

Let us define $A(\omega)$ as

$$A(\omega) = \frac{S_u(\omega)\, k^2(\omega)}{S_w(\omega)\, m^2}, \tag{81}$$

where $\omega = \omega_i + \tilde{U} \cdot \tilde{k}$ is the observed frequency. In a non-Doppler shifted frame $A(\omega)$ would be everywhere equal to 1. This makes a large assumption in representing a tidally averaged Doppler shift as a single number. One can use

$$\frac{S_u(\omega)}{S_w(\omega)} = \frac{N^2 - \omega_i^2}{\omega_i^2 - f^2}.$$

to rewrite (81) as

$$\frac{N^2 - \omega_i^2}{\omega_i^2 - f^2} \frac{\omega^2 - f^2}{N^2 - \omega^2} = A(\omega). \tag{82}$$

One can substitute for the intrinsic frequency, using $\omega_i = \omega - \tilde{U} \cdot \tilde{k}$, and get a quadratic for the unknown $\tilde{U} \cdot \tilde{k}$ in terms of the the observed scaled spectral ratio, $A(\omega)$, and the observed frequency, ω. Solving gives two curves for $\tilde{U} \cdot \tilde{k}$ as a function of the observed frequency, ω. These predicted Doppler shifts could be used to correct the internal wave vorticity, so that we obtain consistent vorticity estimates regardless of which velocity spectra is used. However, this assumes that the horizontal velocity, and vorticity, are due to only internal waves.

6 Lateral Reynolds Stress

In this section we shall examine the results of the Reynolds stress analysis. I start with the effect of medium scale processes (eg. internal waves and vortical modes) on the tidal momentum. First, we shall examine the basic results and then turn to additional factors, such as spring-neap variability. Finally, I present the analysis for the effect of the tide on the momentum in the estuarine mean flow.

The results of these lateral Reynolds stress calculations for the effect of internal waves and vortical modes on the tidal flow are shown in figures 31 through 34. Figure 31 shows the Reynolds stress ($\overline{u'v'}$) as a function of depth for each mooring for flood tide (in the upper panel). The lower panel shows the large-scale flow in the x-direction, $U(y)$, and can be used to examine the cross-channel shear, $\frac{\partial U}{\partial y}$. Figure 32 is the same as figure 31 but for ebb tides. Figures 33 and 34 show the Reynolds stresses $\overline{u'u'}$ and $\overline{v'v'}$ respectively. The flood and ebb are plotted on the same figure and the shear is the same as in the $\overline{u'v'}$ plots. Successive phases of the tide are offset from each other for clarity.

The lateral Reynolds stresses $\overline{u'v'}$ typically have values around $0.001\,m^2/s^2 - 0.002\,m^2/s^2$. They exhibit some low mode structure, but are reasonably correlated over vertical scales of $10 - 20\,m$. There are also certain striking features, such as the large node of negative $\overline{u'v'}$ in the East ADCP data at $70\,m$ depth around $-70\,cm/s$ decelerating (red dots in figure 32). The South (blue) and East (red) ADCP stresses are quite correlated, but the North (green) mooring exhibits different behaviour. The coloured numbers represent the number of different samples that went into each ensemble. For periods around peak ebb and peak flood the number of ensembles may be quite low, and so the averaging is less believable. I have chosen to only plot results which are significantly different from 0 at an 80%

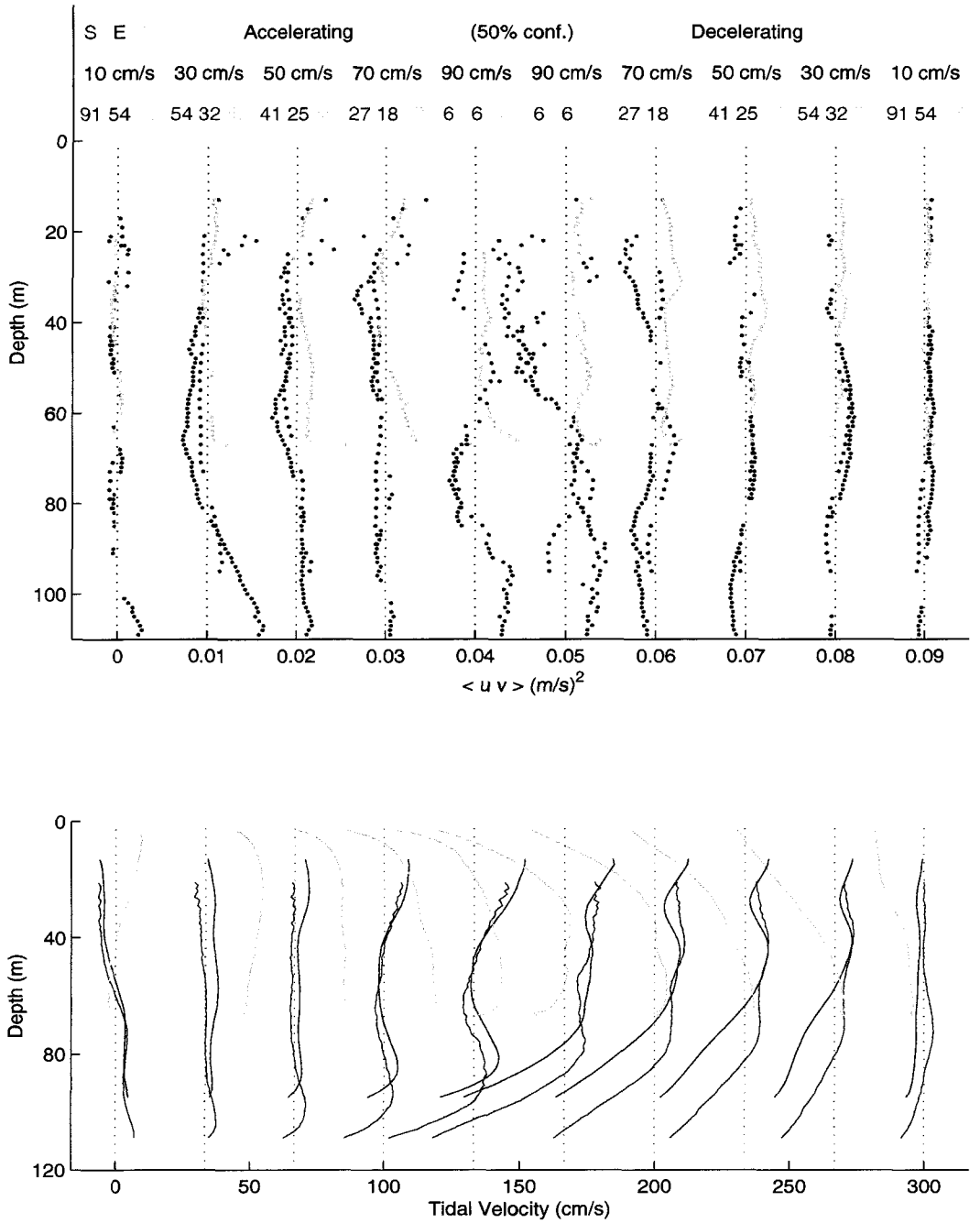

Figure 31: The Reynolds stress $\overline{u'v'}$ for flood tide (top panel) and the associated mean flow, $U(y)$ (bottom panel). Colours represent the south ADCP (blue), east ADCP (red), and north ADCP (green). Coloured numbers represent the number of ensembles in the average. Stresses which are not significantly different from 0 at an 80% confidence intervals are not plotted. Successive plots are offset by 0.010 m^2/s^2 (top) and 0.333 m/s (bottom).

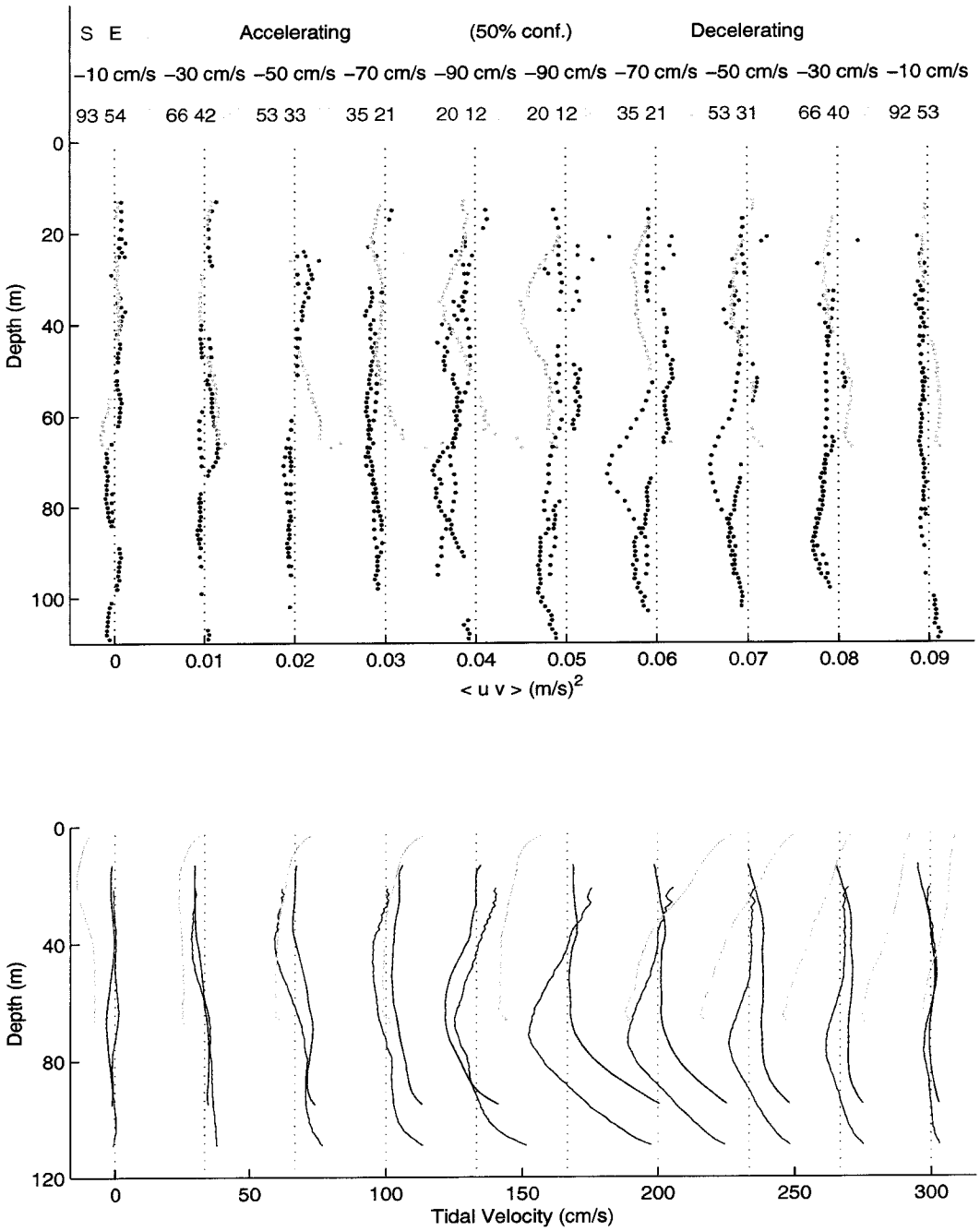

Figure 32: As in figure 31 but for ebb tide.

confidence interval. This removes most of the spurious data particularly near the surface, but still allows one to see the general vertical structure.

The velocities (and implied shear) plotted in figures 31 and 32 are largely consistent with a simple tidal flow that changes first near a boundary, so that the North mooring leads the East mooring which leads the South mooring. Also, in all moorings the bottom leads the upper water column. The vertical structure is quite similar between the East (red) and South (blue) moorings, although the North (green) mooring is often quite different. Also it appears that shear between the North and East moorings is generally larger than the shear between the East and South moorings.

The bottom boundary layer is quite pronounced in the South and East moorings showing very large shears of $30 - 50\, cm/s$ over only $20 - 30\, m$ around peak flood and ebb. The north mooring has a very quiescent surface layer, it is not plotted upside down, which never seems to move faster than about $60\, cm/s$. I think that this may be due to the influence of the water which resides on the shallow ($< 20\, m$ depth) shelf just on-shore of the north mooring. Some form of exchange flow could mix slower moving shelf water out over the mooring, although the $\overline{u'v'}$ signal in the surface layer does not appear distinguishable from the one at depth. However, if there is a shallow front that separates shelf water from offshore water then we would not need large persistent Reynolds stresses.

The diagonal Reynolds stresses $\overline{u'u'}$ and $\overline{v'v'}$ are larger than the lateral component $\overline{u'v'}$ by factors of about 6 and 3 respectively. They are largely uniform with depth with increasing levels near the surface and bottom. The extremely large values observed in the southern mooring data near the surface are a matter of concern. However the fact that they are strongly modulated by the tide makes me

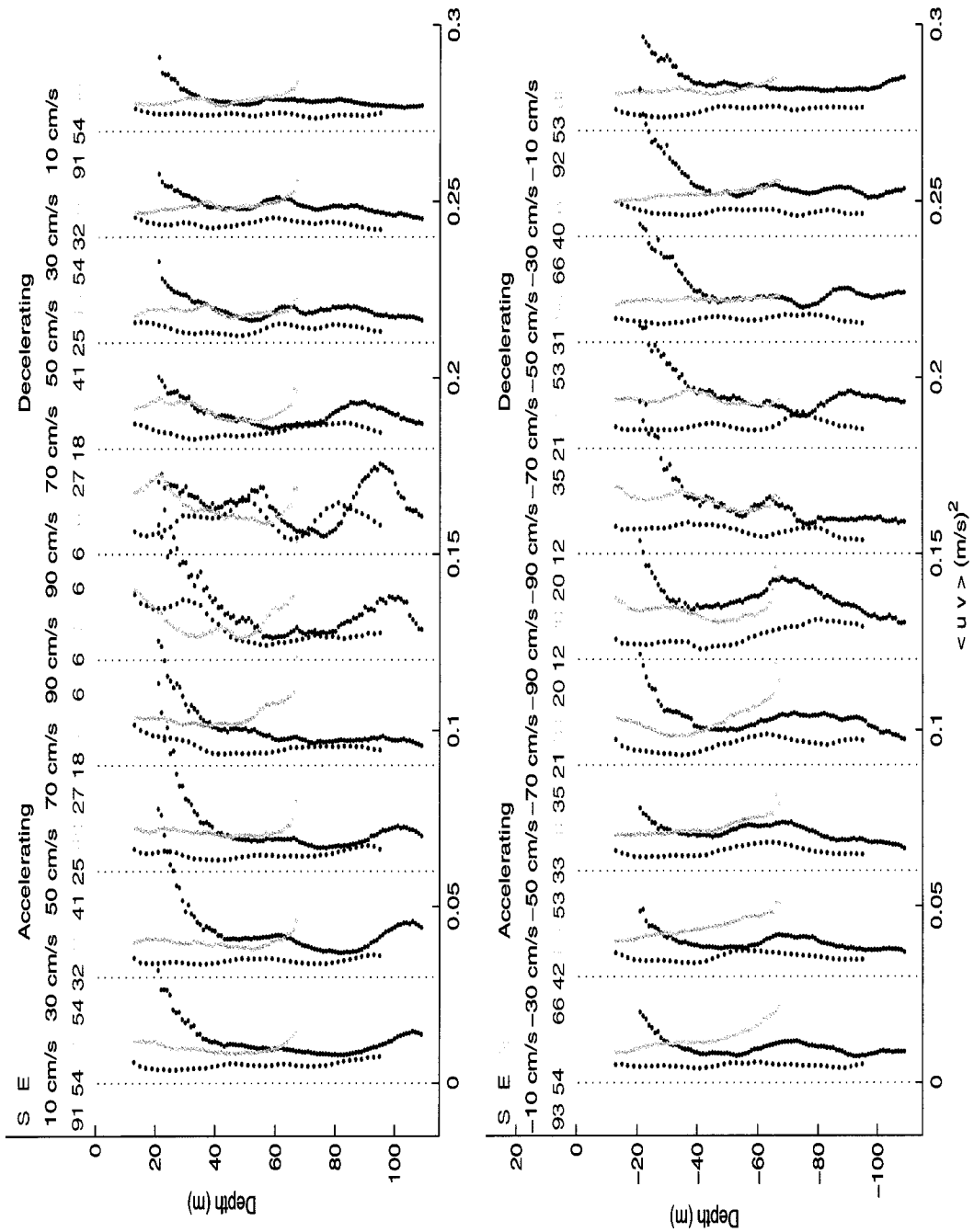

Figure 33: The Reynolds stress component $\overline{u'u'}$ for both flood and ebb tide. Colours are as in figure 31. Shears are the same as for the $\overline{u'v'}$ component. Successive plots are offset by $0.04\,m^2/s^2$.

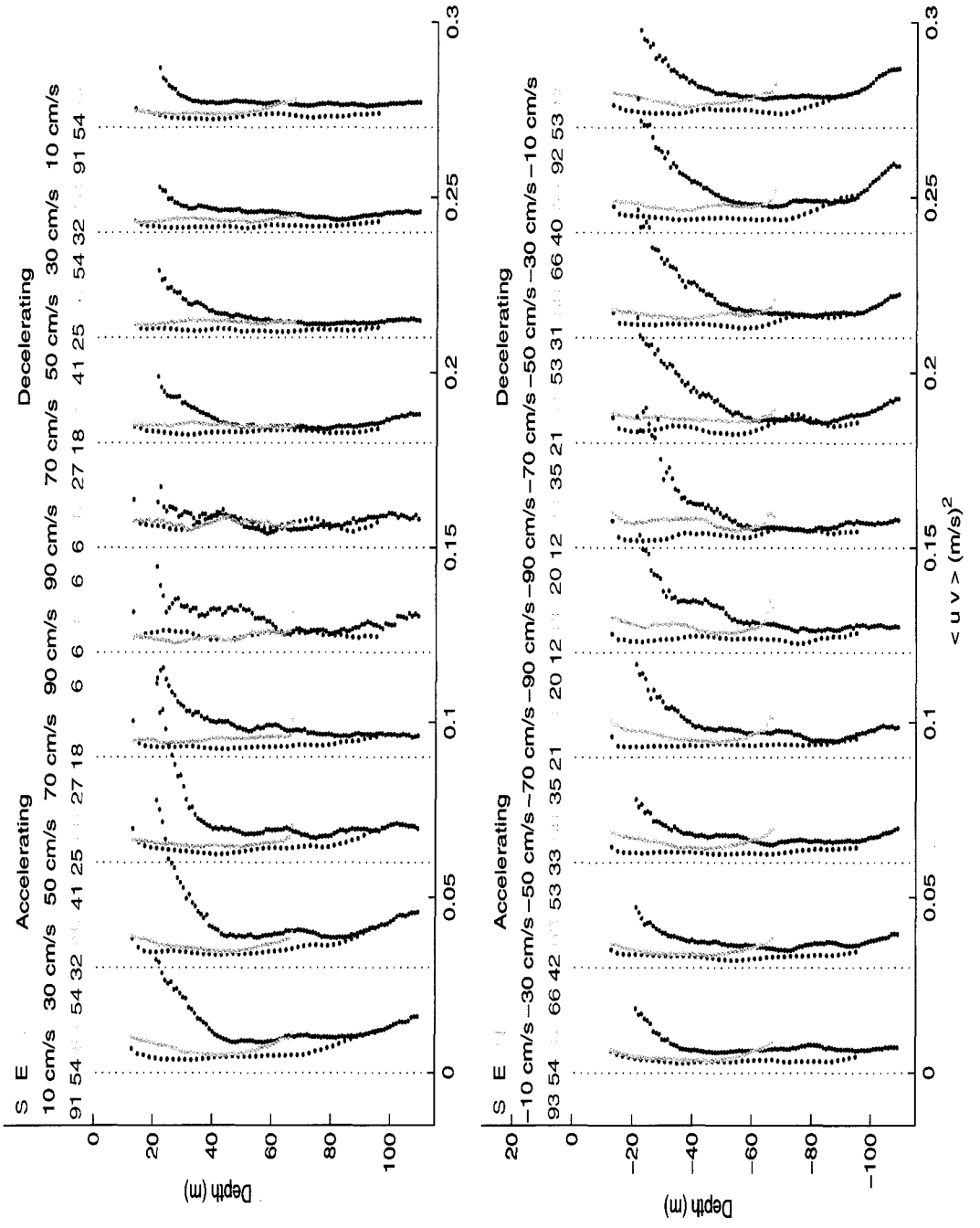

Figure 34: As in figure 33, but for the component $\overline{v'v'}$. Successive plots are offset by $0.03\,m^2/s^2$.

more confident that they are not simply measurement errors due to beam spreading. These large values in the South ADCP stresses appear when the tide shifts from peak ebb to peak flood, which corresponds with times when the tidal flow is accelerating against the surface mean outflow. However, we do not see a corresponding increase in bottom layer $\overline{u'u'}$ and $\overline{v'v'}$ when the tide is accelerating outward, but this may be due to weaker bottom layer currents.

The North (shallowest) mooring exhibits slightly different behaviour than the other two moorings in that its $\overline{u'u'}$ values are quite elevated with respect to its other Reynolds stress components. The ratio $\overline{v'v'}/\overline{u'u'}$ which is similar for the east and south moorings is significantly reduced at the north mooring. This could be due to the boundary influencing internal wave, and forcing them to be more rectilinear. The North mooring is also different in that the average $\overline{u'v'}$ is positive as opposed to the South and East moorings which have slightly negative means. All these means are quite weak, O($0.0002\, m^2/s^2$), but distinguishable from 0 with 99.9% confidence.

Figure 35 shows the data from the 1998 North and South moorings (refer figure 21). Although we have no large scale shear with which to compare these observed Reynolds stresses, it is interesting to observe the magnitude and general behaviour of the stresses as a function of the tidal cycle. As a reminder the North mooring is about a third of the way across the strait, located on a small rise, and the South mooring is located very close to the US shore on a steep (1:8) slope. Thus, they are expected to experience shears of different sign during the same phase of the tide, and hence should have Reynolds stresses of different sign (which is largely true). The magnitude of the Reynolds stress is similar to the 1999 moorings. Also if we assume a simple cross-channel velocity which leads at

the boundary, then the sign of this conceptual shear is qualitatively in agreement with a positive eddy viscosity. There are also depth intervals of very elevated stress which tend to occur shortly after peak ebb or flood. However, these could be singular wave events that have not been sufficiently smoothed by the ensemble averaging (due to the lower number of ensembles near the peak velocities).

6.1 Reynolds Stress Sensitivities

Before proceeding with the analysis we should check that the signal is robust and not overly sensitive to the choices that went into the calculation. The two most important choices are the length of averaging time and the choice of orientation of the axis. There are other concerns as well, such as with averaging spring and neap signals together.

Figure 36 shows the $\overline{u'v'}$ Reynolds stresses for flood tide calculated with a 30 minute window as opposed to a one hour window. The plot is directly comparable with figure 31. The 30 minute Reynolds stresses exhibit nearly identical structure to the one hour averages. Furthermore they are roughly equal in magnitude; within 5% on average and generally differ by less than $0.0001\, m^2/s^2$ except near the surface. The diagonal stresses are in even better agreement with $< 1\%$ difference on average. Similar results hold for a 2 hour time window.

There are two ways to think of this insensitivity to the time window (at least within the range of 20 minutes to 2 hours): first that all the processes that contribute to the Reynolds stress have very high frequencies, and second that they are predominantly very low frequency (at least compared to the averaging window). The first case is the more common, although in this case, the wrong assumption. It assumes that the Reynolds stress is predominantly composed of high frequency

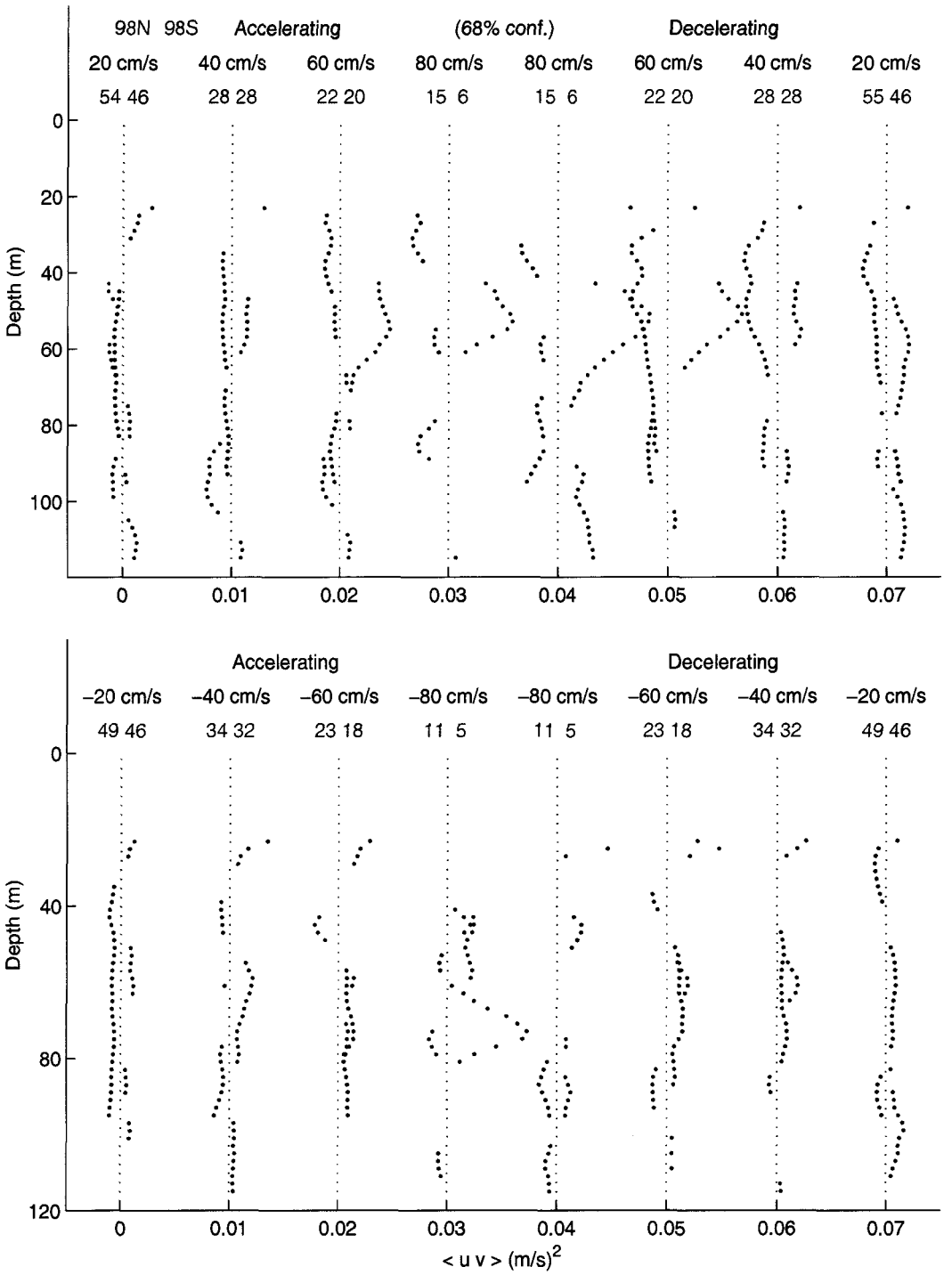

Figure 35: The lateral Reynolds stress ($\overline{u'v'}$) for the 1998 North (blue) and South (red) moorings. Axes are calculated independently for each mooring.

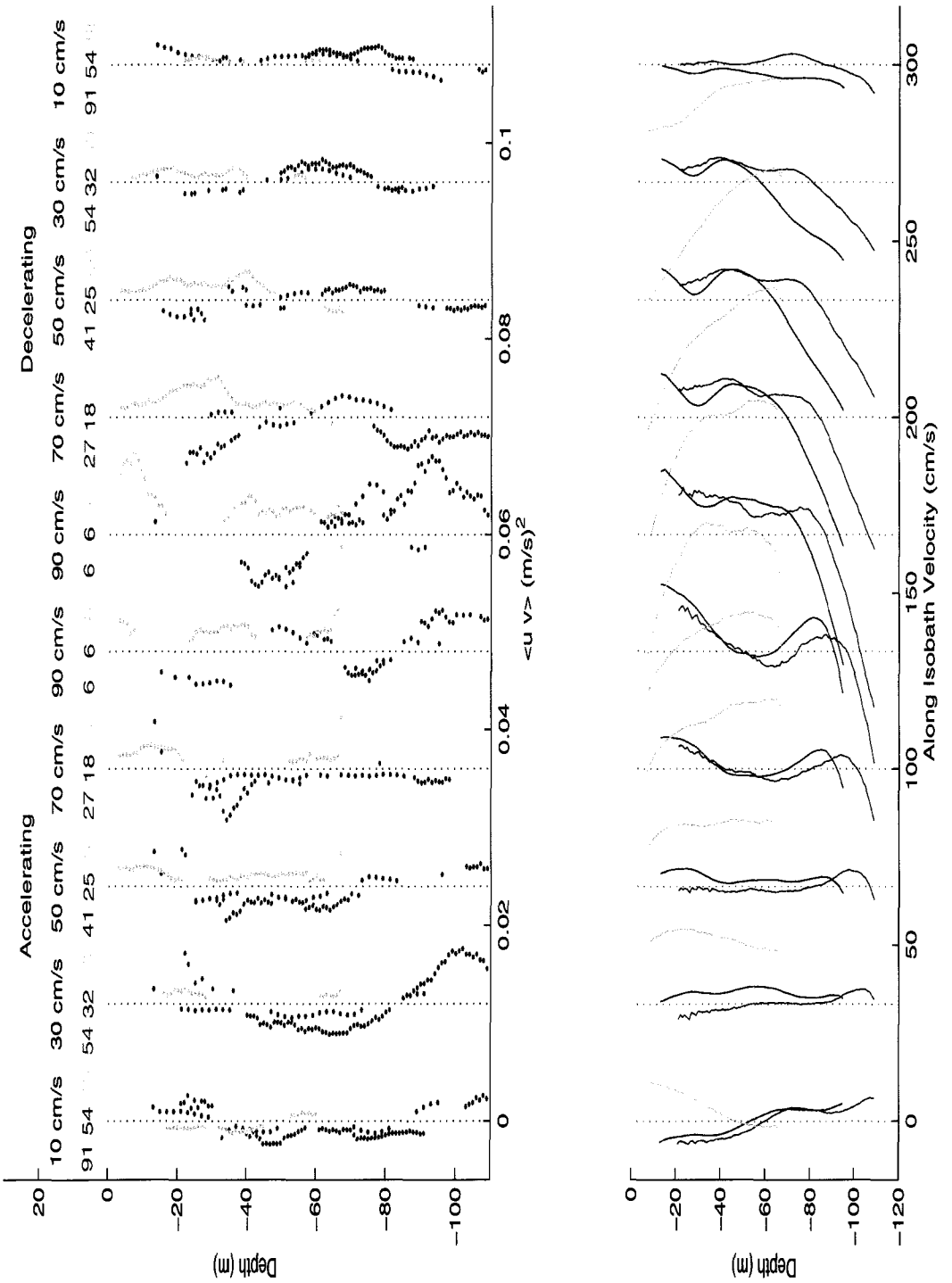

Figure 36: The lateral Reynolds stress $\overline{u'v'}$ calculated with a 30 minute time window, instead of the one hour window used in figure 31.

fluctuations which are fully resolved by each averaging window, and so averaging over 30 minutes or 2 hours makes no difference. This would also imply that different realizations that go into each ensemble should be similar, which is most decidedly not true. The second case assumes that the predominant processes in the Reynolds stress have periods greater than any of the averaging windows. Thus the different realizations are all quite distinct, since they only capture portions of each contributing process around a different phase each time, and are only coherent in the ensemble average. This is the case in the data where the individual realizations produce highly variable Reynolds stresses. Presumably though a smaller time window may need a larger set of ensembles to become statistically significant. We can see some indication of this since the variance in the 30 minute time window ensemble average is about 20% larger than for the one hour window. The one hour window therefore seems justified, since it provides a balance between having a long window to reduce the variance, and having a short window to concentrate on a particular phase of the tide.

Let us now consider the choice of orientation of the axes. One of the subtle changes I could have made was to select an axis that was still based upon the average tide over the ensemble window, but used a single depth-averaged frame instead of a depth-varying frame which changed slightly from bin to bin. The result of the barotropic axis calculation is shown in figure 37.

There is really very little difference between the Reynolds stresses calculated in a depth-averaged and a depth-dependent frame. The largest changes occur for small tidal velocities, when there is the most variation in the tidal angle with height, and even these are quite small. Using some of the other proposed axes, such as a frame fixed to the isobaths, produces similarly small changes. The

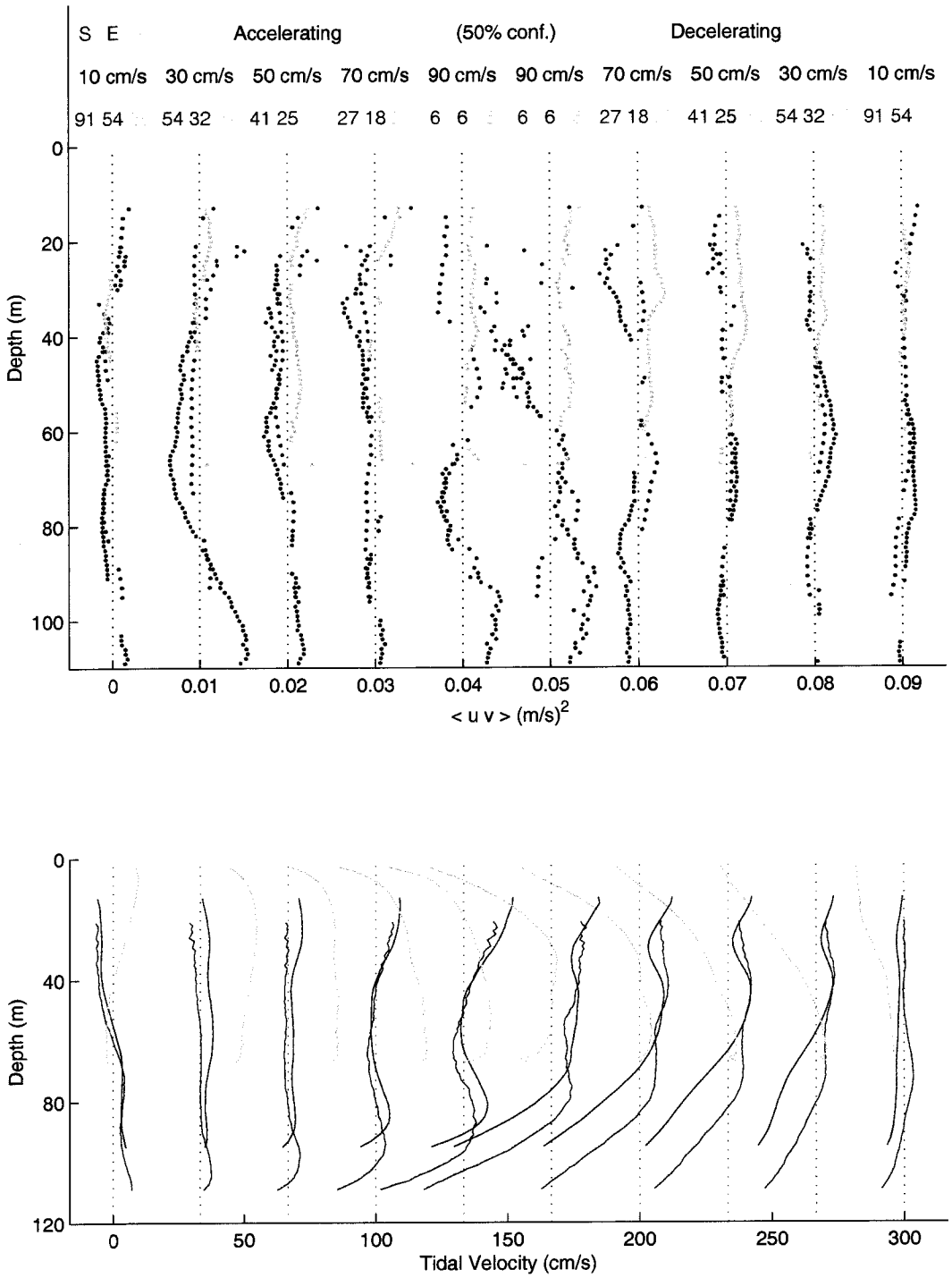

Figure 37: The flood tide Reynolds stresses, $\overline{u'v'}$, calculated using a depth-average reference frame.

reason for this insensitivity is that all the sensible choices give nearly the same axis. Namely, it is not that the Reynolds stress is insensitive to the orientation of the axes, but that all the axes are very similar.

6.2 Principal Axes

As discussed before, the $\overline{u'v'}$ component of the Reynolds stress will be zero for certain choices of axis orientation. Specifically, there will be four angles, one in each quadrant, where the $\overline{u'v'}$ component goes to zero. This set of axes where $\overline{u'v'} = 0$ will be called the principal axes. Thus one will never have to rotate more than $45°$ degrees, either clockwise or counterclockwise, to find a principal axis. There is some subjectivity in the choice of axis that one uses to calculate the Reynolds stresses. Hopefully, one will find that the angle one chooses to use is not close to the principal axis. Figures 38 to 40 show the absolute value of the angle between the chosen axis and the one at which the $\overline{u'v'}$ component goes to zero (i.e. closest principal axis). Here, I have plotted the absolute value since we are not really concerned with whether it is to the right or left of the given axis. The angles have also been rounded down to the nearest $5°$ for clarity.

We can see that the behaviour between the three moorings is quite different. The 1999 North mooring (figure 40) is the worst, with large segments of the data $< 5°$ from the axis at which $\overline{u'v'} = 0$. The 1999 South mooring (figure 38) is better, and the 1999 East mooring (figure 39), which we fortuitously use in most of our calculations, is often significantly different from the axis at which $\overline{u'v'} = 0$.

Because the angle between the chosen axis and the nearest principal axis depends on the measured $\overline{u'v'}$ Reynolds stress (see equation 72), we might expect that, as a first guess, regions of large $\overline{u'v'}$ correspond to angles that are well away

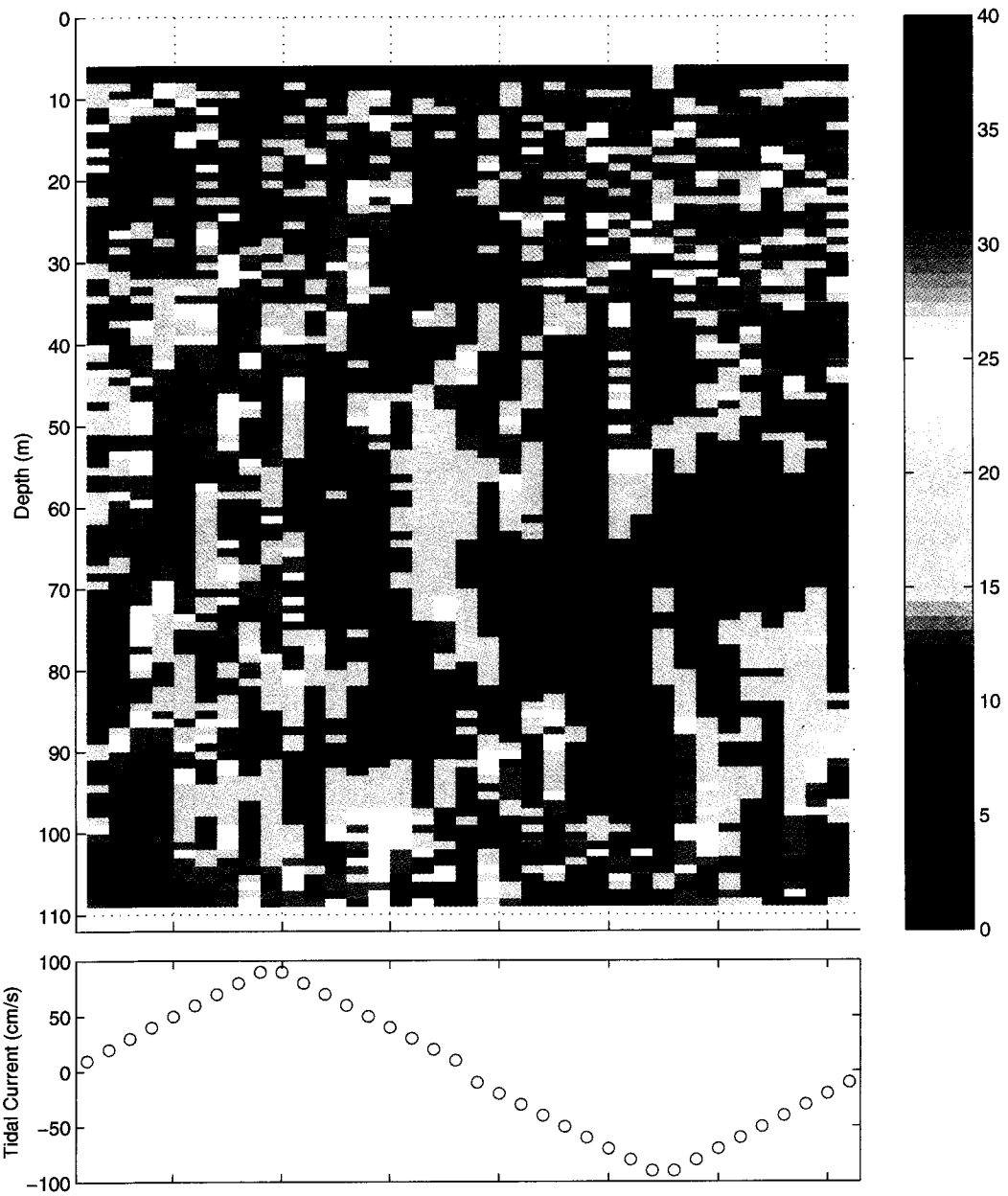

Figure 38: The absolute value of the angle (in degrees) between the chosen axis and the one where $\overline{u'v'} = 0$, as a function of depth and tidal current for the 1999 ADCP South mooring. The small plot at the bottom shows the corresponding tidal current. Angles are rounded down to the nearest $5°$.

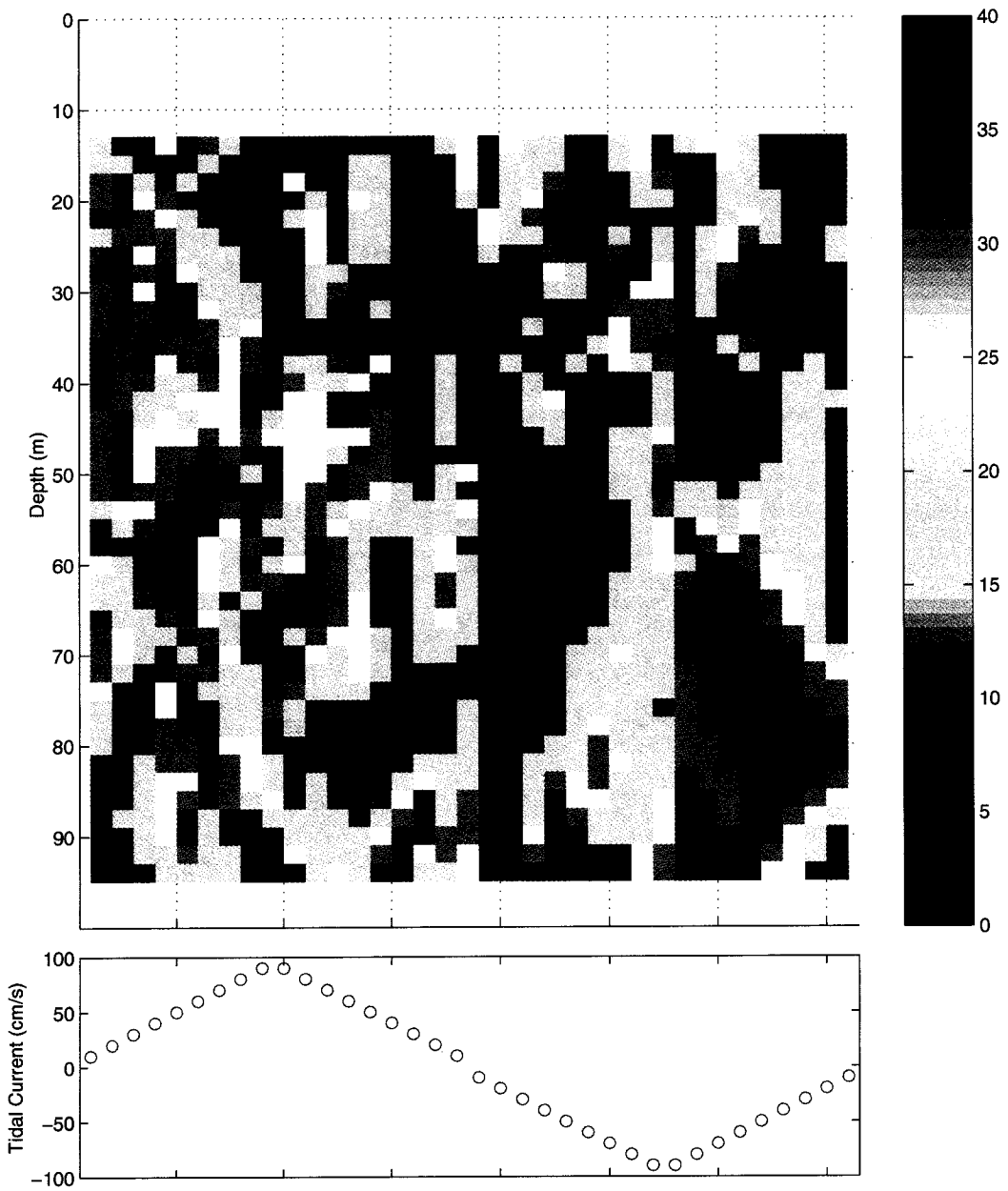

Figure 39: As in figure 38, but for the 1999 ADCP East mooring.

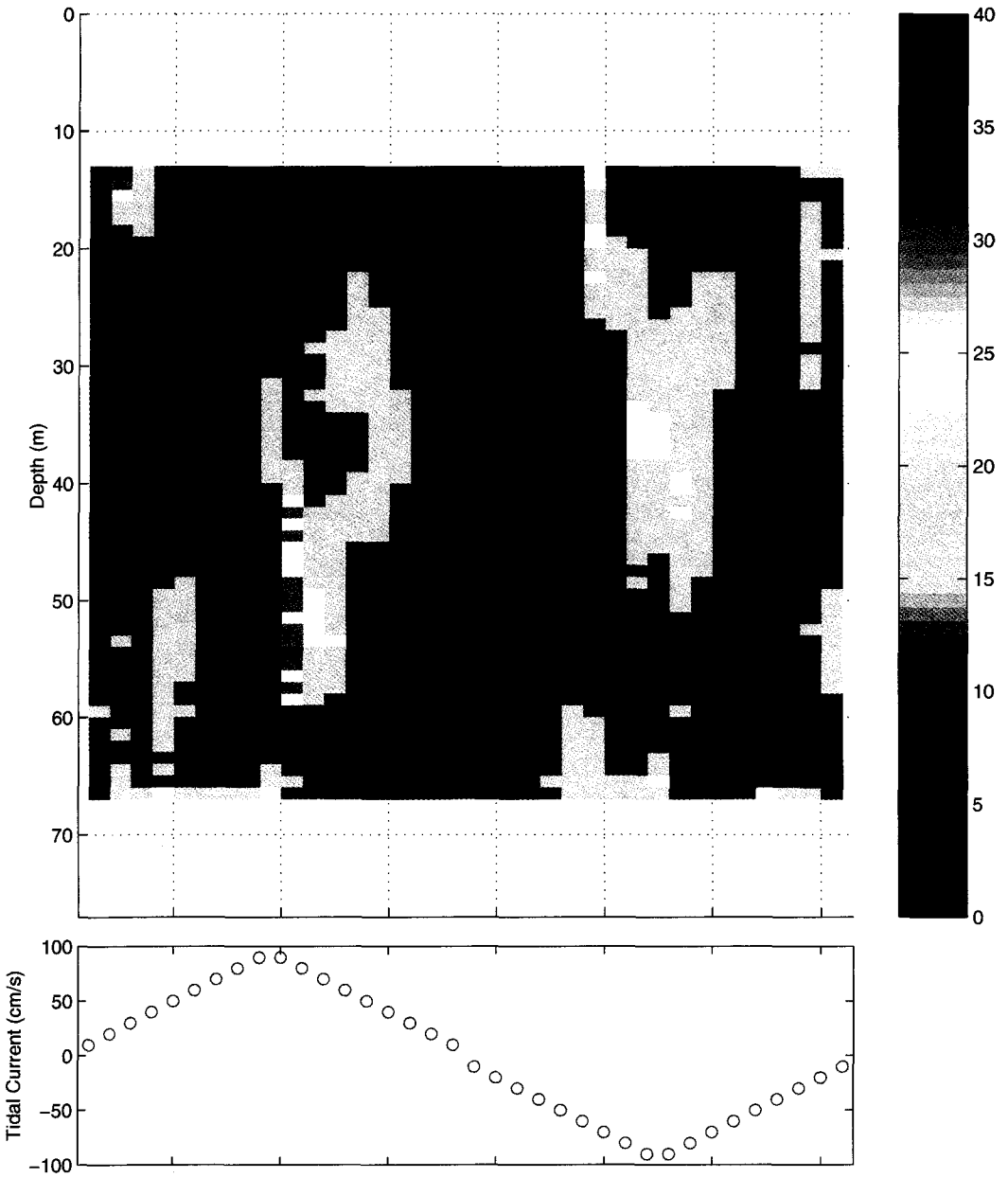

Figure 40: As in figure 38, but for the 1999 ADCP North mooring.

from zero. This is often the case. For instance, the two regions in figure 40 where the 1999 North mooring shows large angles between the chosen and principal axes, correspond to regions of relatively large $\overline{u'v'}$ Reynolds stress (refer to figures 31 and 32). Similar matches can often be found in the data from the 1999 East and South moorings as well.

Intuitively, I expect that an angle greater than 10° between the chosen axis and the closest principal axis is an indication of a believable signal. The difference between the chosen axis, an axis based upon isobaths, and an M_2 major axis is usually less than 10°. Thus, if the angle is greater than 10° one could expect that the $\overline{u'v'}$ Reynolds stress is not overly sensitive to the subjective choice of axis.

6.3 Reynolds Stress Scaling

Before proceeding with a parameterization for the Reynolds stress, it is useful to first ask if the Reynolds stress terms in the momentum equation are significant. The x-momentum equation is

$$\frac{\partial U}{\partial t} + U\frac{\partial U}{\partial x} + V\frac{\partial U}{\partial y} + W\frac{\partial U}{\partial z} - fV = -\frac{1}{\rho_0}\frac{\partial P}{\partial x} - \frac{\partial \overline{u'u'}}{\partial x} - \frac{\partial \overline{u'v'}}{\partial y} - \frac{\partial \overline{u'w'}}{\partial z}.$$

The magnitude of each of these terms can be estimated for a mean flow that represents the tide. It is important to note that an estimate based upon the estuarine flow as a mean might have a different balance of forces, since time and space scales are different and the Reynolds stresses average over a larger set of processes. For the tides we will use the following estimates: $\partial U/\partial t = (2 \times 0.8\,m/s)/20000\,s$, $U\,\partial U/\partial x = (0.8\,m/s)^2/100\,km$, $V\partial U/\partial y = (0.03\,m/s \times 0.20\,m/s)/800\,m$, $W\partial U/\partial z = (0.001\,m/s \times 0.20\,m/s)/30m$, $fV = (10^{-4}s^{-1} \times 0.03\,m/s)$,

$1/\rho_0 \partial P/\partial x = (1m \times 10\,m/s^2)/100\,km$, $\partial\overline{u'u'}/\partial x = (0.01\,m^2/s^2)/100km$, $\partial\overline{u'v'}/\partial y = (0.002\,m^2/s^2)/800\,m$, $\partial\overline{u'w'}/\partial z = (0.001\,m^2/s^2)/50\,m$. I have some difficulty in setting the spatial scale for $\partial/\partial x$ since there is not much information about variations in that direction. I have chosen 100 km, which means that there would be an order one change over the length of Juan de Fuca Strait. It is not clear that the scale of variation of the mean flow in the x-direction (in $U\partial U/\partial x$) needs to be the same as the scale of variation of the Reynolds stress in the x-direction (in $\partial\overline{u'u'}/\partial x$). Due to lack of information I have set them both to be the same here, even though I suspect that the scale of variation of the Reynolds stress could be significantly less than that of the mean flow. The vertical Reynolds stress divergence term is an upper bound, derived from a daily average during neap tide [*Ott,* 2000]. These scalings gives the following values (normalized by the pressure term)

$$(0.8) + (0.06) + (0.07) + (0.07) + (0.03) = (1) + (10^{-3}) + (0.03) + (< 0.2).$$

The main balance is therefore between the time variation and the pressure gradient, possibly with an important contribution from the vertical divergence of the $\overline{u'w'}$ Reynolds stress. The estimate for $\partial\overline{u'w'}/\partial z$ is an upper bound for this stress divergence, and represents the value which *Ott* [2000] found in the central water column inside the interior Ekman layers during neap tides. Values outside this region and period of the tide are an order of magnitude smaller. Therefore, I don't think that the value of the vertical divergence of the Reynolds stress used above is truly representative. Similarly, I believe that the term $\partial\overline{u'u'}/\partial x$ is unreasonably small based upon the spatial scale of $100\,km$. It is much more likely that all the Reynolds stress terms are similar in magnitude, at about $2 - 3\%$ of the pressure

term.

The Reynolds stress divergence terms are smaller than, but roughly the same magnitude as the advective terms, and are only a few percent of the major forcing term (sea level height). They are not likely to influence the zeroth order solution, but they may introduce small corrections. In particular, a lateral Reynolds stress may influence the phase of the tide. If one could simplify the momentum equation to

$$\frac{\partial u}{\partial t} + \lambda u = \exp^{-i\omega t},$$

where λu is the stress and the exponential represents the pressure forcing, then one might expect a phase lag from the Reynolds stress equivalent to $1/(u\omega)\ \partial\overline{u'v'}/\partial y$. This gives about $7.5°$ using an average value of the stress divergence, the rms velocity, and the M_2 frequency. The observed phase shift in the M_2 component of the tide between the 1999 South and East moorings is about $10°$. Although small the Reynolds stress divergence is non-negligible and thus worthy of interest.

6.4 Eddy Viscosity

Figure 41 shows a scatter plot of lateral Reynolds stress ($\overline{u'v'}$, from the East mooring) versus shear (calculated between the North and South moorings). The eddy viscosity in this phase space is the negative of the slope. There are three groups of dots in figure 41, which correspond to stresses which are significantly different from 0 at successive confidence limits of 50%, 80%, and 95%. Thus all the dots are at least significant to a 50% confidence interval, the red and green are significant to at least an 80% limit and the green are all above 95%. Although we want to have a certain level of statistical confidence in the data, one finds that by

increasing the confidence limit what one does is preferentially select regions of particularly large Reynolds stress. While these regions are clearly significant they are not representative of the mean, and so the derived eddy viscosity would only be useful for restricted times and depths. We can probably say that by including all the data, with no error checking, we get a lower bound for the eddy viscosity. The value derived from all the data is $3.9\,m^2/s$, with a correlation coefficient between shear and stress of -0.41. I would therefore say that a mean eddy viscosity has a value of $4-8\,m^2/s$ and can attain intermittent values of $15-20\,m^2/s$.

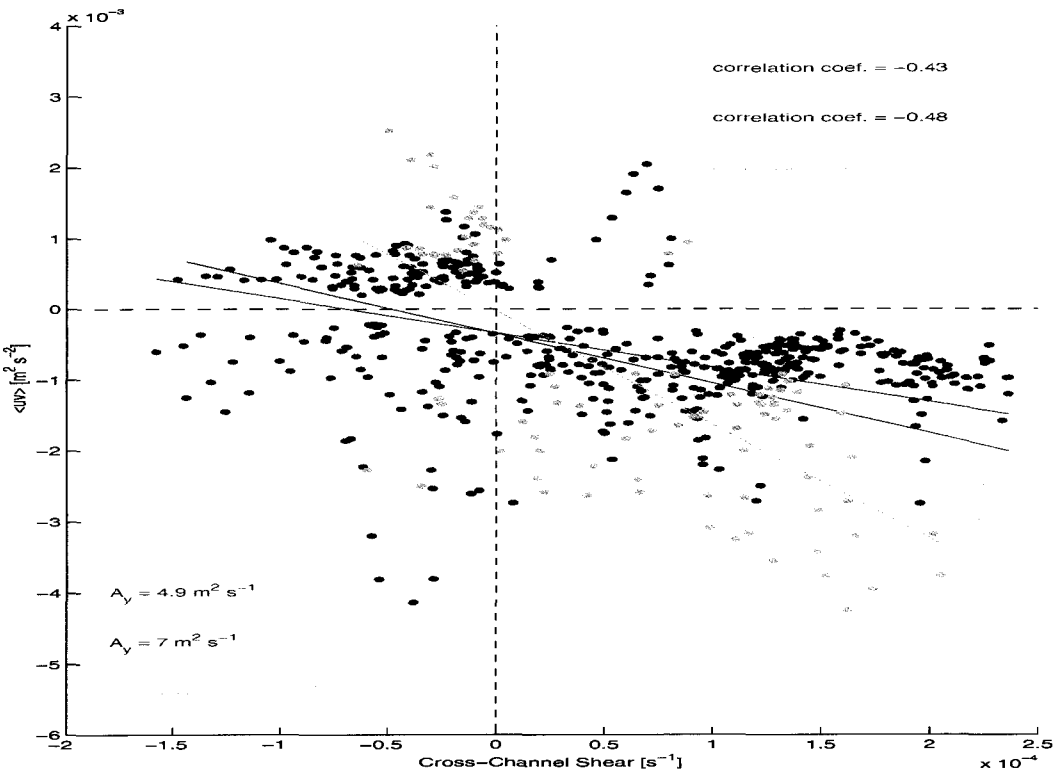

Figure 41: A scatter plot of Reynolds stress (East mooring) versus shear (North-South Mooring). The colours represent successively more stringent choices of statistical confidence (Blue 50%, Red 80%, Green 95%). The lines are least-square regressions to the different groups.

Modelling the Reynolds stress with a least squares regression line, passing through zero, corresponds to a constant eddy viscosity assumption. We can see that although a line is not hopeless at describing the scatter plot in figure 41, it is hardly a satisfying fit to the data. It is also obvious that a log layer parameterization would not be a good fit to the data, since it would indicate that the Reynolds stress depends quadratically on shear (of course we expect our moorings to be outside the horizontal log layer). Thus it seems unlikely that the $A_H \propto U$, since this would imply that the $\overline{u'v'} \propto -|u|u$, which is not apparent in figure 41. It is possible that we are seeing momentum transfer by a number of different processes (e.g. internal waves, vortical modes and turbulence) and that expecting a single parameterization to capture all the variability is unrealistic. However, the data are largely from outside the top and bottom boundary layers, and the internal Ekman layers [*Ott*, 2000] intersect the bottom near the region of our outermost mooring, so they are not playing a role either.

The Reynolds stress measured at other moorings is difficult to use since we do not have appropriate shears with which to match. The South mooring Reynolds stress shows only weak correlation (-0.16) with the shear measured between the East and South moorings. The North mooring is somewhat more useful since it is bounded to the North by a slope where the velocity must vanish. Hence it shows reasonable correlations with the North - East mooring shear (-0.45), and also with the North velocity (-0.56) (ie. the shear determined between the North mooring and the sidewall). Values calculated for the North mooring Reynolds stress using a no-slip sidewall to calculate the shear give mean eddy viscosities of $3 - 6\, m^2/s$. It would be preferable to have a formula for the eddy viscosity instead of just a number. I will study this further in the Discussion chapter.

6.5 Spring-Neap Variability

The spring-neap tidal cycle modulates the dynamics of the entire estuary, so we might expect to see a signal in the Reynolds stress. Figures 42 and 43 show the lateral Reynolds stress ($\overline{u'v'}$) calculated during a 4-day time window centered on neap tide. We only plot the Reynolds stress for speeds $\leq$ $0.5\,m/s$, since the larger velocities predominantly exist during spring tide. For comparison figures 44 and 45 show the same calculation for a 4-day window surrounding spring tide.

There are clear differences between the spring and neap tide Reynolds stresses (for the same value of the tidal current) and, much more noticeably, strong differences in the tidal shear. The spring tide Reynolds stresses are generally larger than the neap tide values, and do not have the same vertical structure in some instances. This is not entirely unexpected since a $+50\,cm/s$ current at spring tide is still in the process of accelerating toward peak flood, while at neap it may represent the peak flood. Thus current velocity does not map onto the same tidal phase during spring as it would during neap. However I would expect that slack tides occur at the same phase, regardless of spring or neap tide, but there is still enhanced tidal shear.

Another reason for the increased shear during spring tides is that the magnitude of the tidal oscillation (flood-to-ebb) is greater, but the tidal phase lag between the coast and the southern mooring is roughly unchanged. The shear will roughly go like

$$\frac{\partial U}{\partial y} \propto U_{max}\cos(\omega_{M2}t) - U_{max}\cos(\omega_{M2}t - \phi), \tag{83}$$

where ϕ is the phase difference, U_{max} is the peak velocity (which is a slowly vary-

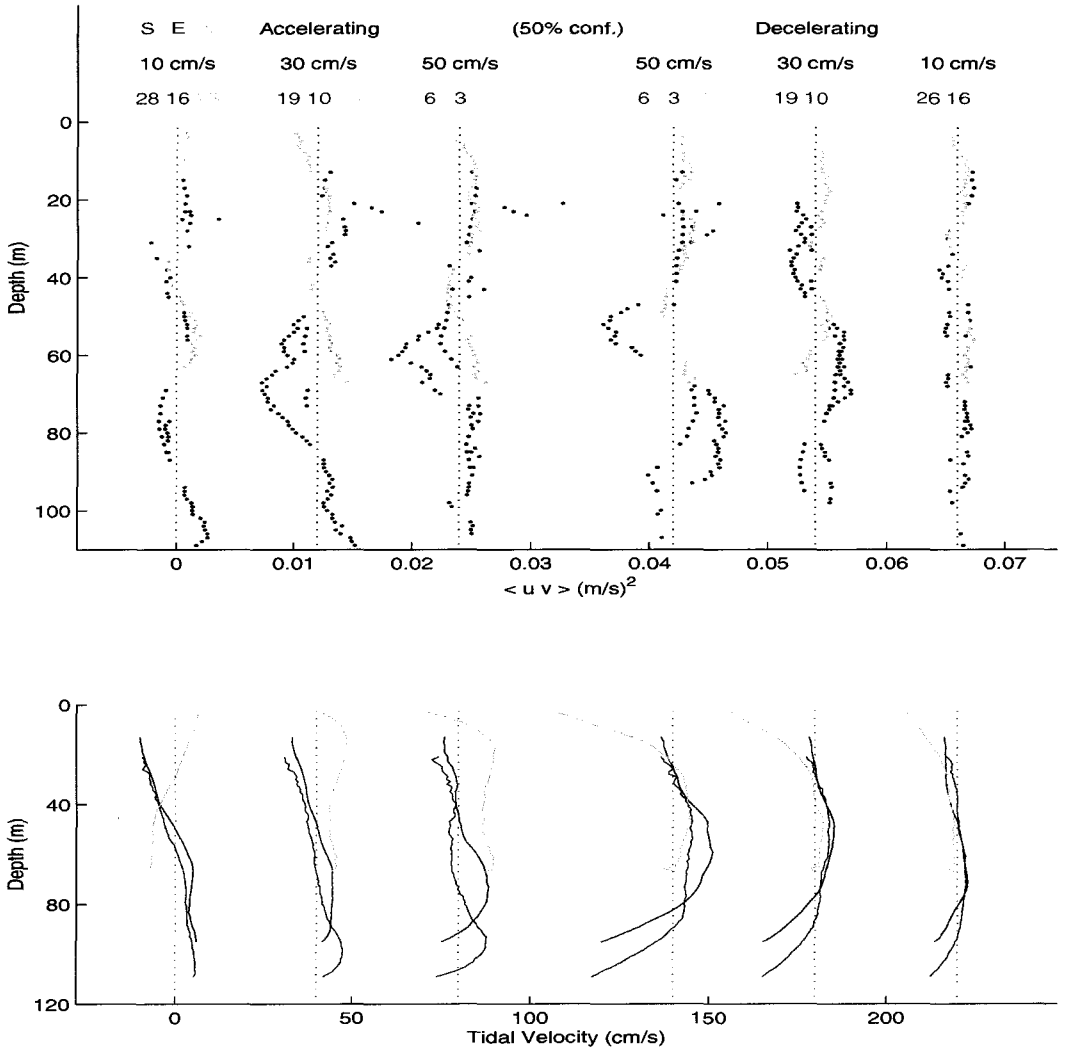

Figure 42: The $\overline{u'v'}$ Reynolds stress during flood, calculated for a 4-day window around neap tide. Colour as in figure 31.

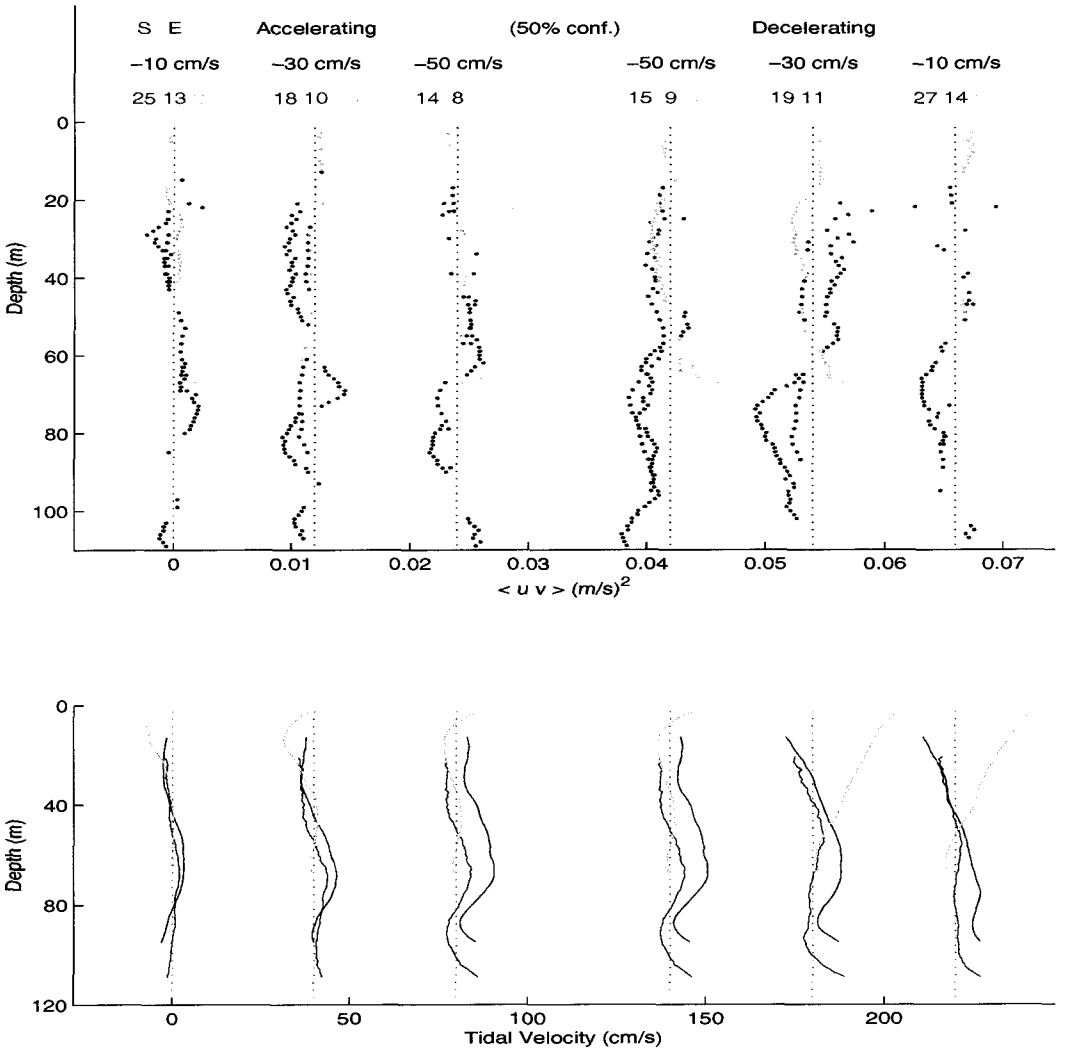

Figure 43: The $\overline{u'v'}$ Reynolds stress during ebb for a 4-day window around neap tide.

ing function of time) and we fudge slightly by assuming only a single frequency component. Thus the shear depends directly on the peak velocity. There is a slight gloss over the fact that we are comparing different values of $\omega_{M2}t$ between neap and spring, but this is not a large correction.

Although not shown, there are also differences in the diagonal Reynolds components ($\overline{u'u'}$ and $\overline{v'v'}$). In particular the auto-correlated stresses seem to increase during spring tide near the surface and also slightly near the bottom, but decrease within the center of the water column (as compared to neap tide). The excess variability near the surface could be attributed to increased eddy activity, caused by the larger tidal velocities generating more active eddies. The decrease in the central water column might be attributable to the changing stratification altering the modal structure of the low mode internal waves. For example, the increased stratification at neap tide might promote more first and/or third mode waves which have large velocity signatures at mid-depth.

If a simple eddy viscosity parameterization holds true, than the increase in tidal shear will lead to a proportional increase in the lateral Reynolds stress ($\overline{u'v'}$). Figure 46 shows a shear vs. lateral Reynolds stress scatter plot for spring tide (dots and solid lines) and neap tide (circles and dotted lines). First, the two are obviously in different regimes. The spring tide values of eddy viscosity and correlation coefficient are not substantially different from the average values calculated above. The neap tide values are quite radically different and for the most part are only poorly correlated with the shear. Note that the 95% confidence interval for neap tide only entails 5 ensembles , so the eddy viscosity and correlation coefficient are largely meaningless.

I would also consider that the value of eddy viscosity derived for the 50%

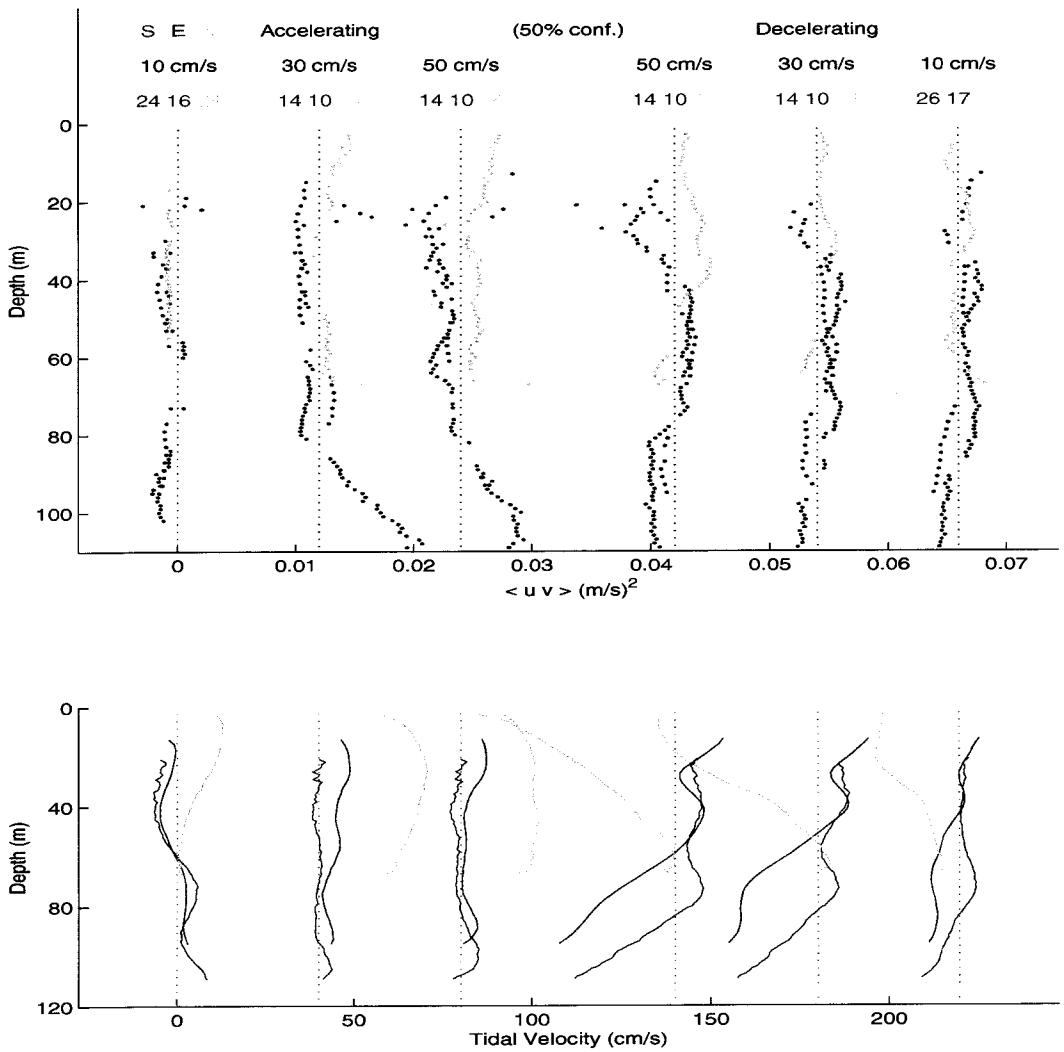

Figure 44: The $\overline{u'v'}$ Reynolds stress during flood for a 4-day window around spring tide.

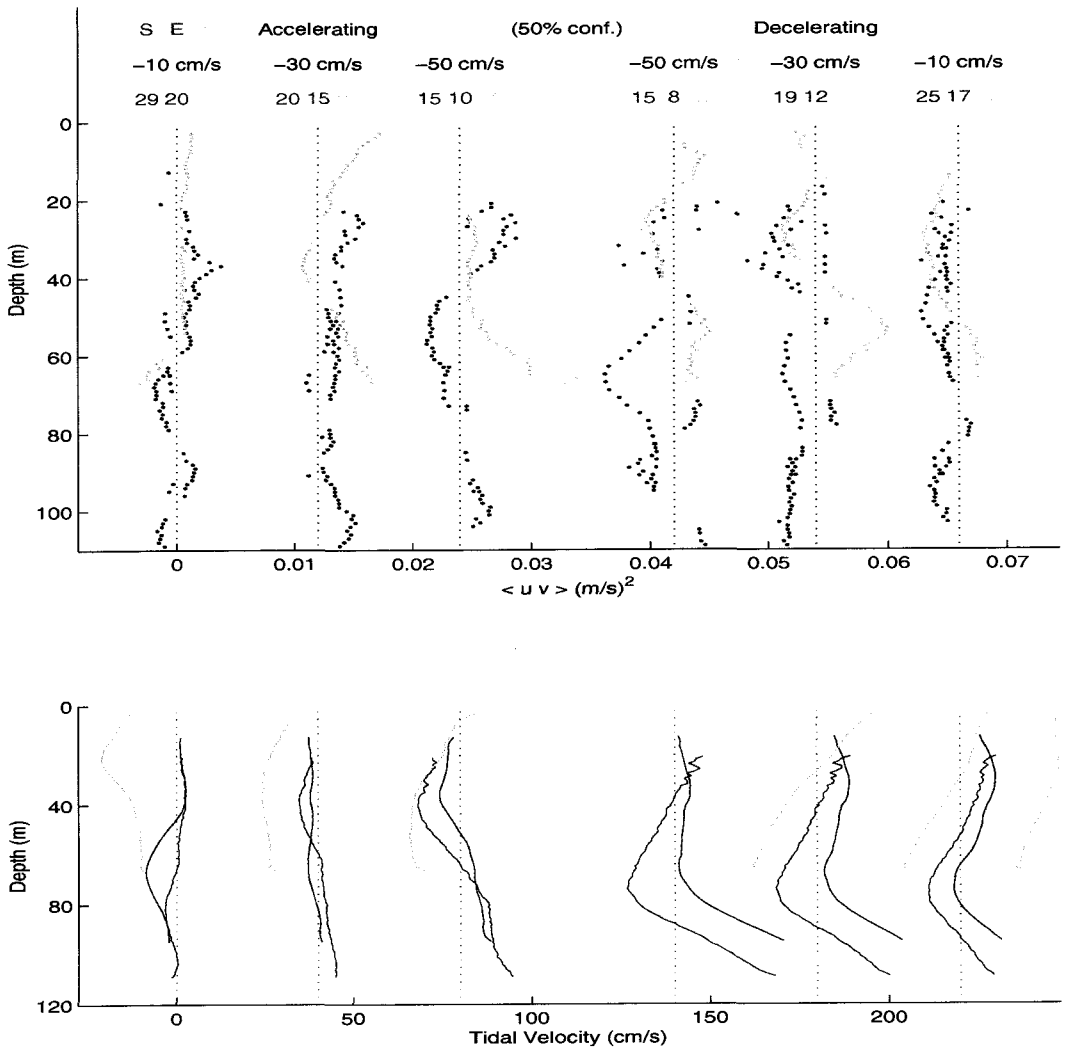

Figure 45: The $\overline{u'v'}$ Reynolds stress during ebb for a 4-day window around spring tide.

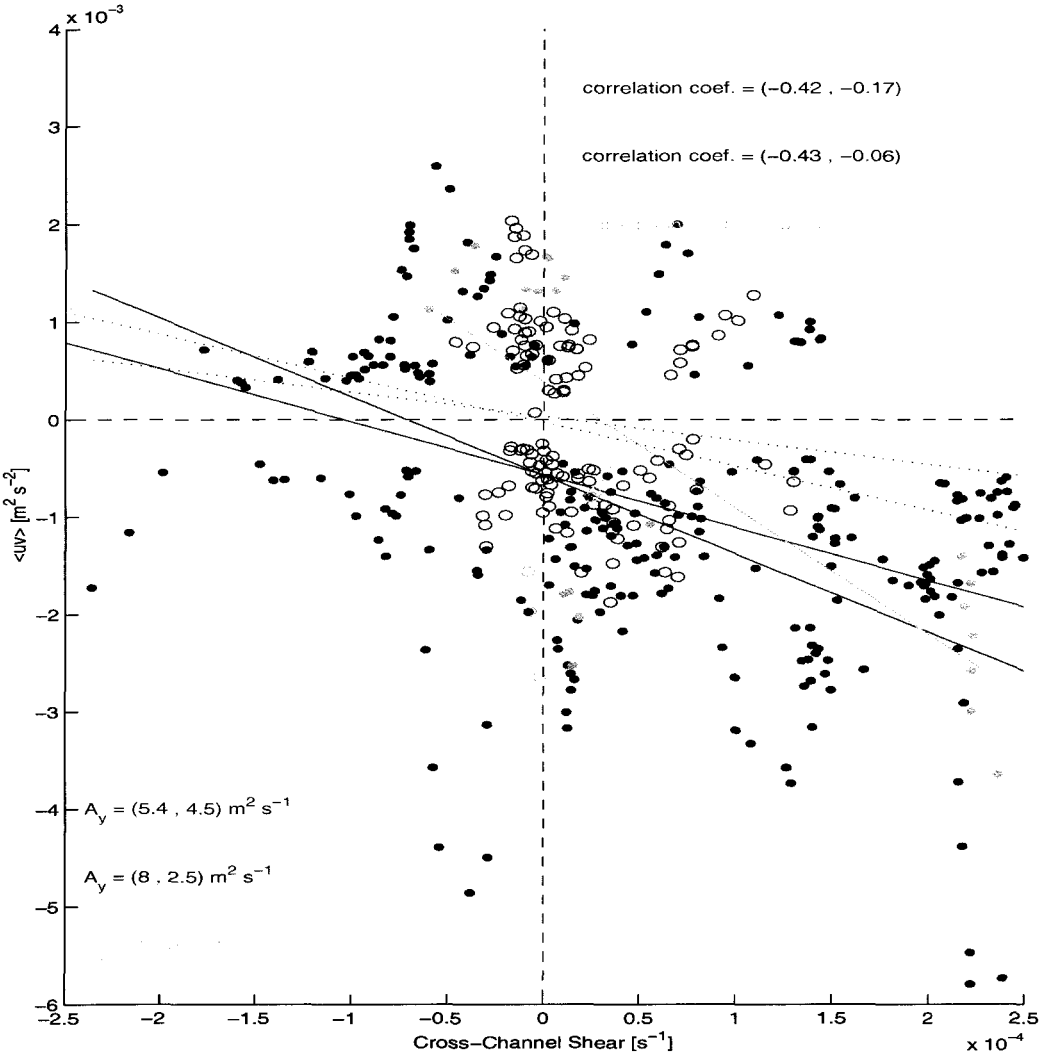

Figure 46: A scatter-plot of tidal shear ($\partial U/\partial y$) vs. Reynolds stress ($\overline{u'v'}$) for spring tide (dots and solid lines) and neap tide (circles and dotted lines). Colours and lines are as in figure 41. Numbers pairs refer to (spring, neap) values.

significance neap tide data (ie. $4.5\,m^2/s$) is only similar to the spring tide and average values by coincidence. The least-square regression line could hardly be said to adequately capture the data.

I hypothesize that during neap tide the large-scale horizontal shear is reduced and thus the small-scale shear, which is below the resolution of our moorings, may account for a significant part of the total horizontal shear. During spring tide the local shear is dominated by the large-scales, which our mooring array does a passable job of measuring. Thus, it is not that shear and lateral Reynolds stress are decorrelated during neap tides, but that the shear is not being adequately resolved during neap tides.

6.6 Reynolds Stresses Acting on the Estuarine Mean Flow

We have been discussing the Reynolds stresses calculated about a mean flow that consists of the tides. In this subsection, we will take the mean flow to be the estuarine circulation, which I will assume is slowly varying on time scales $>$ 1 *cpd*. This means that the tides are now part of the fluctuation side of the equation, and most likely the dominant part of that signal.

A four day (actually an $8 \times M_2$ period) block centered on each day is taken, and assigned an axis based upon the mean current during that time interval. The 1999 mooring array is located entirely within the out-going layer, so I could have chosen a depth-averaged axis and obtained similar results, but for consistency with the previous sections a depth-dependent axis is used. Before considering the Reynolds stresses, we shall first examine the mean estuarine flow.

It is important to know how the bottom boundary layer behaves on this long time scale. In a tidally-unmodulated flow, one would expect Ekman dynamics in

the lower layer. An Ekman layer, moving water down-slope for instance, would also need to be balanced by a secondary circulation return flow in the interior. Then the Coriolis force acting on this secondary circulation would tend to decelerate the mean along-slope flow. There is also the question of arrested Ekman layer dynamics [*Garrett et al.,* 1993], although in this case the surface pressure gradient should force flow down the slope [*Allen and Newberger*, 1998]. All of this becomes more complex in a tidal flow since the velocity reverses every six hours. The time-depth estuarine velocity recorded at the South mooring is plotted in figure 47.

One sees that the along-isobath estuarine flow is almost always negative (oriented seaward), except for a period near the beginning of the time record, and several times at mid-depth during the neap phase of the spring-neap cycle. Cross-isobath velocities are much more erratic although one often sees a shift to negative (down slope) velocities in the bottom 20m. This is different than along-slope velocities which tend toward zero in the bottom boundary layer, and is in the direction one would expect from Ekman dynamics. I should note that the depth-averaged cross-isobath current is not zero on these time scales, as one might expect in order to maintain sea level height. However, there are two reasons that this is problematic. First, the surface is not resolved, so one cannot calculate a true depth-average. Second, the mooring need not be representative of the mean flow everywhere along that isobath (ie the flow could be up-slope on average in some locations and down-slope on average in others). There is also the question of whether the mean flow contains the signature of relatively stationary eddies.

Assuming that the flow in the bottom boundary layer follows Ekman dynamics

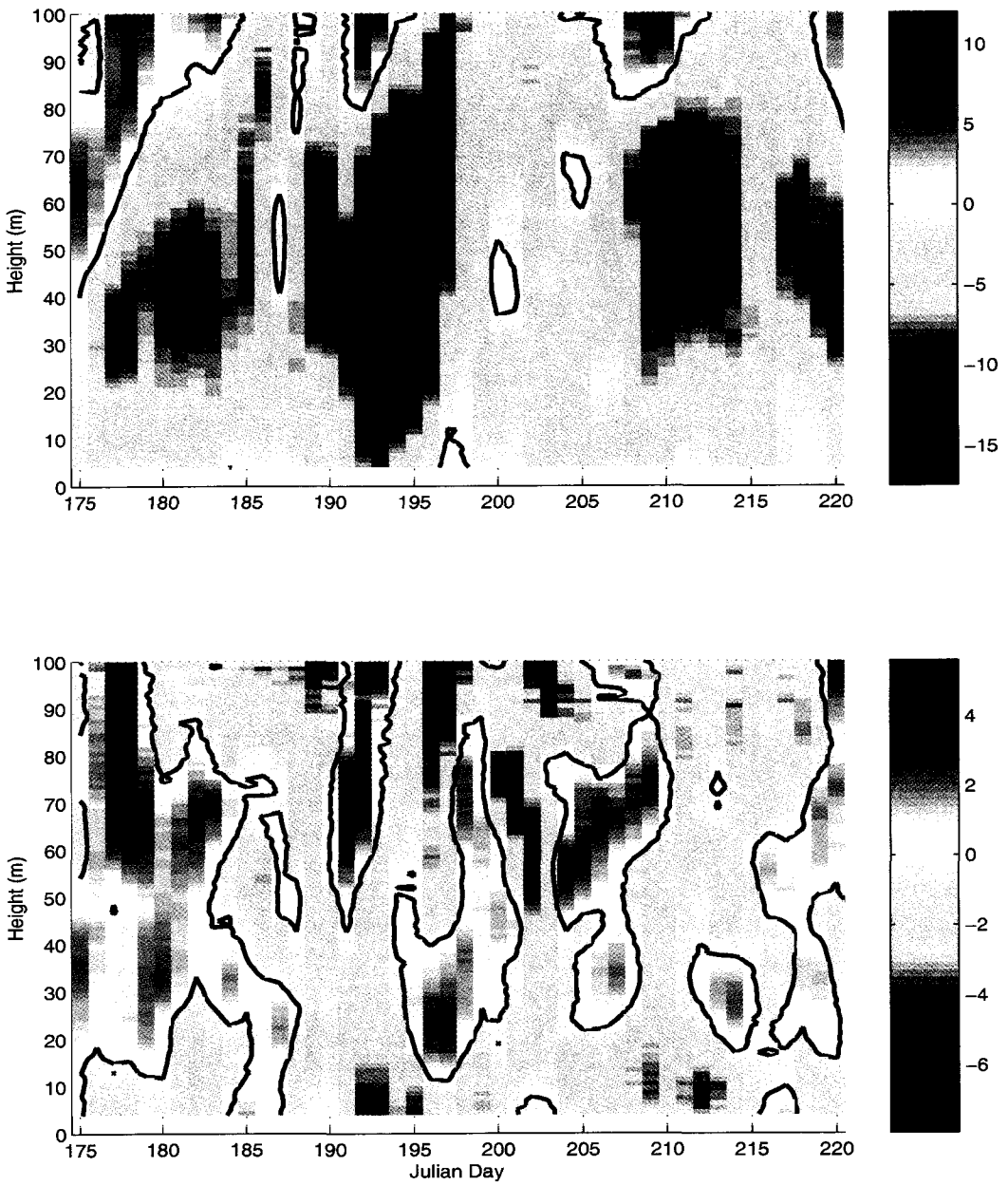

Figure 47: A depth-time plot of the along-isobath (top) and cross-isobath (bottom) estuarine velocity (in cm/s), calculated as a 4 M_2 period running mean for the South mooring. The black line is the zero velocity contour.

then one can write

$$C_D\, U_{est}\, |U_{rms}| = f\, v_{bbl}\, H_{bbl}, \tag{84}$$

where C_D is a drag coefficient, U_{est} is a velocity representing the mean estuarine along channel flow, U_{rms} is an rms along-channel velocity, f is the Coriolis parameter, v_{bbl} is the cross-isobath flow in the bottom boundary layer, and H_{bbl} is the thickness of the bottom boundary layer. This allows one to estimate the average drag coefficient as

$$C_D = \frac{(1.1 \times 10^{-4}\, s^{-1})\ (-0.02\, ms^{-1})\ (20\, m)}{(-0.10\, ms^{-1})\ |0.45\, ms^{-1}|} = 1.0 \times 10^{-3}.$$

This value is quite a bit smaller than the values determined from fits to the log layer by *Ott* [2000] in a flat section of central Juan de Fuca Strait ($2.6 - 3.9 \times 10^{-3}$). It is also interesting to note that a $0.02\, m/s$ down-slope flow in the bottom boundary layer of thickness $20\, m$ implies, assuming conservation of volume, a $0.004\, m/s$ return flow in the rest of the water column.

Taking the x-axis to coincide with the estuarine velocity during a given four day (actually 8 M_2 periods) block, the Reynolds stress is calculated. Since there is a spectral gap between the dominant frequencies of the fluctuations that produce the Reynolds stress (tidal at $1 - 2\, cpd$) and the mean flow (estuarine at $< 0.5\, cpd$) ensemble averaging is not needed. The resulting lateral Reynolds stresses at the three moorings are shown in figure 48.

The mean-flow Reynolds stresses are much larger than the Reynolds stresses calculated earlier (by a factor of at least 30) since they now average over a larger subset of processes, most notably the tides. There is also a strong visual correlation between the behaviour of the Reynolds stress at the different moorings,

particularly East and North. The stresses are predominantly positive, away from the bottom, in the North and East moorings, whereas the South mooring is much more varied in time and depth. A positive stress would tend to imply a negative shear ($\partial U/\partial y$) under the assumption of a positive eddy viscosity. This does not agree with a simple parabolic concept of the outflow distribution.

The strongest positive Reynolds stresses at the North and East moorings correspond to periods around spring tide (spring tide is on days 182, 196, 210 and 224) and the regions of negative, or weakly positive, $\overline{u'v'}$ stress correspond to neap tide (days 175, 189, 203 and 217). The South mooring does not share the strong spring-neap variability of the East and North moorings. Since the Reynolds stress fluctuations are tidally dominated, I would expect a strong spring-neap cycle in all three of the mooring's $\overline{u'v'}$ stresses. It is not at first clear whether the spring-neap modulation is due to changes in the fluctuations, or due to changes in the relative orientation of the estuarine mean and the dominant tidal flow fluctuations, or some combination of the two.

To elucidate this point a scatter plot of the measured lateral Reynolds stress at each of the three moorings versus the angle of orientation of the estuarine mean flow is shown in figure 49. It is immediately clear that most of the variation in the signal can be attributed to the orientation of the estuarine mean flow. Thus the tides flow predominantly along isobaths, as seen by the zero crossings at 0 and π radians, and the lateral Reynolds stress is simply a dot product of the tides onto the estuarine flow, with an amplitude that is modulated by the spring-neap cycle. However, the important physical consideration is not the lateral Reynolds stress but its divergence.

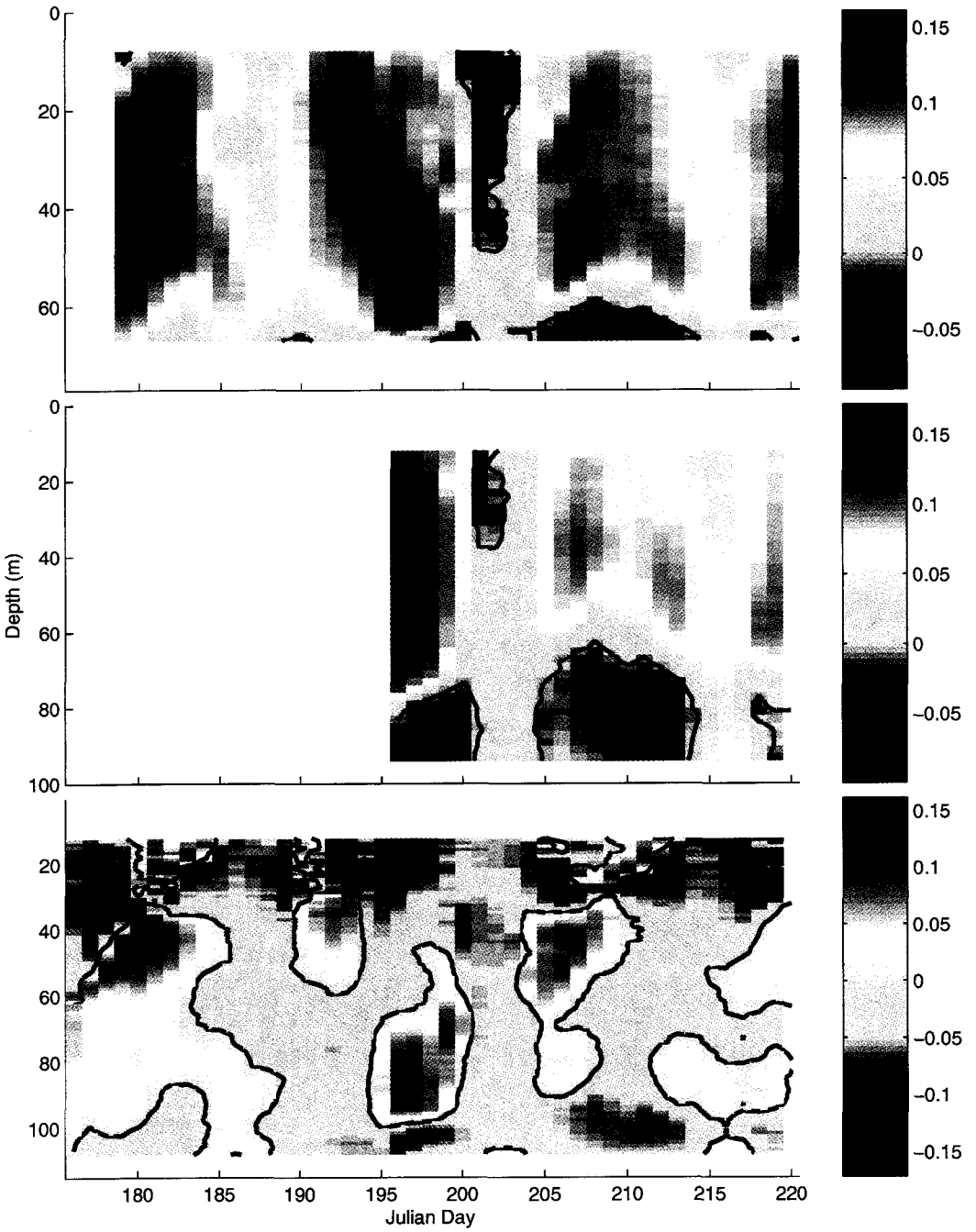

Figure 48: The lateral Reynolds stress ($\overline{u'v'}$) calculated about the estuarine mean flow, for the North (top), East (middle) and South (bottom panel) moorings. The zero contour is drawn in black.

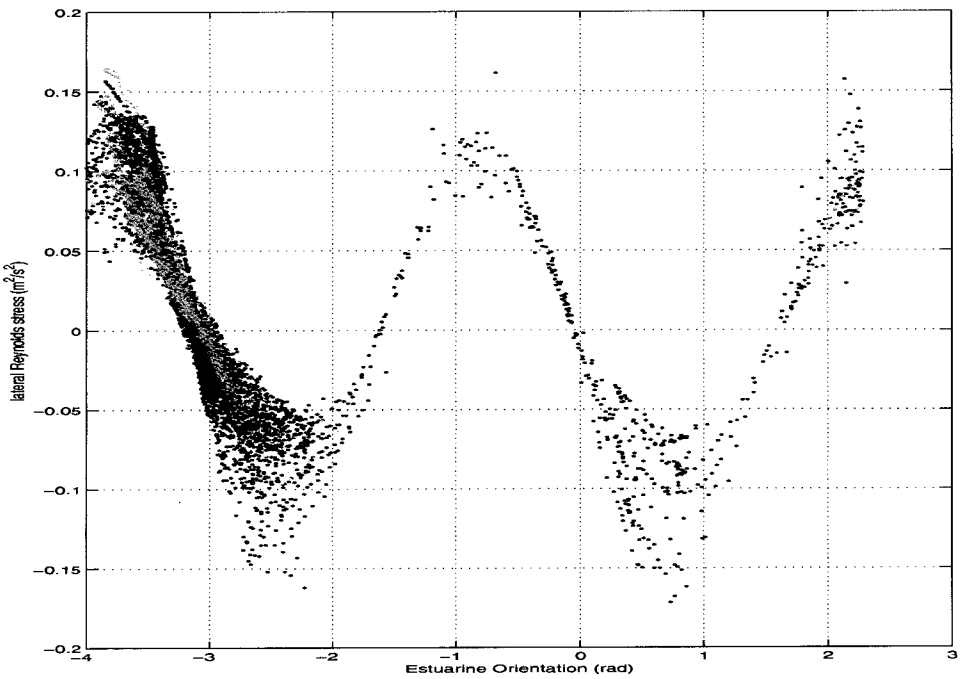

Figure 49: A scatter-plot of the angle of the estuarine mean flow ($\pm\pi$ radians are aligned along isobaths) versus the measured lateral Reynolds stress ($\overline{u'v'}$) for the North (red), East (green) and South (black) moorings.

7 Differentiating Internal Waves and Vortical Modes

The consistency relations are an attempt to explain the observed Reynolds stresses and to link them to particular processes. The consistency relations are complicated by two factors: the Doppler shift and the boundaries of Juan de Fuca Strait. We shall therefore start with the relation between vertical velocity and isopycnal displacement, which is independent of type of motion, and of the existence of boundaries. This allows me to diagnose only the Doppler shift effect. We then proceed on to the point consistency relations (CCW/CW and PE/HKE) and attempt to describe the observations. Finally, we address the additional constraints imposed by vorticity and divergence.

7.1 Doppler Shift Effects

7.1.1 Vertical Velocity versus Isopycnal Displacement

The Doppler shift will have some effect on all of the measurements, but to understand its behaviour I wish to start with a relation that is independent of the type of motion or the presence of boundaries. Therefore, we shall first consider the relation between vertical velocity and isopycnal displacement discussed in 3.4.1. Figure 50 shows the scaled isopycnal displacement spectra ($\omega^2 S_\eta(\omega)$) versus the vertical velocity spectrum ($S_w(\omega)$). There are two lines for most of the spectra. The two isopycnal spectra represent results from two different temperature chains that flanked the central ADCP (figure 21). The two red velocity spectra represent bins that are above and below the mean depth of the isopycnal (this attempts to account for the fact that the velocity is fixed to a given depth, but the isopycnal height can wander over a range of depths, especially between the two temperature

chain moorings).

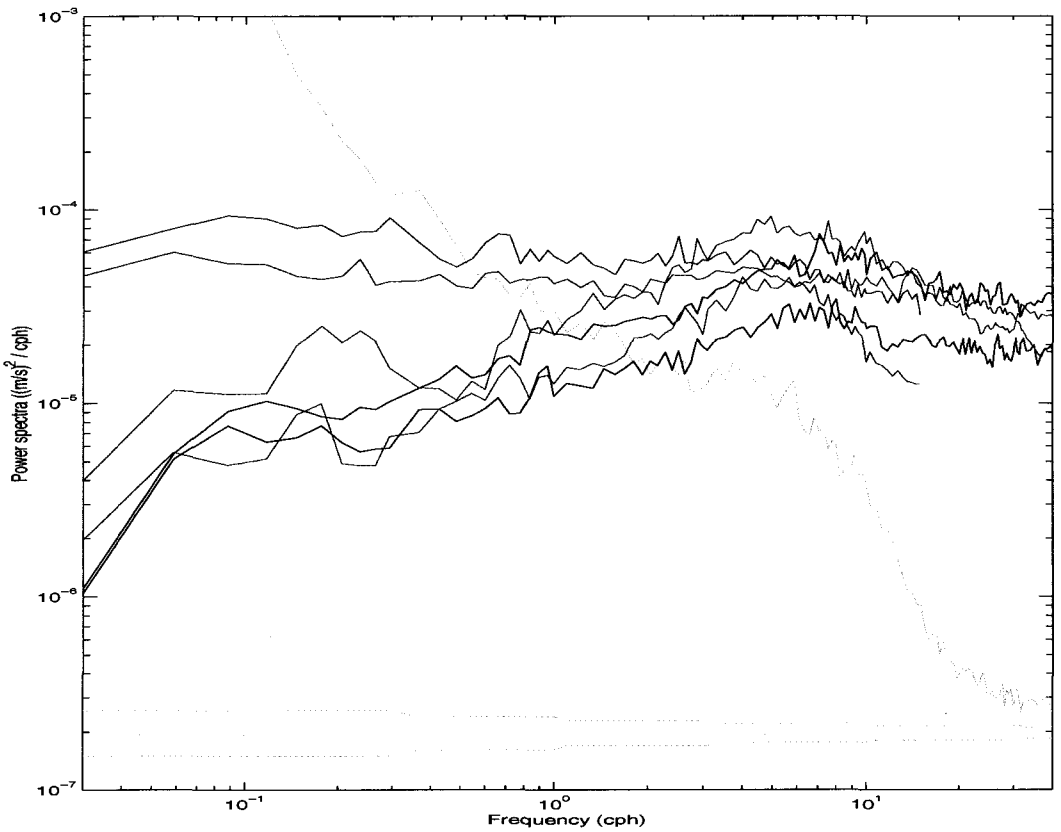

Figure 50: The vertical velocity spectra (red:99S, green:98N) and the scaled isopycnal displacement spectrum (blue:99N and 99S, black:98NE and 98NW). The two isopycnal spectra represent the different moorings, the two red velocity spectra from 1999 represent depth bins that flank the average isopycnal depth. The green lines at the bottom of the figure are the error bar.

If there was no Doppler shift then we would expect that the red and blue curves should overlie one another (similarly the green and black curves). One sees that the vertical velocity spectrum and the scaled isopycnal displacement spectrum are in poor agreement for the 1998 data (green and black), but in considerably better agreement for the 1999 data (red and blue). I have strong suspicions that the 1998

vertical velocity is contaminated by the horizontal velocities, so we will ignore it in the future discussions.

There are a number of possible reasons why the spectra from 1999 (red and blue) do not agree. The first is that the vertical velocity spectrum (red) is unreliable due to contamination from the horizontal velocities, as we suspect in 1998 (green). This is most likely to be true at low frequencies where the vertical velocity signal is very much weaker than the horizontal velocities. This is true for internal waves, but should be reasonably true for any type of motion as well. If one assumes that the vertical velocity signal at low frequencies is entirely due to contamination from the horizontal velocities, then one gets a measure of the uncertainty in pitch and roll. In the region $\omega < 0.1$ cph the horizontal velocity spectra are 10^4 times greater then the vertical velocity spectrum (for 1999 data). Since the pitch and roll are independent of frequency, this implies that at high frequency the contamination of the vertical velocity spectrum could be no larger than $1/10^4$ of the horizontal velocity spectra. However, the observed vertical velocity spectrum exceeds that associated with contamination from horizontal velocity. I therefore assume that the vertical velocity measurements in 1999 are an adequate representation of the true vertical velocity.

Alternatively the scaled isopycnal spectrum could be contaminated due to the mapping of temperature to density. The mapping may over-estimate the higher frequency motions, since the temperature to density scaling assumes that there is no salinity compensation on fast time scales. Namely, I am assuming that the T-S characteristics are fixed on all but very long time scales, which is unlikely to be true. But this assumption holds true for all frequencies less than the frequency used in the construction of the T-S mapping (1/4 cpd). The assumption of fixed

T-S properties on short time scales should be worst for the low frequency motions, where one might expect that there is more time to change the T-S properties. This would imply that the scaled isopycnal displacement spectrum should be even more blue than it is now. This does not help rectify the discrepancy. Therefore, I choose to believe that the spectra are unaffected by $T \rightarrow \rho$ mapping errors, at least for frequencies greater than $\omega > 0.1$ cph.

If we employ the simple argument from 3.4.1, then to the left of $\omega_c \approx 6$ cph in figure 50, where one sees that the vertical velocity spectrum is higher than the scaled isopycnal displacement spectrum, we would have $-2\omega_i < \tilde{U} \cdot \tilde{k} < 0$. Therefore the average wave in this region is propagating against the current, which is consistent with the idea of lee waves.

There is a large amount of averaging and assumptions that occur within the simple calculations in 3.4.1, but I interpret it to mean that on average $\tilde{U} \cdot \tilde{k} < 0$ for $\omega < \omega_c = 6$ cph. Now an internal wave will persist for a few tidal cycles, thus for any given wave we will have periods when $\tilde{U} \cdot \tilde{k}$ is positive and periods when $\tilde{U} \cdot \tilde{k}$ is negative. However, if the waves are being continually dissipated in some fashion, then the average over all waves will be weighted toward the newest ones. Thus if the majority of waves are being formed as lee waves by the tides, then we should see $\tilde{U} \cdot \tilde{k} < 0$ in the average.

Around the frequency of $\omega_c \approx 6$ cph the vertical velocity and scaled isopycnal displacement are in relative agreement. This would imply that within this frequency band one has either $\tilde{U} \cdot \tilde{k} = 0$ or $\tilde{U} \cdot \tilde{k} = -2\omega_i$. These are quite different results since the former implies that the Doppler shift is unimportant, while the latter implies that the Doppler shift is overwhelming but has fortuitously reached a magnitude such that $\omega = -\omega_i$. There is no clear way to distinguish which case

is true. In a simple constant U example, one could argue that $\tilde{U} \cdot \tilde{k} = 0$ implies that the waves must be veering in direction as a function of frequency, so that they are on average perpendicular to the mean flow at $\omega = \omega_c$. This would be a non-intuitive result. However, I can't make such a prediction in the complex environment in Juan de Fuca Strait.

Another explanation might be that the features observed at high frequency are longer lived, and so although they were formed as lee waves initially, the two spectra of waves propagating against and with the current are very similar.

However if one assumes that the simple scaling argument is useful then one can infer something about the magnitude of the Doppler shift. In the low frequency range, $O(0.1\,cph)$, I have $S_w(\omega) \approx 5\omega^2 S_\eta(\omega)$ which implies that $\omega \approx 0.4\,|\omega_i|$. If this could be interpreted as $\omega = 0.4\,\omega_i$ then the Doppler shift effect would not be too drastic, since it means that signals at a given observed frequency are dominated by intrinsic frequency motions that are only 2-3 times higher. However, if it means $\omega = -0.4\omega_i$ then the Doppler shift frequency is larger than the intrinsic frequency, even in this gross average, and so one would expect to have a very difficult time in interpreting the results.

7.1.2 Vertical Velocity as a Function of the Tide

An additional piece of data that points to the existence of lee wave generation is given by the vertical velocity data. For a given mooring, I can calculate spectra of the vertical velocity taken from particular segments of the tide (in a manner similar to the ensemble averaging used in the Reynolds stress calculation). The short segments used must necessarily restrict the resolvable minimum frequency. The vertical velocity spectrum from the 1999 ADCP moorings is shown as a function

of the mean tidal velocity in figure 51. The plot is for a velocity bin at $z \approx 40m$ height, but the result is fairly independent of the choice of bin. I should note that the vortical mode exhibits little vertical velocity, and so the features in the high frequency vertical velocity spectrum are due to internal waves.

Although there is noise in the data, it is apparent that at periods around slack tide there is an energy maximum centered around 4-6 cph. As the tidal velocity increases this maximum moves to lower frequencies. This is consistent with a lee wave with intrinsic frequency of 4-6 cph that is formed at peak tide (flood or ebb). The slope of a line that follows the energy maximum would equal the dominant wavelength (since $\omega = \omega_i + U \cdot k$). There are two lines plotted in figure 51 that bracket the energy maximum, and represent wavelengths of 350 m (dashed) and 1000 m (solid).

It is interesting that the plotted energy looks like a sideways V as opposed to an X. If there was a dominant wavelength set by the topography and one generated waves on ebb and flood, then one would expect to see an X shape. Since the waves generated when the velocity was -1 m/s would have positive wavenumber, they would increase in frequency as the tide slackened. However as the tide changed to a flood, one would now have $U \cdot k > 0$, so that the observed frequency should increase beyond the intrinsic one (4-6 cph). These Doppler shifted waves would not be restricted by the normal internal wave cutoff at $\omega_i = N$, since this is an observed frequency not an intrinsic one.

One possible explanation for the lack of an X-shaped pattern is that the lee waves are relatively quickly damped. If one assumes that the increased vertical kinetic energy is due to internal waves with intrinsic frequency of $4 - 6$ cph and one takes a bandwidth of 2 cph, then one can calculate the total energy of those

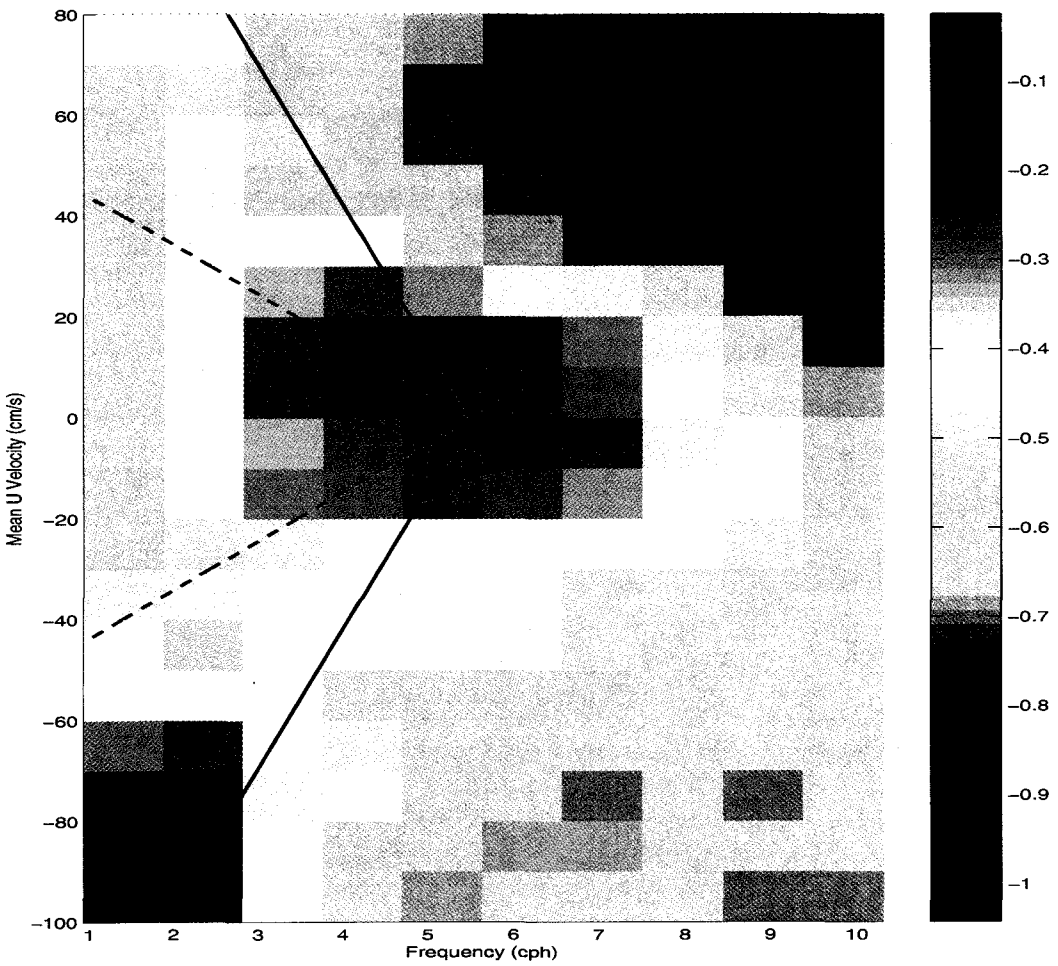

Figure 51: The vertical velocity spectrum (in a log scale and units of $(cm/s)^2/cph$) over a 3.5 hour window as a function of the mean velocity during the window (from ADCP 1999 S). Black lines refer to the slopes of a feature with wavelength of 350 m (dashed) and 1000 m (solid).

internal waves integrated over a water column of $O(100\,m)$. This gives an energy dissipation of $O(40\,J/m^2)$ every 6 hours, once for each flood and ebb. This is equivalent to $1.8 \times 10^{-8}\,W/kg$, a small but non-negligible amount of dissipation. It is also worth noting that these waves have a significant vertical group velocity, so that they could reflect off of the surface and then scatter from the bottom into a larger band of wavenumbers (although this will depend upon the unknown sea floor bathymetry). This band of wavenumbers would translate, via the Doppler shift, into a band of observed frequencies. It is thus possible that the waves are merely diffused over wavenumber space rather than dissipated.

Also the asymmetry in the flood/ebb tide is not obviously explicable. This could be due to local topographic effects, such as the existence of a ridge in a nearby location. Unfortunately, there is not sufficiently detailed bathymetry of the area around the moorings to discover features with wavelengths of less than a kilometer. A plot from the 1998 North mooring (figure 52), another offshore mooring, looks very similar, with energy located near 5 cph at slack tide and progressing to lower frequency with a similar slope (implying a similar wavelength). However, the 1998 North mooring is not strongly V-shaped, having distinctly more wave generation at flood tides than ebb tides. Also the energy generated at peak flood is seen to propagate to high frequencies during ebb tide. This suggests that the flood/ebb asymmetries are due to local topographic effects.

Plots of the 1999 North and 1998 South moorings, which were very near steep side-walls, show increased energy over the offshore moorings, but no discernible pattern. The 1999 East mooring is intermediate, with a marginally visible V-pattern and a lot of "noise" on top.

The existence of the V-shaped pattern is strongly indicative of lee wave for-

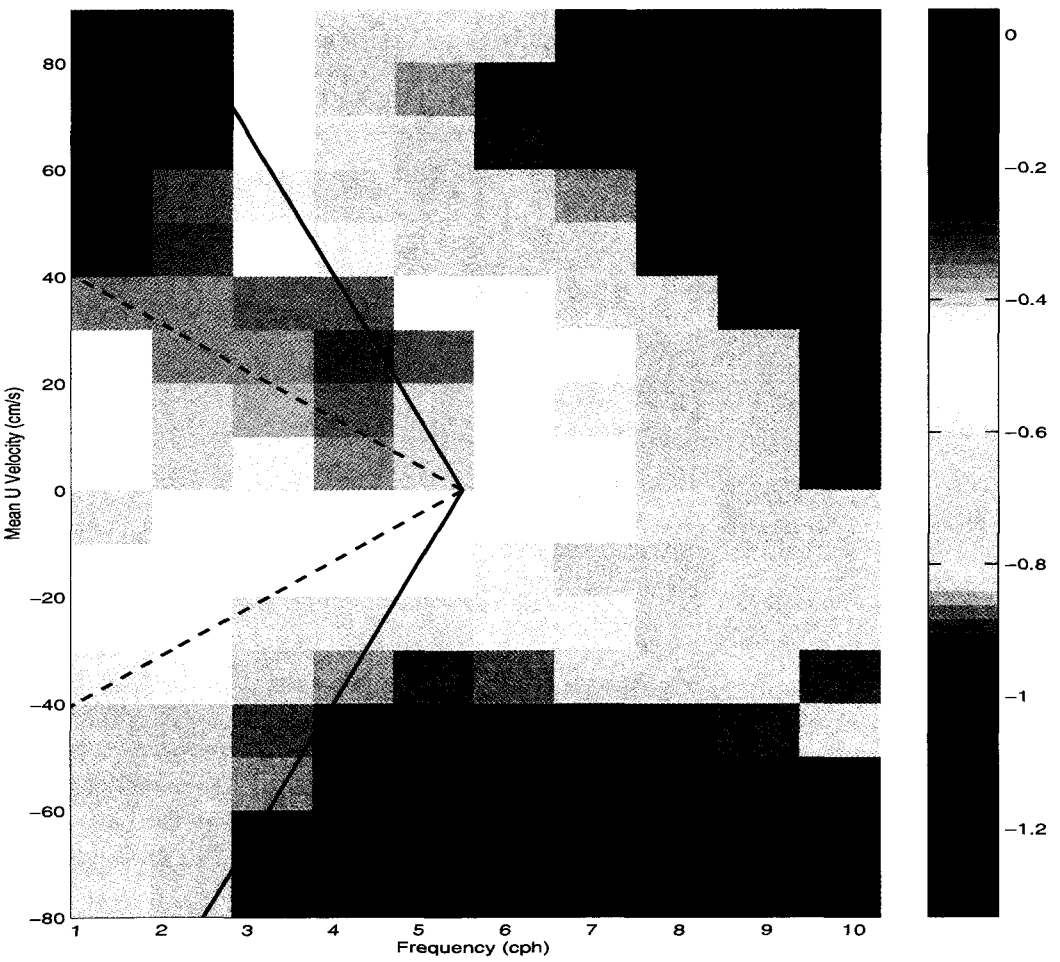

Figure 52: As in figure 51, but for the 1998 North mooring.

mation by the tides. This adds weight to the somewhat shaky conclusions inferred from the ratios of vertical velocity to scaled isopycnal height. It thus seems likely that at any given moment the kinetic energy spectrum is slightly asymmetric, favoring waves that are oriented against the tide.

7.2 Consistency Relationships

Here we will address the the two main consistency relations (CCW/CW and PE/HKE). Each is more complex than the simple comparison used in the Doppler shift arguments. In interpreting the data one needs to keep three influences in mind. The first is the simplest and involves the ratio of vortical mode to internal wave energy. The other two will serve to complicate the first, and are the Doppler shift and the influence of boundaries (or random phase).

The results from 3.2.2 indicate that in the presence of a boundary the normal random phase assumption for internal waves breaks down. However, if one has a spectrum of wavenumbers then one regains the randomness of phase as one moves away from the boundary. I believe that there is a broad spectrum of wavenumbers for the internal waves, since the interaction of waves with the bottom, and the surface to a lesser degree, should scatter waves to different wavenumbers. I therefore believe that most of my measurements are more than 1 or 2 of the shortest wavelengths away from the boundary (which from 3.2.2 implies that the results are within $O(10\%)$ of the random phase value).

Also, the observations are in frequency space, whereas the vortical mode relations exist in Burger number-vortical Rossby number space. For CCW/CW this is not a problem since the expected value for the vortical mode is 1. However in PE/HKE, I will need to make some assumptions about the vortical mode (ie.

assign B and R_ζ) and then plot curves that indicate the expected response of those specific vortical modes.

7.2.1 CCW/CW in the Data

Figure 53 shows the ratio of counterclockwise to clockwise energy as a function of observed frequency for all 5 of the moorings in 1998 and 1999. The coloured lines represent the following moorings: 1998 North (cyan), 1999 South (blue), 1999 East (red), 1999 North (green) and 1998 South (magenta). Here I have listed the moorings according to the distance away from the closest side wall, which tends to be an order repeated in the figure. The solid black line represents the normal internal wave relation, while the black dashed lines represent the internal wave relation after it has been Doppler shifted by the observed tidal currents. The dotted red line represents the vortical mode solution.

There is generally good agreement of all the curves at high frequency, but since the vortical mode and internal wave relations asymptote to the same value it is difficult to distinguish between them. However, the behaviour at high frequency would tend to indicate that the Doppler shift effect is weak. If there was strong Doppler shifting of low frequency intrinsic motion to high observed frequencies, then one would expect the observed ratios to lie below the expected curve (red dashed). This of course assumes that a reasonable portion of the energy is due to internal waves, and not only the vortical mode.

At low frequencies the mooring curves generally lie between the expected internal wave curve and the vortical mode curve. A first explanation for this is that we are seeing a mix of vortical modes and internal waves such that the average lies between the two curves. This is quite probably true. At the very least I can

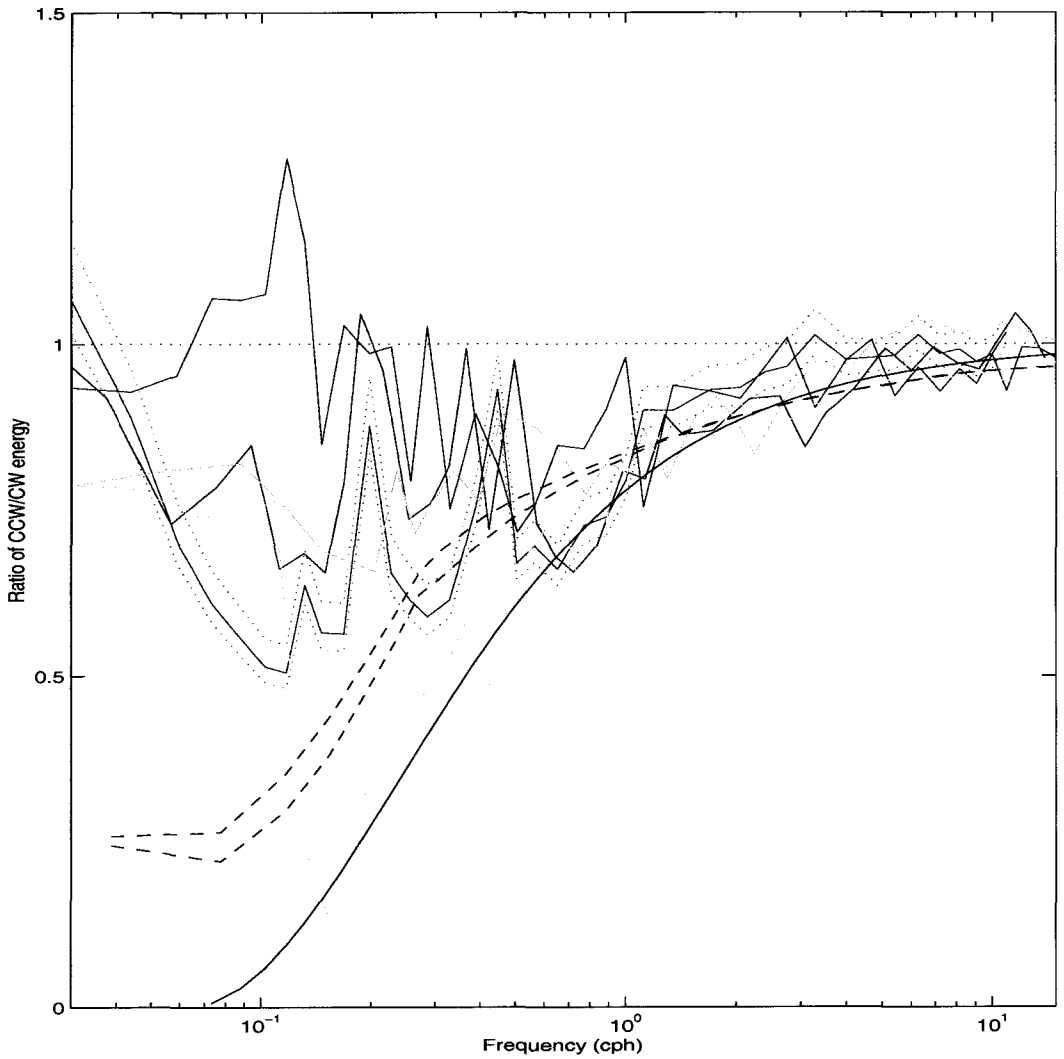

Figure 53: The depth-averaged ratio of counterclockwise to clockwise energy for each of the five ADCP moorings in 1998 and 1999 [1998 North (cyan), 1999 South (blue), 1999 East (red), 1999 North (green), 1998 South (magenta)]. Also plotted are the theoretical curves for internal waves in the absence of Doppler shifting (black solid), vortical modes (black dotted), and for internal waves with the observed Doppler shift (black dashed). The blue dotted lines represent 95%confidence intervals for the 1999 South mooring (solid blue), other moorings have similar error bars.

say that the existence of CCW/CW < 1 indicates the existence of internal waves. Note this is true regardless of boundaries or Doppler shifting.

However, the fact that the curves lie above the expected internal wave curve does not immediately point to the existence of vortical modes. It could instead be due to the Doppler shift which aliased high intrinsic frequency waves into the low observed frequency. Alternatively, it could be due to the phase locking of the internal waves due to the presence of side-walls.

The exact form of the expected internal wave curve in the presence of the observed tidal currents depends upon the wavenumber spectrum of the internal waves. Here I have calculated the resulting spectra for first mode internal waves with wavevectors oriented along the isobaths and either inward or out to sea (two different black dashed curves). One would expect higher mode waves to lie between the first mode curve and the non-Doppler shifted curve. Similarly waves oriented across isobaths would suffer less of a Doppler shift and lie closer to the solid black curve. The Doppler shifted curves are a better fit to the observed ratios, but still don't explain the low frequency behaviour.

The side-walls could also introduce phase-locking within the internal waves. The spectral ratios are generally more than 10% different than the expected internal wave curve (which is a rough bound on the variation expected due to, but far from, the boundaries), so either the elevated values are due to vortical modes or the horizontal wavenumber space is very narrow-banded (such that the phase locked nature of the internal waves is visible several wavelengths from the boundary). The fact that the discrepancy between the data and the internal wave curve increases for moorings that are closer to the wall might lead one to suppose that one is seeing phase-locking. However there is an alternate explanation. This would be

that there is more vortical mode activity near the wall, and so the closer moorings are more heavily weighted toward the vortical mode curve.

In summary, we cannot distinguish which of these two (phase locking or increased vortical modes) causes the progression in the observed CCW/CW. However, there must be internal waves to explain $CCW/CW < 1$.

7.2.2 PE/HKE in the Data

In order to calculate PE/HKE we need to mix data from different moorings. As we have seen above in CCW/CW there could easily be spatial gradients in the data which make inter-comparison of moorings difficult. I have chosen to take a single ADCP and compare the results with the potential energy calculated from two flanking T-chains (but not for 1998 South because there only is one adjacent T-Chain). In this way any strong gradients should show up as variations between the two T-chain potential energies. I use three sets of moorings. The first is composed of 1999 ADCP-S and the temperature chains 1999-N and 1999-S. The second set involves 1998 ADCP-N and the temperature chains 1998-NE and 1998-NW (figure 21). The third involves 1998 ADCP-S and the temperature chain 1998-S. Also since isopycnal height can vary between the different temperature chains, and within the record at a single chain, I have experimented with different velocity bins from the central ADCP. The variation between the different velocity bins was weak and so I only use a central bin which represents the midpoint between the average isopycnals. The results are shown in figure 54.

Although, I have only plotted the potential energy on one specific isopycnal the general result is fairly true for most of the "usable" isopycnals (Most of my "usable" isopycnals are within the central third of the water column). It is pos-

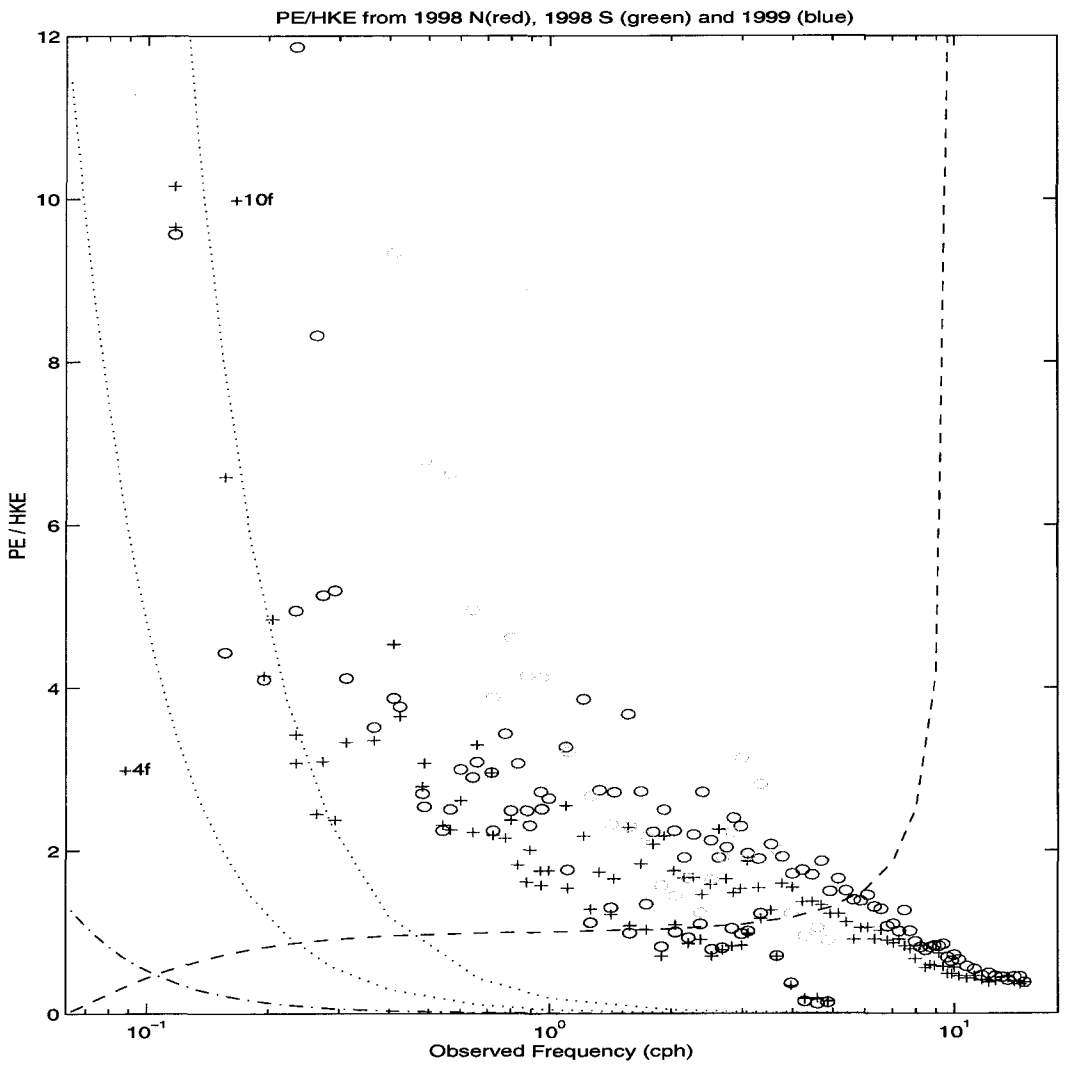

Figure 54: The ratio of PE/HKE from 1999 (blue; using ADCP-S and T-Chains N (o) and S(+)) and for 1998 North (red; using ADCP-N and T-Chains NE(o) and NW(+)), and 1998 South (green; using ADCP-S and T-Chain S). The dashed black curve represents the expected internal wave relation. The dash-dot represents a geostrophic current and the dotted curves represent first mode eddies with the labelled vorticity (refer to equation (60)).

sible that there is significantly different behaviour in the top 30 m of the water column, but the facts that isopycnals in this region frequently outcrop and that the velocity signal is strongly degraded during the daytime make it difficult to assess. Also the red and blue plots represent offshore moorings, while the green data is from a set of moorings located alongside a steep wall. There is a somewhat consistent behaviour between the three moorings, with high values at low frequency decreasing to lower values at high frequency. Also the two PE measurements from 1998 North (red + and o) are quite similar, whereas the 1999 measurements show consistently more PE at one T-chain (blue o:1999 T-Chain North) than at the other (blue +: 1999 T-Chain South). This is not entirely unexpected since the two T-Chains from 1998 North flank the central ADCP in an along-strait direction, whereas in 1999 the T-Chain with elevated PE is considerable closer to the wall then the other T-Chain (figure 21). I will tend to favor comparisons between the 1999 ADCP-S and the 1999 T-Chain South, since I believe these two moorings are more closely related (ie. blue + is more believable then blue circles). There is only one T-Chain for 1999 South, but it is located at roughly the same distance from the sidewall as the ADCP.

The PE/HKE ratio for the vortical mode is given by (60). To transform to observed frequency space I assume that $k = \omega/U_{rms}$, which gives

$$\frac{PE}{HKE} = (1 + \zeta/2f)^2 \frac{N^2}{f^2} \frac{m^2 U_{rms}^2}{\omega^2}. \tag{85}$$

The plotted lines use a first mode assumption ($m = 2\pi/120\,m$) and $U_{rms} = 0.4\,m/s$. The one thing to note about this relation is that it actively uses the Doppler shift of the vortical mode and thus is truly the predicted curve in observed frequency space. By contrast the internal wave curve (dashed black line)

is only true in intrinsic frequency space and is thus plotted as a guide rather than an absolute.

The data cannot be said to clearly resemble any of the curves, nor is it bounded between the internal wave and the vortical mode curves. First we will consider the data quality. The HKE calculation is one of the most reliable ones made. Its only potential failing is due to the aliasing of small wavelength features by the spread of the ADCP beams. I believe that this effect is negligible for the current calculation. PE is much more dubious. As mentioned before, the T-ρ mapping will tend to overestimate the potential energy in situations where salinity partially compensates the temperature fluctuations. This should not be very important for high frequency motions (where there is less time to alter the T-S relation), but low frequency motions could be adversely effected. It is difficult to estimate the potential magnitude of this over-estimation at low frequencies, but I cannot imagine that correcting for it would reduce the estimated isopycnal displacements by more than a factor of 2.

The high frequency estimates of PE/HKE > 1 (for $\omega > 1$ cph) could be fit by a vortical mode curve, but would require an estimated vortical Rossby number that is not only above the observed vorticities (see next section), but would be inherently unstable (since its vorticity exceeds N). This region could be explained as internal waves in one of two ways: either through the Doppler shift or through the effect of top and bottom boundaries.

One needs some care in applying our intuitive idea of how the Doppler shift will act. It is important to realize that one cannot just take the dashed curve in figure 54 and "diffuse" it in one's mind to get the effect of the Doppler shift. Instead the Doppler shift acts separately on the potential energy and horizontal

kinetic energy spectra, not on their ratio. The effect of Doppler shifting a Garrett-Munk spectrum was shown in figure 20. The horizontal kinetic energy over the region ($\omega > 1$ cph) was increased, particularly beyond $\omega > 3$ cph. There was a marginal decrease below $\omega < 1$ cph, and then a significant hump around $\omega \approx 0.2$ cph. The potential energy spectrum shows general increases, though small, at high frequency and a small decrease over much of the low frequency spectrum, except very near $\omega = f$, where it increases. This unfortunately does not help explain the region of PE/HKE > 1 at mid-range frequencies. However, it does provide an explanation for PE/HKE < 1 observations at the highest frequencies. The internal wave energy in this region is Doppler shifted from nearby regions, and the Doppler shift increases the kinetic energy spectrum more than it decreases the potential energy spectrum.

The other alternative explanation is due to the modal structure of the waves in the vertical. If one assumes that the majority of the wave energy is in the first mode, then at mid-depths, where these comparisons are made, the potential energy is maximum and the kinetic energy is minimum. This would certainly give the indicated values of PE/HKE > 1. This can be checked by choosing isopycnals and velocity bins that are closer to one of the boundaries. The velocity structure is easily resolvable over the lower two-thirds of the water column and shows indication of a mid-depth minimum. However, it is a very weak minimum, being only 10% different from the average value. The isopycnals provide a larger data analysis problem. Mid-depth isopycnals were chosen since they tend to stay at mid-depth and only rarely encounter boundaries. The closer an isopycnal is to the boundary the more often the record is fragmented, which provides a complication for spectral analysis. However it does seem, from comparisons made during times

of good data, that the displacements are reduced near the boundary.

Therefore, I think that most of the observed PE/HKE > 1 in the region of $\omega > 1$ cph can be explained by the modal structure imposed by the boundaries. It is also likely that the predictions are biased high by our mapping of temperature to density. The 1998 North moorings are closer to the predicted curves than the other two sets of moorings. This is partially due to the better T-ρ mapping at this site, which was due to the reduced variability in the T-S relationship. As an aside, the strong peak visible in two of the records near $\omega = 3$ cph is consistent with the timing of the cross-strait seiche. The weaker peak near $\omega = 0.3$ cph matches the along-strait seiche, but the bottom slope in the along-strait direction under these moorings is not very large.

At low frequencies ($\omega < 1$ cph), there is considerably elevated levels of PE/HKE. This is not explainable as an effect of the Doppler shift on internal waves. This leaves three options: it is due to vortical modes, it is an artifact of the mapping of T-ρ, or it is due to the modal structure of the internal waves.

I assume that the T-ρ mapping is inadequate at low frequencies, but I don't think it can account for more than a factor of 2 in displacement, or 4 in PE. This can significantly reduce the observed ratios, but some of them will still be quite large (particularly the few elevated values that lie beyond the axis of figure 54).

We cannot clearly distinguish between the two remaining possibilities: vortical modes or internal waves in the presence of boundaries. The internal wave explanation is the more problematic of the two, in my mind, since it requires either a significant reduction of kinetic energy or increase in potential energy at mid-depths. There are some fluctuations in velocity, as a function of depth, on these time scales, but we still need increased potential energy. On long time scales the

isopycnal data near the boundaries is much more fragmented, but does not appear to indicate large vertical structure.

This would tend to indicate that the elevated levels at $\omega < 0.2$ cph are due to vortical modes. The uncertainty in the exact level of PE, due to uncertainties in the T-ρ mapping, makes the determination of a best fit vortical mode impossible. However, the elevated level would tend to indicate vortical modes that are in cyclostrophic rather than geostrophic balance.

7.3 Vorticity and Divergence

Vorticity and divergence place additional constraints on the partition of energy between the vortical mode and internal waves. They are somewhat different from the previous relationships (CCW/CW and PE/HKE) since they depend upon the measurement of spatial gradients. The previous consistency relations were essentially point measurements. Although my PE and HKE were not measured at the same location, they ideally should have been.

We recall that geostrophic motions have no divergence, and that cyclostrophic motions have negligible divergence (at least for our data set). Thus divergence is a characteristic of internal waves. Internal waves also have more divergence than vorticity. Thus vorticity in excess of divergence is a clear indication of vortical modes.

The vorticity, and to a much lesser extent divergence, is dominated by the large-scale shear of the tidal flow (figure 55). This is entirely understandable since the tide at the boundary leads the tide further out. However, I am primarily interested in the signature of vortical modes and internal waves, and so I shall concentrate on vorticity calculated from the detided velocity signals. Also, the signal

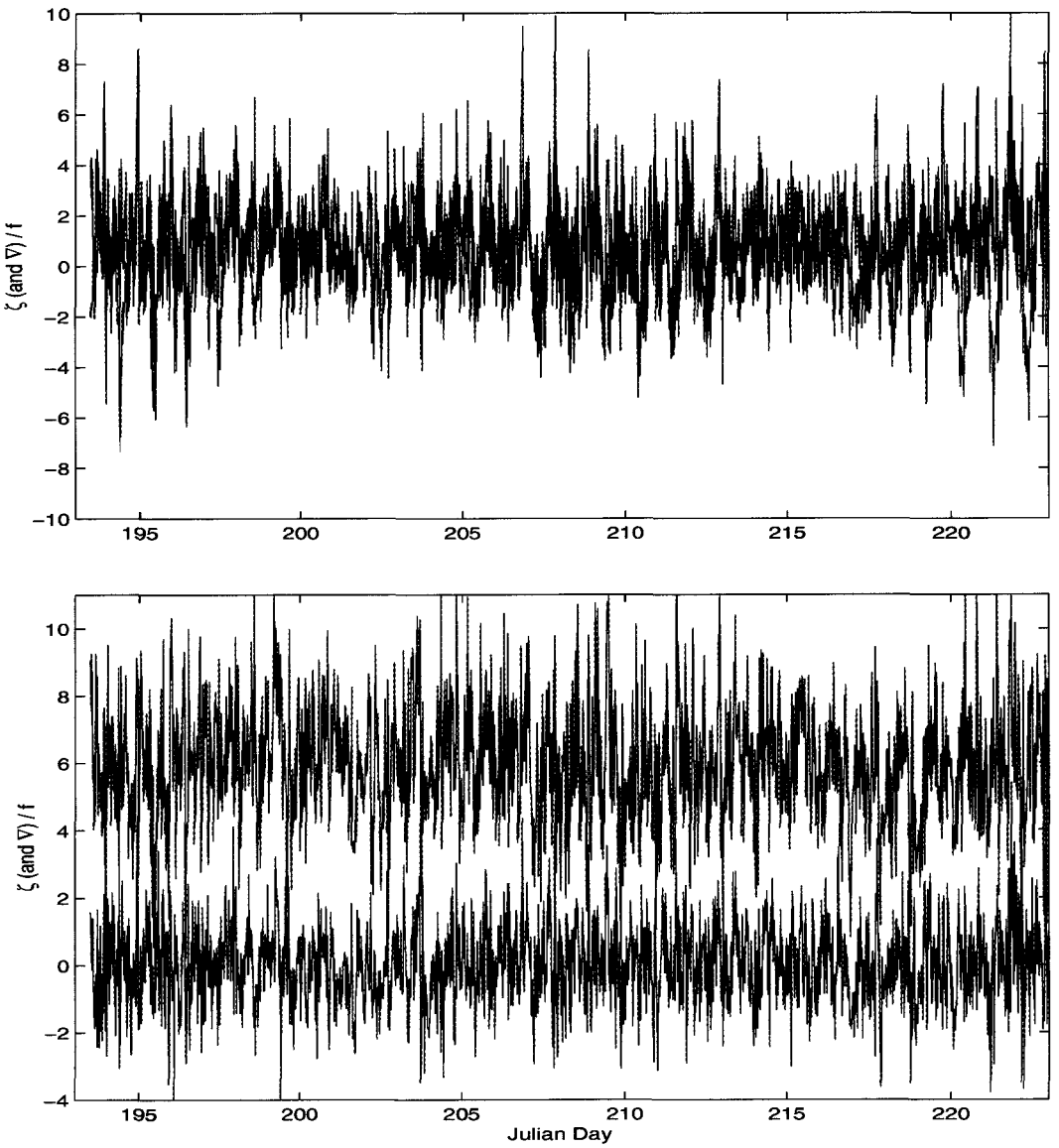

Figure 55: Vorticity (blue) and divergence (red) for the full velocity record (top), and the detided/demeaned residuals (bottom, divergence offset by +6 for clarity). The vorticity and divergence from the full velocity record have considerable energy at tidal frequencies.

was demeaned, since we are not interested in the mean vorticity or divergence due to the estuarine flow. It is interesting to note that the means of the vorticity and divergence records calculated from the residuals are not statistically different from zero at a 68% confidence level (except at the top of the mixed layer which seems to have a weak ($\zeta = 0.1$ f) mean vorticity). As an aside, the vorticity calculation needs all three moorings, and so can only be performed for the 30 day window when the 1999 ADCP East mooring is deployed. The vorticity and divergence spectra, as well as their ratio ($S_\nabla(\omega)/S_\zeta(\omega)$), are plotted as a function of fractional height is plotted in figure 56.

The divergence is everywhere larger than the vorticity, except for high observed frequencies near the surface. The existence of large divergence clearly indicates the existence of internal waves. The existence of more divergence than vorticity does not immediately rule out vortical modes. Before proceeding, one would like to first check the value of the measured divergence and vorticity to make sure they are sensible, and not merely noise.

A representative divergence ($1.3 \times 10^{-4}\, s^{-1}$), which for internal waves using a first mode assumption in (48), generates a predicted vertical velocity of $0.0025\, m/s$. This is a reasonable vertical velocity ($9\, m/h$) but is not likely to hold for very low frequencies, since the associated displacement over a period soon becomes unphysical. It thus seems likely that the divergence at low frequencies is partially influenced by the Doppler shifting of higher intrinsic frequency waves. Higher mode waves would linearly reduce the expected vertical velocity, and consequently displacement, and so that the divergence signal at low frequencies could also be a result of high mode waves. Looking at a representative vorticity ($1.1 \times 10^{-4}\, s^{-1}$) and applying (47) implies a vertical displacement of $19\, m$.

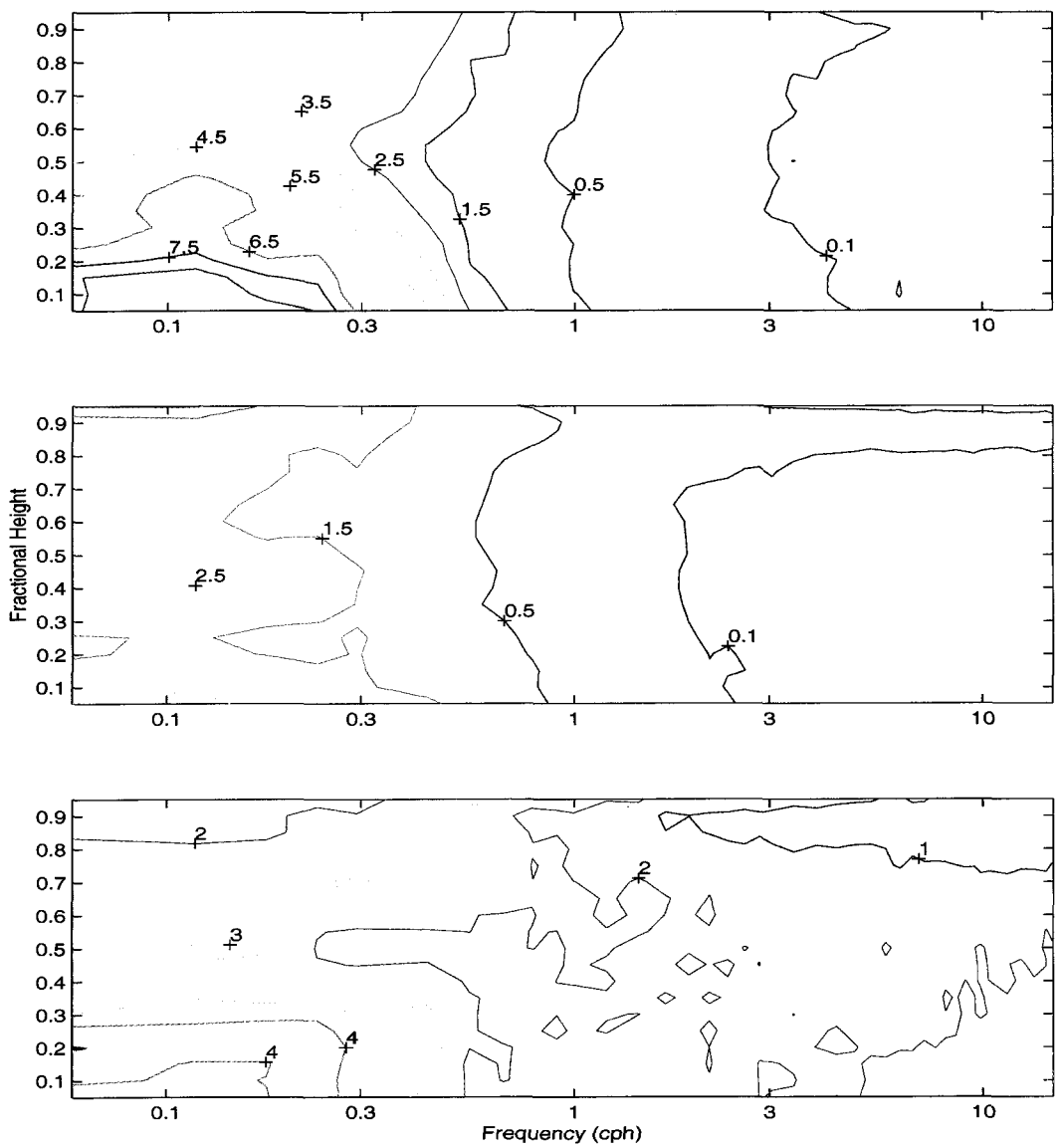

Figure 56: The divergence (top, scaled by f^2), vorticity (middle, scaled by f^2) and the ratio of divergence to vorticity (bottom) spectra as a function of fractional height.

Again this is an entirely sensible displacement for an internal wave.

Both the vorticity and particularly the divergence spectra show some vertical structure, which is indicative of a first mode internal wave. The divergence at low frequencies near the bottom shows values that are larger than at the corresponding frequency near the surface. This may be due to an inadequate mapping between moorings. It could be that one or two of the points is in the bottom Ekman layer while the third is not. This would tend to measure divergence that is not of physical interest.

Looking at the ratio of divergence to vorticity, one should first note that although they are individually modified by the presence of boundaries their ratio is not. Secondly, one might notice that the ratio does not look like the expected curve ($S_\nabla/S_\zeta = \omega_i^2/f^2$), in fact it slopes in the other direction, although only mildly. This is difficult to explain using internal waves. To generate the observed spectral ratio, one would need to make one of two assumptions. The first is that the vorticity and divergence at a given frequency have different wavenumbers associated with them. This is quickly dismissed as impossible after considering the internal wave equations. The second choice assumes that the internal wave spectrum is concentrated in a number of discrete frequency/wavenumber bands. This is plausible, but seems to require a certain amount of preordination. The region with more vorticity then divergence, at high frequencies near the surface, is not truly indicative of vortical modes. The ratio here is only slightly higher than one, and both the vorticity and divergence are quite small in this region. It could easily be an artifact of the data analysis process.

One additional factor which we need to consider is that internal waves cannot have a relative vorticity signal less than $-f$. This is a simple corollary of conser-

vation of potential vorticity; since one can stretch two isopycnals arbitrarily far apart (ie. no bound on positive vorticity), but can only bring them together until they touch. Since the data seem to have a significant amount of vorticity less than $-f$ (figure 57), one must suppose this implies the existence of vortical modes.

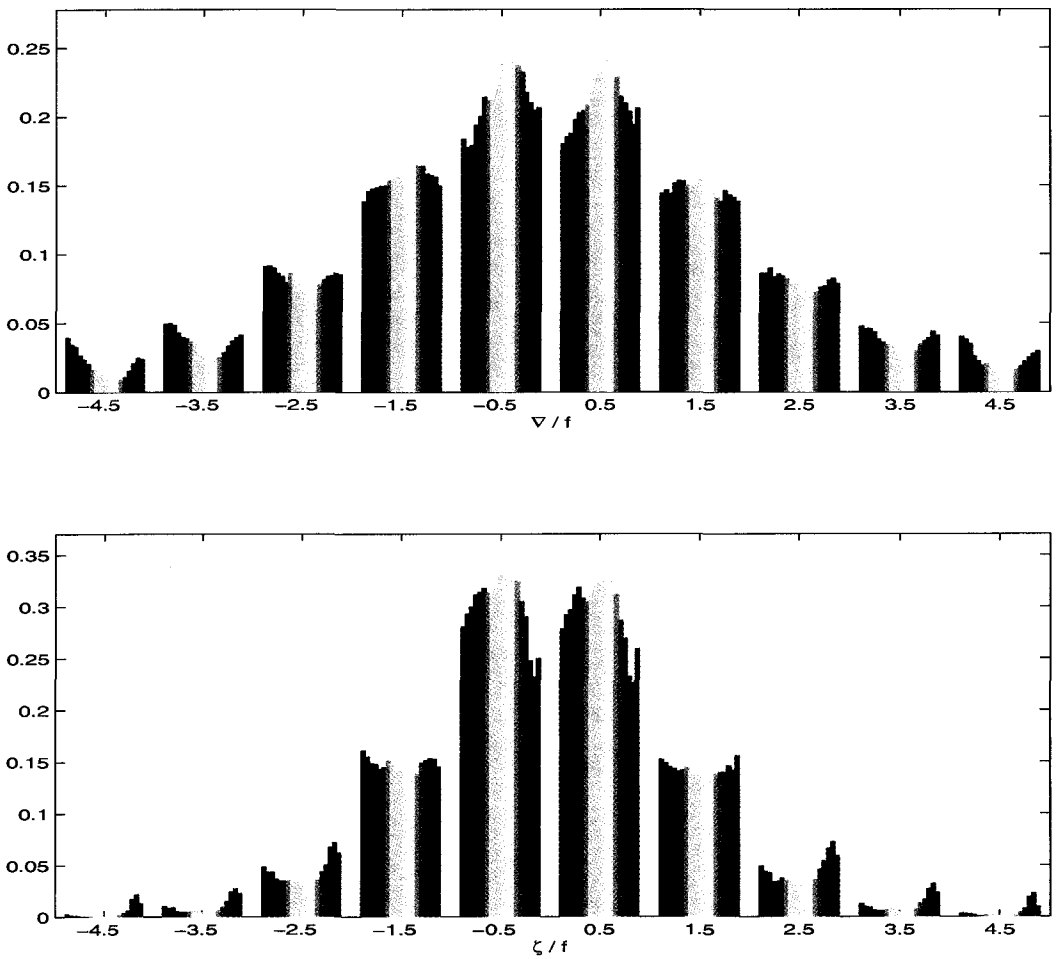

Figure 57: Histograms of the measured divergence (top) and vorticity (bottom) scaled by f. The colors within a bar represent depth and stretch from near bottom (blue) to near surface (red).

I previously ascribed the increased potential energy at low frequencies to vor-

tical modes, and so one might then ask "How much vorticity would one expect to be associated with that potential energy?" (ref. section 3.3.6). Figure 58 shows the vorticity spectrum scaled by f^2 that one would expect if the measured potential energy was entirely due to geostrophic (or cyclostrophic) vortical modes. This is under the assumptions that $H = 120\,m$, $N = 0.018\,s^{-1}$ and $U_D = 0.5\,m/s$; obviously one could adjust these numbers to change the results by a factor of 3 (or more). This is using a mid-depth isopycnal, although other isopycnals only change the results by at most 50%.

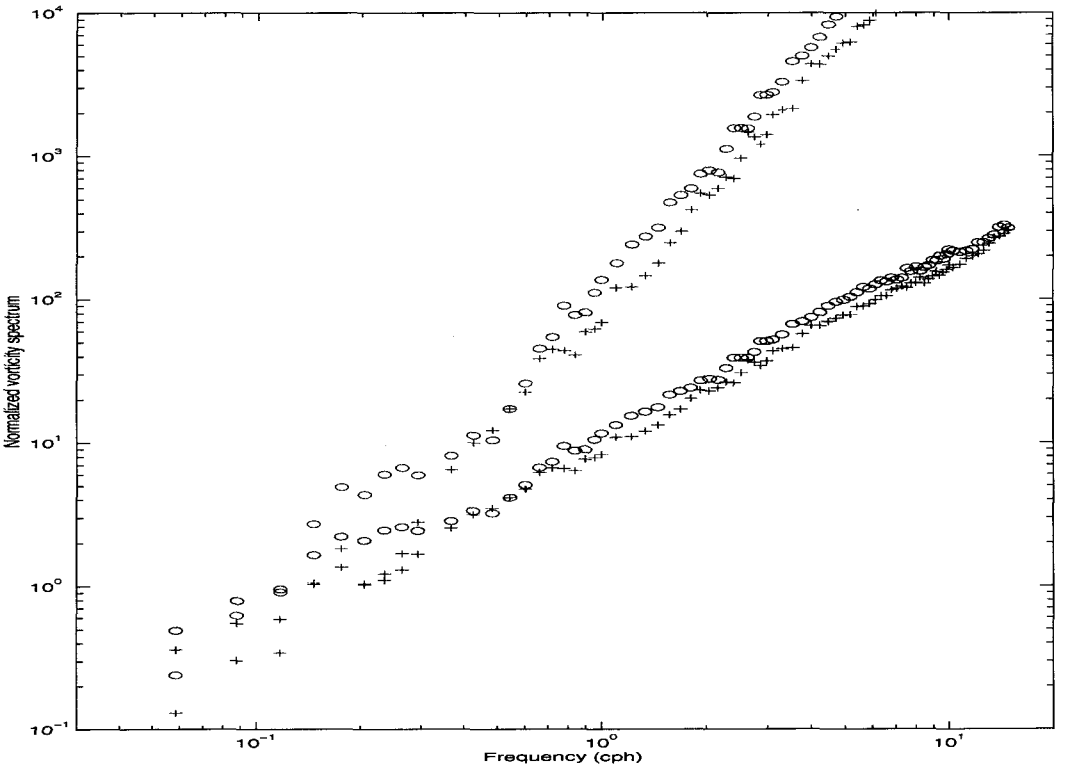

Figure 58: The vorticity spectrum (scaled by f^2) that is expected if one assumes that all the measured potential energy is due to a vortical mode in geostrophic balance (blue) or cyclostrophic balance (red) [for 1999 T-Chain North (circles) and 1999 T-Chain South (pluses)].

We can see that a vortical mode at low observed frequency can contain significant potential energy while exhibiting only moderate vorticity, however the vorticity rapidly increases as we move to higher observed frequencies. This is understandable since for a geostrophic vortical mode the vorticity is proportional to L^{-2} (and hence the spectrum goes like L^{-4}). Using our assumption that $\omega = 2\pi/L$ (which is even more accurate for higher frequencies) one finds that the vorticity spectrum scales like ω^4 times the potential energy spectrum. Comparing with figure 56 (middle panel), we see that the observed vorticity is able to account for all of the very low frequency potential energy, but at frequencies above $3f$ for geostrophic (or $5f$ for cyclostrophic) the vortical modes must be close to non-existent since we do not observe sufficient vorticity. This is not too bad, since the strong vortical mode signature in the PE/HKE ratio is primarily below $5f$.

However, there is another point that needs to be made concerning the vortical mode, and that relates to the implied length and velocity scales of the mode. Since the vortical mode is inherently sub-inertial it is not a bad assumption to assume that the observed frequency is entirely due to the Doppler shift (ie. $\omega = U_D k$). However, for low observed frequencies this can imply substantial length scales (for example, a vortical mode observed at $\omega = 0.3\,cph$ would have a length scale of $6\,km$ assuming $U_D = 0.5\,m/s$). As this length scale becomes similar in size to a tidal excursion (as it would at lower frequencies) it becomes very difficult to interpret the data in terms of a vortical mode. The Doppler shifting velocity is itself dependent on frequency, since it needs to represent an average velocity over that period. It is therefore true that the velocity used above, $U_D = 0.5\,m/s$, would be inappropriately large for a lower frequency, such as $\omega = 0.1\,cph$. In fact there will be a substantial drop in the average advecting velocity, U_D, for frequencies

greater than the dominant M_2 frequency.

It also should be noted that these large vortical modes would need to have large horizontal velocities. If one assumes that $U = \zeta L$ then for the above mentioned vortical mode with the vorticity given in figure 56 (middle panel) one finds that $U = 0.7\, m/s$. It is possible to reduce this by a factor of two if the vortical mode has some intrinsic frequency and/or I pick a larger Doppler advecting velocity, but the velocity is still unrealistic. The only assumption that can be made to potentially alleviate this problem is to assume the vortical modes are not in solid body rotation over their full length scale.

8 Discussion

This thesis has investigated a number of problems concerned with lateral mixing in the ocean. In the introduction, I stated a number of goals that this thesis was meant to address. It seems appropriate to revisit each of the three main ideas and see what we have learned.

Langmuir Circulation

I feel that the goal of deriving a robust parameterization for the cross-wind eddy diffusivity has been successful achieved. The Langmuir circulation diffusivity had previously been parameterized either by empirical formulae based on very specific experiments whose generality was questionable, or by exceedingly simple cartoon models of Langmuir circulation. These results present a parameterization which not only captures much of the important dynamics, but also depends only on readily observable variables (such as wind speed). The fact that the derivation is independent of the unknown eddy viscosity is more fortuitous than planned, but strongly increases the applicability of this formulation. Furthermore, the reduction of the friction velocity and the two wave variables to a single variable, namely wind speed, through the use of previously derived relations makes this parameterization computationally efficient, and easily employable in operational models.

The Langmuir circulation calculation suffered most from its assumption of two-dimensionality. The obvious method to solve this is to run a three dimensional model, but for sufficient time to have robust statistics. This is really just a matter of time, since computational advances will presumably enable this type

of calculation to be done quickly in the future. Current three-dimensional models are also hindered by their rather constrained downwind domain. These models are periodic in the downwind domain, so what ever travels out the end reappears in the beginning. This is a necessity of the computation, but for small down-wind domain sizes one must wonder whether this arbitrarily imposed periodicity does not skew the statistics into an unrealistic state.

Lateral Reynolds Stress

The lateral Reynolds stress calculations are interesting because they are fairly novel and more importantly because they allow us to investigate the form of the eddy viscosity. The stress calculations themselves are relatively easy and the results have only minor sensitivity to my subjective choices. What is more problematic for the eddy viscosity calculation is the determination of the large-scale shear. This was not originally expected. Lateral mixing in the ocean has been poorly studied in comparison to vertical mixing. Before this study there were few estimates of lateral eddy viscosity, and none at these time and space scales. They thus provide a first step toward a usable parameterization.

The motivation for measuring the Reynolds stresses, and parameterizing them as an eddy viscosity, is to provide some guidance for the modelling community. The novelty of the measurement is useful, but is far short of the goal of a robust parameterization. It is interesting to first consider what forms of lateral momentum transfer are currently used in models. Two comparable models are the one by *Davies and Hall* [2000] in the Irish Sea, and that of *Cummins, Masson and Foreman* [2000] (see also *Cummins and Oey* [1997]) in Juan de Fuca Strait and surrounding waters. In the first of these papers they use no lat-

eral diffusion of momentum at all (at least that is what their paper indicates). The second uses a Smagorinsky formulation, which can be expressed as $A_H = C\Delta x\Delta y[(\partial U_i/\partial x_j + \partial U_j/\partial x_i)^2]^{1/2}$, where $\Delta x, \Delta y$ are the grid resolution and C is the Smagorinsky constant. With a $2\,km$ grid resolution and a Smagorinsky constant of 0.05 (*Diane Masson,* personal comm.), and with a strain rate of $3\times10^{-4}\,s^{-1}$ (which is large but not unusual for our data) one finds $A_H \approx 50\,m^2/s$. The model is therefore over-estimating the observed horizontal eddy viscosity. One could easily note that if the same model was run with $1\,km$ resolution the Smagorinsky diffusivity would be $A_H = 12\,m^2/s$, in much better agreement with our data. However, the modellers did not have any data to compare with before this study, so that any agreement of their imposed eddy viscosity with my measured one should be seen more as fortuitous then expected. It may not be possible to run a computer model with a measured lateral eddy viscosity of $O(10\,m^2/s)$ and have it remain stable, but at least now one is cognizant of what values to aim for.

I am unclear as to how my limited data can improve the ability of coastal modellers to parameterize the lateral eddy viscosity. One could obviously fit an empirical curve to my data, but it is hard to believe that such a fit would have universal applicability. Certainly, I can say that a constant eddy viscosity parameterization does not adequately capture the variability in figure 41. It could be that the constant eddy viscosity parameterization would do a better job if I were resolving the shear adequately. This may be the case, but it doesn't help the models, since they would need to have equally fine resolution to resolve the necessary shear. At the very least my data provides an initial foundation on which to explore more complex parameterization.

Internal Waves vs. Vortical Modes

The goal of unambiguously dividing the data into vortical modes and internal waves has not been achieved. This is not surprising given the limitations in the data set. However, a synthesis of the data would lead me to the conclusion that both internal waves and vortical modes are in the data set. The internal waves are fairly ubiquitous over all observed frequency ranges, although whether this is inherent in the wave field or due to Doppler shifting is unclear. The vortical modes are constrained to the low frequency ($\omega < 5f$) portion of the observed spectrum. Although the CCW/CW ratio could imply the existence of vortical modes at higher frequencies, the PE/HKE ratio at mid to high frequencies can be explained only by using internal waves. If there were vortical modes in the high observed frequency band, then we would expect a near negligible increase to the PE but a noticeable increase to the HKE, which would imply PE/HKE should lie below the internal wave curve. It is thus very doubtful that the observed signal at $\omega > 10f$ has any signature of the vortical mode.

The division of the data set into vortical mode and internal waves was motivated by a desire to explain the observed Reynolds stress, and to better parameterize the inferred eddy viscosity. It is difficult to assign the Reynolds stress to either vortical modes or internal waves. Intuitively, I feel that the stirring nature of an eddy will be much more effective in the transfer of momentum, than the sloshing effect of internal waves. The only way to truly answer this question would be to decompose the velocities in the time domain into internal waves and vortical modes, and then calculate the Reynolds stress of each component. This is not only beyond the scope of this thesis, but impossible with our data set.

If we assume that vortical modes are responsible for the Reynolds stress than

this implies a couple points. First, we would expect that the approximation $A_x = A_y$ is a reasonably good one, since an eddy will not have a significant preferred direction. Second, the Reynolds stress and eddy viscosity I measure may be strongly dependent on the distance from shore. If one envisages eddies as being formed primarily by interaction with the sloping sidewalls and one assumes that the eddies are very slow moving features, then one must conclude that far from the sidewalls there are probably few eddies to stir the fluid. I do not have sufficient moorings to discuss the cross-isobath change in eddy viscosity, nor do I have any knowledge as to what scale would govern the decrease in eddy viscosity as one progressed away from the wall. This is perhaps an area more readily explored by numerical modelling, which could be subsequently verified by a well planned experiment.

Future Avenues of Inquiry

It is customary to mention some of the open avenues of investigation and some of the improvements that could be made. From an observational standpoint the two largest shortcomings are in the resolution of the large-scale shear and in the density field mapping. The large scale shear could always be resolved with the use of more instruments in a closer array, but this is easier said then done. It is probably reasonable to deploy our ADCP moorings as close as 300-400 m apart, but one needs to get sufficient instruments and have data returned from each of them. However it might be possible to mount a low frequency ADCP at mid-depth and oriented sideways, so as to resolve the velocity along a mid-depth line connecting two moorings. However, beam spreading would be a much more serious concern in an ADCP oriented in this fashion.

The density could be resolved with a singe well instrumented chain. If one

had 6 or 7 density resolving pods on a single chain, and had none on the others, one might have more faith in the T-S relationship then is achieved by breaking the instruments up over all the different temperature chains.

An interesting question, that could possibly be resolved with the existing data, is "Which is more important the vertical or the horizontal eddy viscosity?". Presumably, near the bottom, vertical mixing is the most important sink of momentum whereas further up in the water column horizontal mixing might become more important. As one moved further away from a side-wall, the depth at which the transition from vertical to horizontal mixing occurred would probably rise in the water column. However, the spatial distribution of $\overline{u'v'}/\overline{u'w'}$ is unknown.

Appendices

These appendices contain the derivations for the modified consistency relations presented in the text. Although the concept of a boundary imposing a modal structure on an internal wave through interaction of the incident and reflected waves is common, I have not found a clear discussion of how this would influence the expected consistency relations. These appendices also deal only with the case of purely horizontal or vertical boundaries since these are the easiest. The reflection problem from a slope is conceptually easy, but mathematically difficult and I have not obtained a simple expression for that case.

Appendix A: PE/HKE for Internal Waves Above a Flat Bottom

One can easily imagine that potential energy (and vertical kinetic energy) must go to zero at the bottom, while kinetic energy (in the absence of friction) is unrestrained. Thus the PE/HKE ratio must got to zero at the bottom regardless of frequency. It is also fairly easy to imagine that the result should be independent of the direction of propagation of the wave.

The case of reflection from a flat bottom has the following relations between the incident and reflected wave. The horizontal wavenumbers are unchanged ($k_i = k_r$ and $l_i = l_r$, where subscripts denote incident and reflected waves), the vertical wavenumber changes sign ($m_r = -m_i$) and the amplitude of the wave is unchanged ($A_i = A_r$). This results in the following form for the velocity of the sum of the two waves,

$$u = 2A_{inc}\tan\theta_{inc}[-\cos\phi_{inc} - if/\omega\sin\phi_{inc}]e^{i(kx+ly-\omega_i t)}\cos(m_{inc}z), \quad (86)$$

$$v = 2A_{inc}\tan\theta_{inc}[-\sin\phi_{inc} + if/\omega\cos\phi_{inc}]e^{i(kx+ly-\omega_i t)}\cos(m_{inc}z), \quad (87)$$

$$w = 2A_{inc}e^{i(kx+ly-\omega_i t)}\sin(m_{inc}z). \quad (88)$$

I can then compute the horizontal kinetic energy as $uu^* + vv^*$and the vertical kinetic energy as ww^*, where * denotes the complex conjugate. Then using the fact that vertical kinetic energy and potential energy for internal waves are related by $PE/VKE = N^2/\omega_i^2$ (which holds regardless of boundaries), I can write PE/HKE as

$$\frac{\frac{N^2}{\omega_i^2}ww^*}{uu^* + vv^*} = \frac{N^2/\omega_i^2\, A_iA_i^*\sin^2(m_iz)}{\tan^2(\theta_i)\,(1 + f^2/\omega_i^2)\,A_iA_i^*\cos^2(m_iz)}.$$

Now $\tan^2(\theta_i) = (N^2 - \omega_i^2)/(\omega_i^2 - f^2)$ which allows us to rewrite the above as

$$\frac{PE}{HKE} = \frac{N_i^2\,(\omega_i^2 - f^2)}{(N^2 - \omega_i^2)\,(\omega_i^2 + f^2)}\frac{A_iA_i^*\sin^2(m_iz)}{A_iA_i^*\cos^2(m_iz)}. \quad (89)$$

In the case of a single monochromatic wave, I can cancel the amplitudes and I am left with a $\tan^2(m_iz)$ in the vertical multiplying the expected frequency relation . However it is important to realize that in the presence of a spectrum of waves one must first integrate the potential and kinetic energy separately and then take the ratio.

Let us consider the case of an internal wave spectrum that is white in vertical wavenumber space, and that is constrained by two limits $[m_{min}, m_{max}]$. Then

integration of the top and bottom of (89) with respect to m yields

$$\frac{PE}{HKE} = \frac{N^2\left(\omega_i^2 - f^2\right)}{\left(N^2 - \omega_i^2\right)\left(\omega_i^2 + f^2\right)} \frac{\sin(2m_{min}z) - \sin(2m_{max}z) + 2m_{max}z - 2m_{min}z}{\sin(2m_{max}z) - \sin(2m_{min}z) + 2m_{max}z - 2m_{min}z}.$$

The vertical wavenumber spectrum is not white in the ocean, and so I will consider one other case where the amplitude has a m^{-2} dependence. In this case the vertical structure function, $F(z)$, becomes

$$F(z) = \frac{(1 - 2m_i^2z^2)\cos(2m_iz) - m_iz\sin(2m_iz) - 24m_i^3z^3\mathrm{si}(2m_iz) - 1|_{m_{min}}^{m_{max}}}{(-1 + 2m_i^2z^2)\cos(2m_iz) + m_iz\sin(2m_iz) - 24m_i^3z^3\mathrm{si}(2m_iz) - 1|_{m_{min}}^{m_{max}}},$$

where $\mathrm{si}(x) = -\int_x^\infty \frac{\sin t}{t} dt$. These two vertical profiles are plotted in figure 15. Clearly for any other given amplitude dependence, one could compute the integral and find the expected vertical profile. It's also possible that the vertical wavenumber spectrum has some frequency dependence as well. In this case the frequency character of the PE/HKE ratio will be altered, but it seems probable that the integration over wavenumber space would tend to minimize this perturbation.

Appendix B: PE/HKE for Internal Waves Beside a Vertical Wall

It is fairly clear that potential energy (and vertical kinetic energy are unaffected by a vertical wall). Thus the only influence is due to the modification of the horizontal kinetic energy. It is clear that horizontal velocities must be constrained to be parallel to the wall at the wall. Thus I expect the horizontal kinetic energy to depend on the angle at which the wave encounters the wall; being unaffected for a wave perpendicular to the wall, and with increasing effect as the wave becomes closer to parallel.

Appendix C: CCW/CW for Internal Waves Beside a Vertical Wall

The effect a wall on the ratio of CCW/CW is less clear. At the wall the flow is constrained to be rectilinear, and so the ratio must be 1 regardless of frequency. However I lack an intuitive picture of how this will depend on the angle of incidence of the incoming wave.

Let us consider reflection from a wall at $x = 0$. I'll specify the incident wave to have velocity components

$$u = A_i \Re(\exp^{i(-kx+ly-\omega t)}), \tag{90}$$

$$v = A_i \Re(\frac{i\omega l - fk}{-i\omega k - fl} \exp^{i(-kx+ly-\omega t)}). \tag{91}$$

Which implies that the reflected wave has components

$$u = -A_i \Re(\exp^{i(kx+ly-\omega t)}), \tag{92}$$

$$v = -A_i \Re(\frac{i\omega l + fk}{i\omega k - fl} \exp^{i(kx+ly-\omega t)}). \tag{93}$$

Now adding the incident and reflected waves and collecting terms yields

$$u = -2A_i \sin(kx) \sin(\omega t - ly), \tag{94}$$

$$v = -2A_i (\frac{(\omega^2 - f^2)kl}{\omega^2 k^2 + f^2 l^2} \cos(kx) + \frac{\omega f(k^2 + l^2)}{\omega^2 k^2 + f^2 l^2} \sin(kx)) \cos(\omega t - ly) \tag{95}$$

Without loss of generality, I can set $y = 0$ and eliminate the ly phase shift in the

trigonometric terms. I can then write

$$u+iv = iA_i[(1-G)\sin(kx)-F\cos(kx)]\exp^{i\omega t} - iA_i[(1+G)\sin(kx)+F\cos(kx)]\exp^{-i\omega t}, \tag{96}$$

where F and G are the fractions in front of the cosine term and sine terms, respectively, in (95). At the wall, $x = 0$, I note that the counterclockwise ($\exp^{i\omega t}$) term and the clockwise ($\exp^{-i\omega t}$) term are equal as expected. One can also note that the cases $k = 0$ and $l = 0$ reduce to expected infinite ocean form. I would like to integrate over a spectrum of waves to investigate whether the ratio relaxes to the infinite ocean case, as I expect. However the integral is not forthcoming algebraicly. Nonetheless, I have performed a number of numerical integrations which indicate that the consistency relation returns to the expected value away from the boundary.

References

[1] Allen, J.S., and P.A. Newberger 1998: On symmetric instabilities in oceanic bottom boundary layers. *J. Phys. Oceanogr.*, 28, 1131-1151.

[2] Batchelor, G.K. 1967: *An Introduction to Fluid Dynamics.* 615 pp., Cambridge Univ. Press, New York.

[3] Chester, D., P. Malanotte-Rizzoli, J. Lynch and C. Wunsch 1994: The eddy radiation field of the Gulf Stream as measured by ocean acoustic tomography. *Geophys. Res. Letts.*, 21, 181-184.

[4] Clift, R., J.R. Grace, and M.E. Weber 1978: *Bubbles, Drops and Particles.* 380 pp., Academic, San Diego, Calif.

[5] Craik, A.D.D. 1970: A wave-interaction model for the generations of windrows. *J. Fluid Mech.*, 41, 801-821.

[6] Craik, A.D.D. 1977: The generation of Langmuir circulations by an instability mechanism. *J. Fluid Mech.*, 81, 209-233.

[7] Craik, A.D.D. and S. Leibovich, 1976: A rational model for Langmuir circulations. *J. Fluid Mech.*, 73, 401-426.

[8] Csanady, G.T. 1973: *Turbulent Diffusion in the Environment.* 248 pp., D. Reidel, Norwell, Mass.

[9] Cummins, P.F., D. Masson, and M.G.G. Foreman 2000: Stratification and mean flow effects on diurnal tidal currents off Vancouver Island. *J. Phys. Oceanogr.*, 30, 15-30.

[10] Cummins, P., and L.-Y. Oey 1997: Simulations of barotropic and baroclinic tides off northern British Columbia, *J. Phys. Oceanogr.*, 27, 762-781.

[11] D'Asaro, E.A. and G.T. Dairiki 1997: Turbulent intensity measurements in a wind-driven mixed layer. *J. Phys. Oceanogr.*, 27, 2009-2022.

[12] D'Asaro, E.A. and M.D. Morehead 1991: Internal waves and velocity fine structure in the Arctic Ocean. *J. Geophys. Res.*, 96, 12,12725-12738.

[13] Davies, A.M., and P. Hall 2000: A three-dimensional model of diurnal and semidiurnal tides and tidal mixing in the North Channel of the Irish Sea. *J. Geophys. Res.*, 105, 17079 - 17104.

[14] Dewey, R. 1999: Mooring design & dynamics - a Matlab package for designing and analyzing oceanographic moorings. *Marine Models*, 1, 103-157.

[15] Faller, A.J., and S.J. Auer 1988: The roles of Langmuir circulations in the dispersion of surface tracers. *J. Phys. Oceanogr.*, 18, 1108-1123.

[16] Farmer, D., and M. Li 1995: Patterns of bubble clouds organized by Langmuir circulation. *J. Phys. Oceanogr.*, 25, 1426-1440.

[17] Foreman, M.G.G., R.A. Walters, R.F. Henry, C.P. Keller, and A.G. Dolling 1995: A tidal model for eastern Juan de Fuca Strait and the southern Strait of Georgia. *J. Geophys. Res.*, 100, 721-740.

[18] Garrett, C., P. MacCready and P. Rhines 1993: Boundary mixing and arrested Ekman layers: Rotating stratified flow near a sloping boundary. *Annu. Rev. Fluid Mech.,* 25, 291-323.

[19] Geyer, W.R., J.H. Trowbridge, M.M. Bowen 2000: The dynamics of a partially mixed estuary. *J. Phys. Oceanogr.*, 30, 2035-2048.

[20] Gill, A.E. 1982: *Atmosphere-Ocean Dynamics.* 662 pp., Academic Press, San Diego, Calif.

[21] Griffin, D.A. and P.H. LeBlond 1990: Estuary/Ocean exchange controlled by spring-neap tidal mixing. *Estuarine, Coastal and Shelf Sci.*, 30, 275-297.

[22] Hamilton, J.M., J. Kim, and F. Waleffe 1995: Regeneration mechanisms of near-wall turbulence structures. *J. Fluid Mech.* 287, 317-348.

[23] Hinze, J.O. 1975: *Turbulence.* 790 pp., McGraw-Hill, New York.

[24] Huang, N.E. 1979: On the surface drift currents in the ocean. *J. Fluid Mech.*, 91, 191-208.

[25] Kenyon, K.E. 1969: Stokes drift from random gravity waves. *J. Geophys. Res.*, 74, 6991-6994.

[26] Kundu, P.K. 1990: *Fluid Mechanics*. 638 pp., Academic Press, San Diego, Calif.

[27] Kunze, E. 2001: Vortical Modes, *Encyclopedia of Ocean Sciences*, Academic Press, San Diego, Calif.

[28] Kunze, E. and T.B. Sanford 1993: Submesoscale dynamics near a seamount. Part I: Measurements of Ertel vorticity. *J. Phys. Oceanogr.*, 23, 2567-2588.

[29] Kunze, E. 1993: Submesoscale dynamics near a seamount. Part II: The partition of energy between internal waves and geostrophy. *J. Phys. Oceanogr.*, 23, 2589-2601.

[30] Langmuir, I. 1938: Surface motion of water induced by the wind, *Science*, 87, 119-123.

[31] Leibovich, S. 1977a: On the evolution of the system of wind drift currents and Langmuir circulations in the ocean, 1, Theory and averaged current. *J. Fluid Mech.*, 79, 715-743.

[32] Leibovich, S. 1977b: Convective instability of stably stratified water in the ocean. *J. Fluid Mech.*, 82, 561-585.

[33] Leibovich, S. 1980: On wave-current interaction theories of Langmuir circulations. *J. Fluid Mech.*, 99, 715-724.

[34] Leibovich, S. 1983: The form and dynamics of Langmuir circulations. *Annu. Rev. Fluid. Mech.*, 15, 391-427.

[35] Leibovich, S. and A. Tandon, 1993: Three dimensional Langmuir circulation instability in a stratified layer. *J. Geophys. Res.*, 98, 16501-16507.

[36] Leibovich, S. and D. Ulrich, 1972: A note on the growth of small scale Langmuir circulations. *J. Geophys. Res.*, 77, 1683-1688.

[37] Leibovich,S. and G. Yang, Turbulent flow in natural water bodies friven by wind and surface waves. *unpublished manuscript.*

[38] Li, M. and C. Garrett 1993: Cell merging and the jet/downwelling ratio in Langmuir circulation. *J. Mar. Res.*, 51, 737-769.

[39] Li, M. and C. Garrett 1995: Is Langmuir circulation driven by surface waves or surface cooling? *J. Phys. Oceanogr.,* 25, 64-76.

[40] Li, M. and C. Garrett 1997: Mixed-layer deepening due to Langmuir circulation. *J. Phys. Oceanogr.*, 27, 121-132.

[41] Li, M., K. Zahariev, and C. Garrett 1995: Role of Langmuir circulation in the deepening of the ocean surface mixed layer. *Science*, 270, 1955-1957.

[42] Lien, R.-C. and P. Müller 1992a: Consistency Relations for gravity and vortical modes in the ocean. *Deep-Sea Res.*, 39, 1595-1612.

[43] Lien, R.-C. and P. Müller 1992b: Normal-mode decomposition of small-scale oceanic motions. *J. Phys. Oceanogr.*, 22, 1583-1595.

[44] McWilliams, J.C., P.P. Sullivan and C.-H. Moeng 1997: Langmuir turbulence in the ocean. *J. Fluid Mech.*, 334, 1-30.

[45] Müller, P. 1995: Ertel's potential vorticity theorem in physical oceanography. *Revs. Geophs.*, 33, 67-97.

[46] Müller, P., R.-C. Lien and R. Williams 1988: Estimates of potential vorticity at small scales in the ocean. *J. Phys. Oceanogr.*, 18, 401-416.

[47] Ott, M.W. 2000: Mixing and Secondary Circulation in Juan de Fuca Strait. *thesis,* University of Victoria.

[48] Provost, C. and P.-Y. Le Traon 1993: Spatial and Temporal Scales in Altimetric Variability in the Brazil-Malvinas Current Confluence Region: Dominance of the Semiannual Period and Large Spatial Scales, *J. Geophys. Res.*, 98, 18037–18051.

[49] Skyllingstad, E.D., and D.W. Denbo 1995: An ocean large-eddy simulation of Langmuir circulations and convection in the surface mixed layer, *J. Geophys. Res.*, 100, 8501-8522.

[50] Soulsby, R. 1983: The bottom boundary layer of shelf seas, in *Physical Oceanography of Coastal and Shelf Seas,* vol. 35 of *Elsevier Oceanography Series*, ed. B. Johns, 189-266, Elsevier, Amsterdam.

[51] Stansfield, K., C. Garrett and R. Dewey 2001: The probability distribution of the Thorpe displacement within overturns in Juan de Fuca Strait. *J. Phys. Oceanogr.*, accepted.

[52] Stanton, T. P. and Thornton, E. B., 1997: Reynolds Stress and Small-Scale Morphology Measurements during DUCK94, *Proceedings of the 25th International Conference on Coastal Engineering*, Orlando, FL, ASCE.

[53] Tandon, A. and S. Leibovich 1995: Simulations of three-dimensional Langmuir circulation on water of constant density. *J. Geophys. Res.*, 100, 22,613-22,623.

[54] Taylor , G.I. 1921: Diffusion by continuous movements. *Proc. London Math. Soc.*, A20, 196-212.

[55] Thomson, R.E., and S.E. Allen 2000: Time series acoustic observations of macrozooplankton diel migration and associated pelagic fish abundence. *Can. J. Fish Aquat. Sci.*, 9, 1919-1931.

[56] Thorpe, S.A. 1995a: On the meandering and dispersion of a plume of floating particles caused by Langmuir circulation and a mean current. *J. Phys. Oceanogr.*, 25, 685-690.

[57] Thorpe, S.A. 1995b: Vertical dispersion of oil droplets in strong winds: The Braer oil spill. *Mar Pollut. Bull.*, 30, 756-758.

[58] Thorpe, S.A., M.S. Cur/'e, A. Graham, and A.J. Hall 1994: Sonar observations of Langmuir circulation and estimation of dispersion of floating particles. *J. Atmos. Oceanic Technol.*, 11, 1273-1294.

[59] Townsend, A.A. 1980: *The Structure of Turbulent Shear Flow.* 429 pp., Cambridge Univ. Press, New York.

[60] von Storch, H. and F. Zwiers 1998: *Statistical Analysis in Climate Research*, Cambridge Univ. Press, New York.

[61] Weller, R.A. and J.F. Price 1988: Langmuir circulation within the oceanic mixed layer. *Deep-Sea Res., Part A*, 35, 711-747.

[62] Zedel, L. and D. Farmer 1991: Organized structures in subsurface bubble clouds: Langmuir circulations in the open ocean. *J. Geophys. Res.*, 96, 8889-8900.